Technical University of Denmark

DTU

Flow modelling of steel fibre reinforced self-compacting concrete

Svec, Oldrich; Olesen, John Forbes; Stang, Henrik; Poulsen, Peter Noe; Thrane, Lars Nyholm

DTU Library
Technical Information Center of Denmark

Flow modelling of steel fibre reinforced self-compacting concrete

Simulating fibre orientation and mechanical properties

Oldrich Svec

PhD Thesis

Department of Civil Engineering
2013

DTU Civil Engineering
Department of Civil Engineering

Department of Civil Engineering - Technical University of Denmark

Flow modelling of steel fibre reinforced self-compacting concrete

- Simulating fibre orientation and mechanical properties

Oldřich Švec

Ph.D. Thesis

Supervisors:

Henrik Stang, Danish Technical University, Denmark
John Forbes Olesen, Danish Technical University, Denmark
Peter Noe Poulsen, Danish Technical University, Denmark
Lars Nyholm Thrane, Danish Technological Institute, Denmark

Assesment Committee:

Hans Holger Hundborg Koss, Danish Technical University, Denmark
Gilles Chanvillard, Lafarge, France
Bhushan Lal Karihaloo, Cardiff University, Great Britain

Preface

This thesis is submitted as a partial fulfilment of the requirements for the Danish Ph.D. degree.

Lyngby, the 24$^{\text{th}}$ May 2013

Oldřich Švec

Acknowledgements

I would like to express my sincere gratitude to my supervisors Henrik Stang (BYG DTU), John Forbes Olesen (BYG DTU), Peter Noe Poulsen (BYG DTU) and Lars Nyholm Thrane (DTI) for giving me the great opportunity to work on this challenging project. Their invaluable guidance, patience and encouragement will always be appreciated.

Furthermore, I would like to thank Jan Skocek for the great collaboration experience during the development of the numerical framework. We have had numerous good discussions ranging from the implementation details of the framework to the phenomenological understanding of the concrete behaviour. Without Jan's big contribution, the numerical framework would have never been developed.

I gratefully acknowledge support from Danish Technological Institute and Norwegian University of Science and Technology. Especially, my sincere gratitude goes to Lars Nyholm Thrane, Terje Kanstad, Giedrius Zirgulis and Elena Vidal Sarmiento who greatly contributed to the experimental part of the research.

Finally, I would like express my thanks to my wife, Jana. Thanks for your love, encouragement and understandings. You are always my biggest motivation to overcome any obstacles that I encountered.

Abstract

Concrete is one of the most widely used materials in the world. Ordinary concrete composition makes the material strong in compression yet weak and brittle in tension. Steel reinforced concrete successfully eliminates the weak tensile properties of the ordinary concrete. Steel fibres dispersed in concrete can efficiently substitute or supplement conventional steel reinforcement, such as reinforcement bars. Ordinary concrete composition further makes the material stiff and non-flowable. Self-compacting concrete is an alternative material of low yield stress and plastic viscosity that does flow and fills the formwork with a little or no effort. Steel fibre reinforced self-compacting concrete is a logical combination of the two types of concrete. The combination nevertheless creates several challenges. It has been observed by many authors that steel fibres orient and distribute according to the flow of the fibre reinforced self-compacting concrete. The orientation and distribution of the fibres results in non-homogeneous and non-isotropic mechanical properties of the structural elements.

The primary aim of this research project was to develop a numerical framework capable of predicting the fibre orientation and distribution in structural elements made of fibre reinforced self-compacting concrete. The existence of a such numerical tool is essential for the wider usage of the material. The developed numerical framework is capable of simulating free-surface flow of a suspension of explicitly represented rigid particles immersed in the non-Newtonian fluid. The non-Newtonian fluid was modelled by the novel Lattice Boltzmann fluid dynamics solver. The numerical framework, among others, allows for a two-way coupling between the fluid and the explicitly represented immersed particles. The coupling was done by means of the Immersed boundary method with direct forcing. Evolution of the immersed particles was described by Newton's differential equations of motion. The Newton's equations were solved by means of Runge-Kutta-Fehlberg iterative scheme.

Several challenges had to be overcome during the development of the numerical framework to be able to successfully simulate the flow of the fibre

reinforced self-compacting concrete. Fibres are particles of high aspect ratio. To allow for efficient simulation of a large number of the immersed fibres, the fluid domain must be discretized into a coarse grid. The discrete fibre diameter then usually reduces to a sub-grid size, which significantly decreases accuracy of drag forces acting on the fibres. A function was therefore proposed to correct the drag forces. Formwork used in the structural industry is often smooth and slippery which results in an apparent slip of the fluid near formwork surface. A method to incorporate the apparent slip into the Lattice Boltzmann fluid dynamics solver was suggested.

The proposed numerical framework was observed to correctly predict flow of fibre reinforced self-compacting concrete. The proposed numerical framework can therefore serve as an efficient alternative to conventional experimental and analytical tools. Simulations performed by the numerical framework together with the experimental observations revealed several important conclusions: 1) Fibres orient under the flow of fibre reinforced self-compacting concrete. 2) Formwork surface can play an important role in the fibre orientation. 3) Fibre orientation significantly influences mechanical behaviour of the material. 4) A prevailing linear relation between the fibre orientation and tensile mechanical behaviour of the material seems to exist.

The ability to simulate the casting process of fibre reinforced self-compacting concrete, including the movement of individual immersed fibres in response to such factors as formwork geometry and surface roughness, has profound implications toward the effective use of these materials within the civil infrastructure. Together with physical experimentation, this coupled simulation of concrete casting and its load resistance in the hardened state presents opportunities for improving material performance for both ordinary and high-performance applications.

Resumé

Beton er det mest anvendte byggemateriale i verden. Almindelige betonsammensætninger gør materialet stærkt i tryk, men sprødt og svagt i træk. Traditionel stålarmering eliminerer effektivt de svage trækegenskaber i almindelig beton. Stålfiberarmering fordelt i selve betonmaterialet – og som udstøbes sammen med betonen – kan på en effektiv måde erstatte en del eller al den konventionelle stålarmering. Traditionelle betonmaterialer er normalt – inden de hærder – relativt tyktflydende og kræver vibration under udstøbning. I de senere år er udviklet specielle betonmaterialer, som er letflydende – med lav viskositet og flydespænding – og som kan fylde formen uden nogen form for vibration eller bearbejdning under udstøbning. Disse materialer kaldes selvkompakterende beton. Fiberarmeret selvkompakterende beton er en logisk sammensætning af de omtalte to typer specialbeton. Selvom selvkompakterende, fiberarmeret beton rummer mange fordele, er der også mange udfordringer forbundet med anvendelsen af materialet. Det er rapporteret i litteraturen hvordan fiber orienteres og fordeles af strømningsmønsteret, når formen fyldes. Denne orientering kan resultere i inhomogene og anisotrope egenskaber ved den hærdede beton.

Det primære formål med dette forskningsprojekt har været at udvikle et numerisk værktøj, som er i stand til at forudsige fiberorientering og fordeling i konstruktionselementer udført af stålfiberarmeret, selvkompakterende beton. Sådanne værktøjer er essentielle for udbredelsen af brugen af dette lovende materiale. Det udviklede værktøj er i stand til at simulere fri-overflade strømning af en suspension af eksplicit modellerede partikler i en ikke-Newtonsk væske. Væsken er modelleret vha. den såkaldte Lattice-Boltzmann metode. Det numeriske værktøj benytter to-sidet kobling mellem væsken og partiklerne. Koblingen er modelleret med den såkaldte 'Immersed Boundary Method' mens partiklerne bevægelse er modelleret med Newtons klassiske bevægelsesligninger. Det ikke-lineære ligningssystem løses ved hjælp af den såkaldte Runge-Kutta-Fehlberg iterative metode.

Udviklingen af værktøjet har budt på en række udfordringer. Fibrene er partikler med et stort forhold mellem længde og diameter. På den anden

side er det nødvendigt at benytte en relativt grov numerisk diskretisering af strømningsområdet, for at opnå en effektiv simulering. Fiberdiameteren bliver således væsentligt mindre end det numeriske net, hvilket gør det vanskeligt at bestemme samvirkningen mellem væske og fibre. Dette problem er løst i det udviklede værktøj, ligesom værktøjet muliggør modellering af forskellige overflader i formen. Det er bl.a. muligt at modellere glatte og olierede overflader, som ofte forekommer i virkelige betonforme. Ved sammenligninger med eksperimenter er det eftervist, at det udviklede værktøj korrekt forudsiger strømningen af fiberarmeret, selvkompakterende beton. Værktøjet kan derfor benyttes som et alternativ til traditionelle eksperimentelle og analytiske metoder. Simuleringer og sammenligninger med eksperimenter afslørede et antal vigtige forhold: 1) Der finder en stærk orientering af fibrene sted under strømning af fiberarmeret, selvkompakterende beton. 2) Beskaffenheden af formens overflade har stor betydning for fiberorienteringen. 3) Fiberorienteringen har stor betydning for de mekaniske egenskaber af materialet. 4) Sammenhængen mellem fiberorientering og mekaniske egenskaber er relativt simpel og overvejende lineær.

Muligheden for at udføre simuleringer af støbeprocessen af fiberarmeret, selvkompakterende beton, som inkluderer bevægelsen af de enkelte fibre og indflydelsen fra formgeometri og –overflader, har stor betydning for en effektiv udnyttelse af dette lovende materiale til bygningskonstruktioner. Simuleringen, eksperimentelle undersøgelser og kobling til forudsigelse af de mekaniske egenskaber i hærdet tilstand udgør unikke muligheder for at videreudvikle og optimere materialeegenskaber i både almindelige og mere avancerede anvendelser.

Contents

Chapter 1

Introduction

More than 10 billion tons of concrete are produced every year[1]. This makes concrete one of the most widely used materials in the world. Concrete is primarily composed of cement, water, fine and coarse aggregates, additives and admixtures. An ordinary concrete has excellent properties as a structural material when loaded in compression. An ordinary concrete is on the other hand very weak and brittle when loaded in tension (Neville, 1995).

Tensile stresses are commonly taken by a conventional steel reinforcement, such as steel reinforcement bars or steel reinforcement grids. The use of conventional steel reinforcement has nevertheless several important drawbacks. The reinforcement is usually assembled and placed into the formwork manually which increases the construction time and costs (Grunewald, 2004). Individual steel reinforcement bars are further typically positioned with relatively large mutual spacing. Subsequently, the concrete matrix located between the reinforcement bars might be exposed to non-zero tensile stresses. This often leads to micro-cracking of the conventionally reinforced concrete (Rossi et al., 1987).

Steel fibre reinforced concrete might serve as a promising alternative to conventional steel reinforcement (Mobasher et al., 1990). Contrary to the large continuous unidirectional reinforcement bars, the homogeneously dispersed steel fibres reinforce the concrete evenly, thus effectively reducing and controlling any micro-cracks arising in the concrete matrix. Steel fibres are normally added to the concrete before casting which favourably reduces necessary in-situ costs. Compared to the conventional steel reinforcement, steel fibres usually provide a weaker strength and ductility to the concrete. In many industrial applications, the steel fibres can nevertheless effectively and beneficially substitute or complement the conventional reinforcement (Sand-

---

[1]http://concretehelper.com/concrete-facts/

Figure 1.1*: Sydney Opera House: An example of a concrete structure. (wikimedia.org)*

bakk, 2011).

An ordinary concrete is in the fresh state stiff and thus does not flow (Figure 1.2a). The casting process of an ordinary concrete is therefore accompanied by an extensive vibration of the material. The primary aim of the vibration is to level the concrete and to remove any air bubbles entrapped in the concrete. The vibration process of the concrete is a very labour and time intensive process which has negative impacts on the human body and the working environment in general. Self-compacting concrete provides an effective alternative to the stiff ordinary concrete (Figure 1.2b). Self-compacting concrete flows due to its own weight, levels with a little or no vibration and does not entrap air excessively (Okamura and Ouchi, 2003; Thrane, 2007).
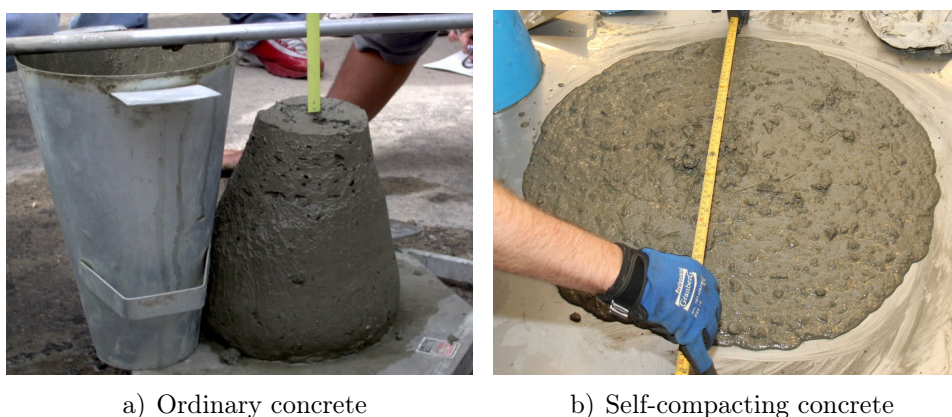
a) Ordinary concrete   b) Self-compacting concrete

Figure 1.2*: Slump test*

Steel fibre reinforced self-compacting concrete is a logical combination

of fibre reinforced concrete with self-compacting concrete. Such a concrete allows for very fast and simple casting of the material, effectively reducing erection costs of the structure. Further, the self-compacting concrete overcomes problems due to vibration, creates safer working environment, allows for innovative architectural features, provides better surface finish, improves durability, allows for thinner concrete structures and provides better reinforcement bonding. The immersed steel fibres improve freeze-thaw resistance, resistance to explosive spalling, impact resistance, resistance to plastic shrinkage during curing and others (Grunewald, 2004).

Fibre reinforced self-compacting concrete has on the other hand several important drawbacks. The concrete is more expensive compared to conventional concrete. It is often challenging to produce the required flow-ability properties of the concrete and to avoid segregation of the immersed aggregates and fibres. Due to the low yield stress of the concrete, formwork must carry relatively high pressure. Finally, steel fibres are not able and probably will never be able to transfer the same tensile loads as the traditional reinforcement.

It has been observed by many authors that steel fibres orient and distribute according to the flow of fibre reinforced self-compacting concrete (Kooiman, 2000; Stähli et al., 2007; Zerbino et al., 2012). Figure 1.3 as an example shows a top view of a beam specimen cut from a slab made of fibre reinforced self-compacting concrete (see Chapter 7 for further details). Fibres in the left part of the beam specimen seem to be predominantly oriented normal to the beam length. On the other hand, the steel fibres tend to be oriented parallel to the beam length in the right part of the beam specimen. The various fibre orientations and distributions typically origin in the casting process and result in non-homogeneous and non-isotropic mechanical response of the structural elements. This significantly complicates the design process and without a deeper understanding of the mechanisms responsible for the fibre orientation limits the use of the material. The study of the fibre orientation and distribution and their link to casting methods and flow patterns is therefore the main objective of the presented research project.

The following sections introduce the state-of-the-art of the understanding of the various aspects of the fibre orientation such as the main phenomena driving the fibre orientation, the impact of the fibre orientation on the mechanical response of the material, the different means to represent the fibre orientation or the various tools available to obtain the fibre orientation.

Figure 1.3: *Top view of a beam specimen cut from a slab made of fibre reinforced self-compacting concrete (see Section 7 for further details). Individual lines were obtained by x-ray computed tomography and represent immersed steel fibres.*

1.1 Origin of fibre orientation

Orientation of steel fibres immersed in the self-compacting concrete origins from a combination of several basic phenomena, of which the most important ones are the so-called wall effect, shear induced orientation and extensional stresses induced orientation (Martinie and Roussel, 2011).

1.1.1 Wall effect

Wall effect is caused by the interaction of the immersed steel fibres with the surrounding rigid obstacles such as formwork (Soroushian and Lee, 1990; Stroeven, 1999; Dupont and Vandewalle, 2005). It is geometrically impossible to have a rigid fibre located normal to the formwork at a distance less than half-length of the fibre (red rectangle in Figure 1.4). Hence, the rigid fibre tends to orient according to the surrounding flow with a restriction imposed by the wall (fibre marked as blue rectangle).
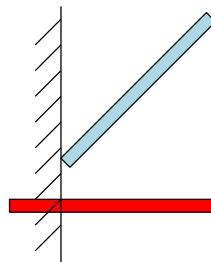
Figure 1.4: *Wall effect: Blue and red bars stand for the possible and impossible orientation of the rigid fibre located in the vicinity of the wall.*

1.1.2   Shear induced orientation

Shear induced orientation of rigid fibres was first described by Jeffery (1922) for the case of a dilute suspension of massless inertia-free ellipsoids immersed in a Newtonian incompressible fluid. Since then, a lot of research has been carried on to study semi-dilute and concentrated suspensions of fibres or to study non-Newtonian fluids, such as concrete (Folgar and Tucker, 1984; Ozyurt et al., 2006; Chung, 2007). In the case of an ideal Newtonian fluid, the rigid fibre performs one of the infinite sets of Jeffery's orbits[2]. When the fibre orients parallel to the shear flow, forces acting on the fibre almost disappear. Practically, any small disturbance of the fibre, such as fibre contact with other obstacles, has a strong influence on the forces and often forbids the fibre from performing the orbits. Under a steady and constant shear rate surrounding an immersed rigid fibre, the rigid fibre then orients nearly parallel to the shear flow direction and remains in that position (Figure 1.5). Shear induced orientation of rigid fibres takes approximately 0.5 up to 5 seconds depending among others on material properties (Martinie and Roussel, 2011). Compared to the duration of the casting process, the shear induced orientation can be assumed to be instantaneous.
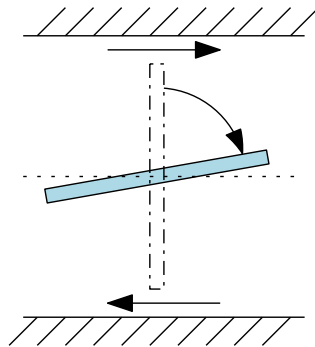
Figure 1.5*: Shear induced orientation: The horizontal arrows represent the shear direction. The dot-dashed bar stands for the initial state of the fibre. The blue bar stands for the final state of the fibre.*

     Shear induced orientation, among others, takes place in the vicinity of a formwork. At the formwork surface, the fluid can be assumed to have a zero velocity relative to the formwork. With an increasing distance of the fluid from the formwork surface, the fluid velocity increases. The spatial velocity

---

[2]Jeffery's orbits describe the irregular rotation of an ellipsoid suspended in a sheared fluid. (`http://demonstrations.wolfram.com/JefferysOrbits/`)

change of the fluid, i.e. the shear rate, is the driving force for the shear induced orientation.

1.1.3 Extensional stresses induced orientation

Extensional stresses induced orientation orients fibres normal to the flow direction (Barnett et al., 2009; Boulekbache et al., 2010; Martinie and Roussel, 2011). Such orientation is among others predominant in the case of thin plate casting. As an example, plate of a constant discharge is cast from a circular inlet (brown filled circle in Figure 1.6) positioned at one of the corners of the plate. Concrete spreads from the inlet in a circular shape (dashed lines). A rigid fibre immersed in the flow is illustrated by a bar of blue fill. Figure 1.6 presents three different time steps of the concrete flow. Time, $t = 1$, $t = 2$ and $t = 3$ are marked by red, orange and blue stroke, respectively. At initial state, $t = 1$, the fibre is almost parallel to the flow direction (red stroke bar). As the fibre moves away from the inlet, the fibre orients normal to the flow direction (blue stroke bar).
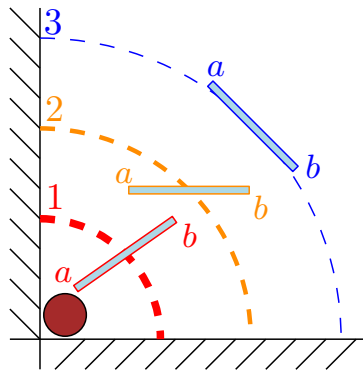
Figure 1.6: *Extensional stresses induced orientation: Top view illustration of plate casting. Brown circle is the inlet. Red, orange and blue colours stand for three different time steps of the immersed fibre (bar of blue fill).*

Red, orange and blue dashed circular curves represent the same material at the three different time steps. As the distance of the circular curves from the inlet increases the length of the curves also increases. With the increasing length and with the constant discharge, the velocity of the concrete parallel to the flow direction decreases (thickness of the dashed circular curves). At time $t = 1$, velocity of point a is therefore larger than velocity of point b. The difference between the two velocities forces the fibre to orient normal to the flow direction. When point a and b reach the same circular curve, the fibre

remains in that orientation state. Experimental evidence of this phenomenon can bee seen e.g. in Chapter 7 and Chapter 5.

1.2 Influence of fibre orientation on mechanical behaviour

One of the main interests dealing with the fibre reinforced self-compacting concrete is to understand the influence of fibre orientation on the tensile mechanical behaviour of the material. This field has been therefore extensively studied by many researchers (Jansson et al., 2008; Bolander et al., 2008; Laranjeira et al., 2010; Sandbakk, 2011). In this section, the focus is laid on two particular problems, namely the effect of number of fibres crossing a fracture plane and the effect of fibre inclination at the fracture plane on the resulting mechanical response of the structure.

A fibre can be assumed to be active in a fracture process when the fibre bridges a fracture plane (Figure 1.7a). For the case of a dilute fibre suspension, the overall tensile behaviour of the material can be approximated as a combination of plain concrete contribution and contribution of the individual fibres.

a) 0°   b) 0°   c) 60°
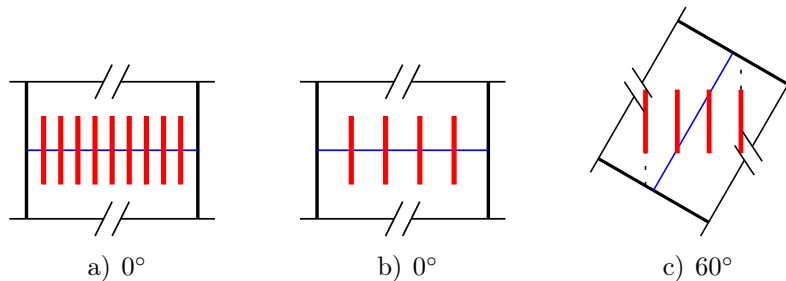
Figure 1.7: *Illustration of the number of fibres crossing a fracture plane for various set-ups. The fibres and the fracture planes are marked by red and blue lines, respectively.*

The number of fibres bridging the fracture plane has the primary effect on the tensile stresses of the material (Oliveira, 2010). As an example, Figure 1.7a indicates more than double the number of fibres crossing the fracture plane compared to Figure 1.7b. We can therefore expect that the fibre reinforced concrete depicted in Figure 1.7a will result in more than double the tensile mechanical response compared to the fibre reinforced concrete depicted in Figure 1.7b. Pull-out response of individual fibres bridging the fracture plane also plays an important role. The fibre pull-out response is,

among others, influenced by the concrete type, fibre type, fibre embedment length, or fibre inclination relative to the fracture plane (Soetens et al., 2013).

The number of fibres present in the fracture plane is primarily influenced by the local fibre volume fraction (Figure 1.7a,b) and by the local fibre orientation (Figure 1.7b,c). Figure 1.7c illustrates a fracture plane rotated by 60°. In such a case, only two fibres out of four cross the fracture plane. If the fracture plane was in this particular example rotated by more than 60°, no fibres would cross the fracture plane at all. The local fibre orientation has therefore a strong impact on the number of fibres bridging the fracture plane. Figure 1.7c further reveals that the local fibre orientation also affects the fibre inclination relative to the fracture plane (Thorenfeldt, 2003).

1.3 Representation of fibre orientation

1.3.1 Orientation factor

Tensile mechanical response of fibre reinforced self-compacting concrete is primarily influenced by the number of fibres in the fracture plane, N_f, and secondarily by other phenomena, such as inclination of fibres in the fracture plane (Section 1.2). It can be therefore advantageous to represent the local fibre orientation in terms of the number of fibres crossing a given plane. The fibre orientation factor, α, satisfies this condition (Krenchel, 1975; Stroeven, 1979; Gettu, 2004; Martinie and Roussel, 2011):

$$\alpha = \frac{N_f A_f}{\Phi A_c} \ ,$$
(1.1)

where Φ, A_c and A_f denote fibre volume fraction, the concrete area and the single fibre area, respectively. The orientation factor can be seen as the area of fibres relative to the maximum theoretical area of the fibres crossing a given plane. When the orientation factor is equal to $\alpha = 0$, no fibres cross the given plane. This also means that all the fibres must be parallel to the given plane. When the orientation factor is equal to $\alpha = 1$, the maximum number of fibres cross the given plane. In such a case, all the fibres must be normal to the given plane. Hence, the average fibre inclination relative to the given plane can be also deduced from the fibre orientation factor (Thorenfeldt, 2003).

1.3.2 Other representations

The most complete information about the fibre orientation and distribution is achieved when position and orientation of every single immersed fibre is

tracked. The main drawback of such a representation is the lack of experimental and analytical tools capable of acquiring and processing that complex information. X-ray computed tomography and subsequent data analysis is currently the only reliable experimental technique that can provide position and orientation of all the individual immersed fibres (Suuronen et al., 2012). Similarly, the emerging numerical simulations of flow are able to provide such complex information (Kulasegaram and Karihaloo, 2013). The numerically or experimentally obtained fibre positions and orientations can subsequently serve as a direct input to the numerical simulations of fracture process of the fibre reinforced self-compacting concrete.

Once obtained either experimentally or numerically, position and orientation of every single immersed fibre can be converted into a probability distribution function or into a symmetrical even order orientation tensor (Advani and Tucker, 1987). The even order orientation tensor simplify the matter by converting the large number of fibre positions and orientations into several degrees of freedom. The most commonly used even order orientation tensor is the symmetrical second order orientation tensor which, as an example, has six independent degrees of freedom in 3D. The second order orientation tensor can be visualized by means of orientation ellipsoids in 3D space or orientation ellipses in 2D plane. Figure 1.8, as an example, presents a top view projection of 3D orientation ellipsoids constructed from Figure 1.3 (see Section 7 for further details).
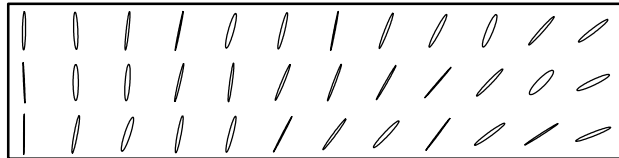
Figure 1.8: *Top view of fibre reinforced self-compacting concrete beam specimen: Illustration of 3D fibre orientation ellipsoids projected into 2D orientation ellipses.*

1.4 Experimental determination of fibre orientation

1.4.1 Manual counting

Manual counting is a simple destructive experimental method which is used to estimate the number of fibres crossing a given plane. The number of

fibres is often used to determine the fibre orientation factor (Section 1.3.1), assuming the fibre volume concentration and the fibre cross sectional area to be known. The method does not require any special equipment or skills but on the other hand, it is relatively time consuming. The method further does not provide enough information to properly distinguish between the effect of fibre orientation and local fibre volume concentration. The two phenomena can be separated by e.g. crushing of the fibre reinforced self-compacting concrete and weighting the steel fibres within. Manual counting is commonly composed of the following steps. A structural element made of fibre reinforced self-compacting concrete is cut along a given plane of interest (Figure 1.9a). The plane is polished and the number of fibres crossing the plane is counted (Figure 1.9b,c).

a)   b)   c)
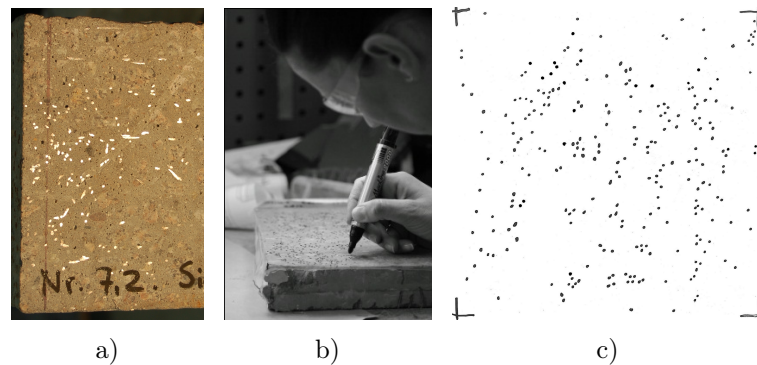
Figure 1.9: *Process of manual counting. a) cut specimen. b) Manual counting. c) Scanned result. (Žirgulis et al., 2013a)*

1.4.2   Identification of fibre inclination

Recognition of fibre inclination is a based on manual counting with the addition of fibre cross-sectional shape analysis. Similarly to manual counting, the procedure begins with cutting and polishing a given plane of interest. The plane polishing is performed to remove any fibre deformations caused by the cutting. The number and shape of the fibres crossing the given plane is then analysed. X-ray tomography, photography, image analysis and other techniques help to automate the analysis process (Lee et al., 2002; Blanc et al., 2006; Wuest and Denarié, 2009; Liu et al., 2011, 2012).

    Figure 1.10 as an example illustrates two fibres crossing a given plane. When the fibre is normal to the given plane, the cross-section of the fibre visible at the given plane has a circular shape (left). When the fibre crosses the given plane at a different inclination, the cross-sectional shape of the
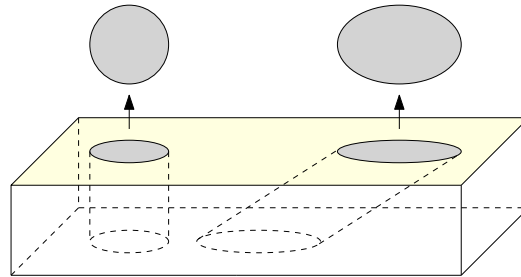
Figure 1.10*: Illustration of two fibres (dashed cylinders) crossing a give plane (yellow). Grey ellipses denote fibre cross-sectional shapes at the given plane.*

fibre becomes an ellipse (right). The inclination of the fibre relative to the given plane can be estimated based on lengths of major and minor axes of the ellipse. A single ellipse can represent two different fibre inclinations. It is therefore necessary to cut and analyse three mutually perpendicular planes to obtain a complete information about the fibre orientation in the given region.

1.4.3   X-Ray computed tomography

X-Ray computed tomography with subsequent image analysis is an advanced technique used to obtain a 3D model of the internal structure of an element. X-Ray computed tomography produces tomographic slices, i.e. images, of specific areas of the element. A set of successive tomographic slices form a 3D image which can be subsequently converted into the 3D model.

In the field of fibre reinforced concrete, the method has been used by e.g. Le et al. (2008); Barnett et al. (2009); Suuronen et al. (2012); Bytyci (2012); Žirgulis et al. (2013b). As an example, Suuronen et al. (2012) used an industrial μCT scanner (Figure 1.11a) to obtain a 3D image and subsequently a statistical representation of steel fibres contained in cylinders drilled from a fibre reinforced concrete slab. Bytyci (2012) used HiSpeed CT/i scanner produced by Ge Medical Systems to scan 12 standard size beams. Žirgulis et al. (2013b) used a medical CT scanner Siemens Somatom Sensation 4 (Figure 1.11b) to scan 18 standard size beams specimens cut from a slab and made of fibre reinforced self-compacting concrete.

X-ray computed tomography is probably the only experimental method capable of obtaining position and orientation of every single fibre located in the steel fibre reinforced self-compacting concrete. The method is also highly efficient. As an example, a standard size beam can be scanned in less than

a)   b)
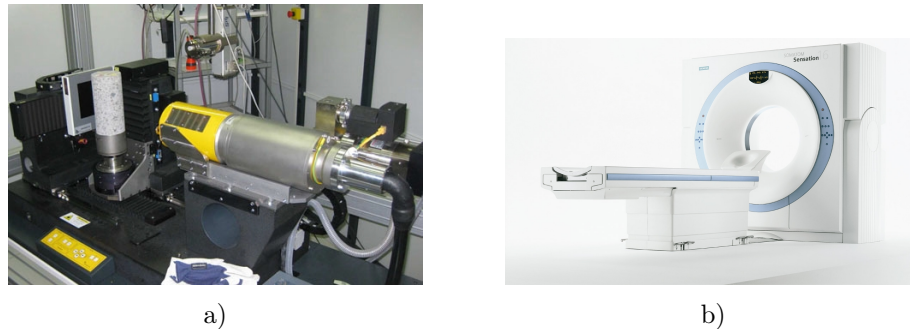
Figure 1.11: *a) Industrial µCT scanner (Suuronen et al., 2012). b) Medical CT scanner.*

a minute when using the medical CT scanner Siemens Somatom Sensation 4 (Žirgulis et al., 2013b). A complete information of the fibre orientation and distribution in a large slab can be obtained in one day. X-ray computed tomography has on the other hand several drawbacks: The scanned fibres must have a significantly different attenuation coefficient[3] compared to the surrounding, such as concrete matrix; Steel reinforcement bars have a large attenuation coefficient which can easily make the scanner "blind"; Finally, a CT scanner of high tube voltage is desirable to obtain a clear distinction between the concrete matrix and the steel fibres within.

1.4.4 Transparent gel

Transparent gel, such as Carbopol, is sometimes used in place of the self-compacting concrete. Steel fibres immersed in the transparent gel are then visible during the whole casting of an element (Figure 1.12). Image analysis is subsequently used to detect the immersed fibres. Carbopol is a shear thinning material which can be for low shear rates assumed to act as Bingham plastic fluid. Carbopol was as an example used by Vasilic et al. (2011); Spangenberg et al. (2012b) to study migration of aggregates in the self-compacting concrete. Boulekbache et al. (2010); Hvilsom and Rasmussen (2011) used Carbopol to study fibre orientation and distribution in the fibre reinforced self-compacting concrete.

    The ability to see the evolution of the fibre orientation and distribution during the whole casting process is probably the main benefit of this method. Carbopol on the other hand brings several challenges. Carbopol is a relatively acid fluid. Stainless steel fibres must be therefore used in place of ordinary

---

[3]Attenuation is a gradual loss in intensity of any kind of flux (such as x-rays) through a medium.

a) Initial state   b) Final state
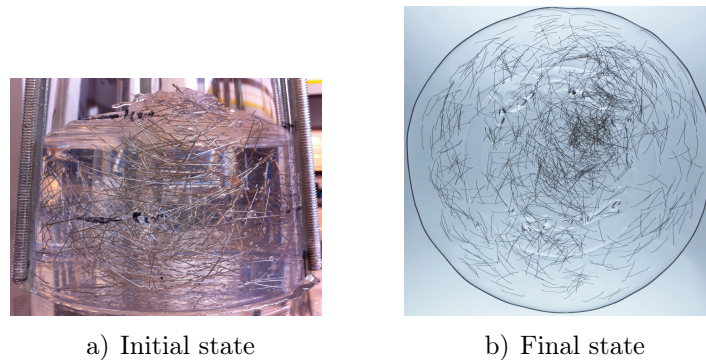
Figure 1.12: *An example of transparent Carbopol gel with immersed stainless steel fibres.*

steel fibres. Carbopol, similarly to self-compacting concrete, has an apparent yield stress. The non-zero yield stress entraps any emerging air bubbles in the gel. The entrapped air bubbles then make the image analysis and fibre recognition harder.

1.4.5 Mechanical testing

Mechanical testing of fibre reinforced self-compacting concrete elements can serve as an indirect indication of the local fibre orientation within the element (Zerbino et al., 2012). Three- and four-point bending tests of standard size beams are among the most commonly used mechanical test set-ups. Standard size beams are usually cast as beams. It might be on the other hand advantageous to cast larger structural elements, such as a slabs. The slabs can then be saw cut into the standard sized beams. The advantage of such an approach is the larger expected variation in the mechanical response of the beam specimens (Figure 1.13, Zerbino et al. (2012)) and consequently in the fibre orientation.

Figure 1.14 shows an example of flexural stresses (at $cmod = 0.5\,\text{mm}$ and $cmod = 2.5\,\text{mm}$) as a function of the number of fibres crossing the fracture plane. The figure indicates a prevailing linear relation. Having the knowledge of the linear relation, the number of fibres and consequently the local fibre orientation factor can be then estimated by mechanical testing of the structural elements.

1.4.6 Other techniques

Faifer and Ottoboni (2011) provides a brief overview of other various meth-
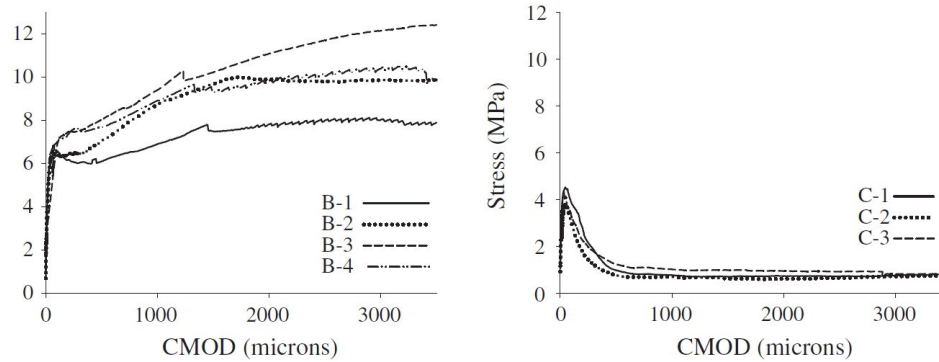
Figure 1.13*: Result of three-point bending test for standard size beams saw cut from different locations of a slab. (Zerbino et al., 2012)*
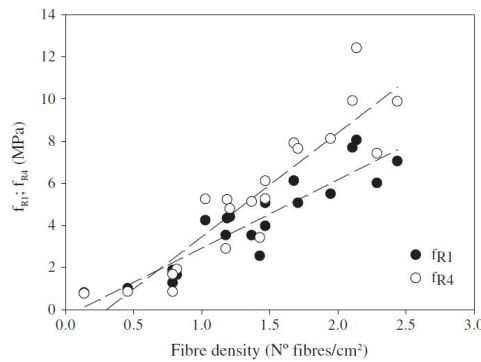
Figure 1.14*: Relation linking flexural stresses to the number of fibres crossing the fracture plane. (Zerbino et al., 2012)*

ods available in the field of destructive and non-destructive fibre orientation and distribution measurements. The most widely discussed method is AC impedance spectroscopy (Woo et al., 2003; Ozyurt et al., 2006; Chung, 2007; Wansom and Janjaturaphan, 2013). Low-frequency resistance measurements (Lataste et al., 2008), coaxial probe and microwave reflectometry (Damme, 2004) or impedance-over-frequency measurements (Faifer and Ottoboni, 2009) are yet another techniques. All the aforementioned alternative methods aim to provide a simple and cheap way to measure fibre orientation and/or distribution. Majority of the methods is nevertheless in their early research phase.

1.5 Numerical estimation of fibre orientation

Numerical frameworks capable of predicting orientation and distribution of fibres immersed in the self-compacting concrete can serve as an efficient alternative to the aforementioned experimental methods. Such numerical frameworks usually consists of a fluid dynamics solver and fibre orientation and distribution solver.

1.5.1 Fluid dynamics solvers

Various fluid dynamics solvers exist and can be differentiated by the time and spatial scale they operate on. The shortest time scales and smallest space scales are modelled by e.g. molecular dynamics simulations. Such numerical simulations solve movement and interactions of individual atoms in the given fluid. These simulations therefore provide the highest available resolution of the given problem. The high resolution on the other hand significantly restricts application of such methods to microscopic or atomic scale problems. This limitation is considerably reduced by lattice gas automata, dissipative particle dynamics or lattice Boltzmann method. All the three methods still solve movement of atoms in the fluid but they pose many assumptions and simplifications to reduce the amount of information simulated. The substantial reduction then allows for macroscopic numerical simulations. Lattice gas automata restricts movement and interaction of individual atoms onto a 2D or 3D lattice. The restriction creates so called lattice artefacts. Dissipative particle dynamics is an off-lattice mesoscopic method that does not restrict the movement of atoms onto the lattice and thus does not create the lattice artefacts. Instead, the method replaces individual atoms by clouds of atoms. Lattice Boltzmann method can be seen as a combination of the lattice gas cellular automata and dissipative particle dynamics. Lattice Boltzmann method replaces individual atoms by clouds of atoms, i.e. by statistical particle distribution functions. The method further restricts the movement of the clouds onto a 2D or 3D lattice.

Macroscopic fluid dynamics solvers can be split into two main categories. Concrete can be either seen as a continuous non-Newtonian fluid or as a granular discontinuous material (Figure 1.15). The continuous fluid is commonly represented by macroscopic Navier's Stokes differential equations that define the time evolution of mass, momentum or energy. A large range of numerical frameworks solve the Navier's Stokes equations (Dufour and Pijaudier-Cabot, 2005; Kulasegaram et al., 2011; Spangenberg et al., 2012a; Kulasegaram and Karihaloo, 2013). The individual methods are differentiated by the way they solve the differential equations. Finite element method, finite volume method

or finite difference method are the most commonly used and accepted methods in the field of fluid dynamics. Smooth particle hydrodynamics is an alternative novel mesh-free solver of the Navier's stokes equations. Discrete element method is the most widely accepted numerical simulation of granular discontinuous material. The discrete element method is based on molecular dynamics. Instead of simulating movement and interactions on the level of atoms, the method tracks movement and interactions of macroscopic granular particles, such as aggregates, sand, etc.
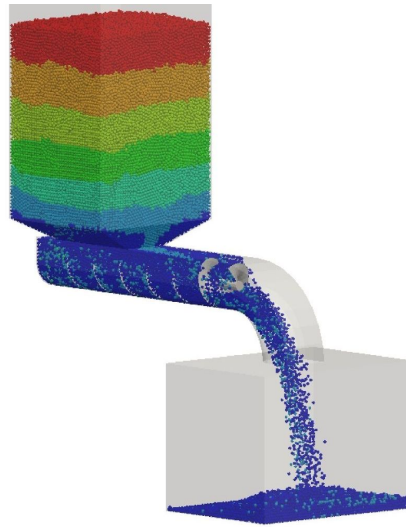
Figure 1.15: *An example of discrete element method (B. Avci, P. Wriggers, www.ikm.uni-hannover.de)*

1.5.2 Fibre orientation solver

Similarly to fluid dynamics solvers, the fibre orientation solvers can be differentiated by the resolution of the method. Statistical representation of the fibre orientation (distribution functions or even order orientation tensors) provide one of the least resolutions but allow for simulations of basically unlimited number of fibres (Dupret and Verleye, 1999; Laure and Silva, 2007; Dumont et al., 2009; Phelps and Tucker, 2009; Montgomery-Smith et al., 2010). Phenomena such as collisions among fibres, collisions of fibres with formwork or fibre influence on the effective viscosity and yield stress of the fluid are hard to express and often result in the introduction of fitting constants. Simulation of individual fibres immersed in the fluid eliminates most of the drawbacks at the cost of a significant computational demand increase.

In the framework of the lattice Boltzmann method, the immersed fibres can be simulated by simple bounce-back scheme (Jianzhong et al., 2003; Qi, 2006). In such a case, fibres and the fluid dynamics solver share the same discrete spatial domain. As a consequence, the fluid domain must be finely discretized to accommodate the fibres. This results in an large increase in computational costs. The simple bounce-back scheme is therefore applicable only to numerical simulations of several fibres. To allow for a large number of fibres, the discrete fluid domain must be separated from the discrete spatial domain of fibres. Immersed boundary method provides such a separation (Wu and Aidun, 2009, 2010).

1.6 Objective and scope of the research

The presented research project was part of a larger project: Innovation consortium "Sustainable Concrete Structures using Steel Fibre Reinforced Concrete" funded by the Danish Strategic Research Council, Grant no. 09-069955. The primary aim of the presented research Ph.D. project was to develop a novel methodology linking the casting process of steel fibre reinforced self-compacting concrete to the resulting fibre orientation and consequently to the mechanical response of the hardened material. Knowledge and control of the fibre orientation and distribution can significantly increase efficiency and competitiveness of the material. The fibre orientation and distribution is nowadays primarily obtained by means of experimental investigations, such as x-ray computed tomography. These experiments are often time consuming and expensive. Numerical simulations of the flow can therefore serve as a cheap and relatively quick alternative. A numerical framework capable of predicting fibre orientation and distribution in structural elements made of fibre reinforced self-compacting concrete was therefore developed.

1.7 Research strategy

Based on the aforementioned requirements, a numerical framework capable of simulating flow of a suspension of explicitly represented rigid particles immersed in the free-surface flow of the non-Newtonian fluid was developed. The Lattice Boltzmann method was chosen as the fluid dynamics solver due to its simple implementation and due to its ability to easily include various required phenomena, such as the free surface or the non-Newtonian rheology.

The developed framework includes two-way coupling between the fluid and the rigid immersed particles. The immersed boundary method was found

to be an appropriate method for the given task due to its ability to efficiently simulate explicitly represented sub-grid sized immersed particles. The immersed particles are, among others, allowed to collide with other immersed particles, formwork or reinforcement bars.

Various iterative techniques of solving the Newton's equations of motion, responsible for the correct particle dynamics, were analysed. Iterative Runge-Kutta-Fehlberg method with adaptive time step was chosen to numerically solve the equations of motion. The iterative method was chosen due to its accuracy and efficiency even for stiff differential equations. Several phenomena such as lubrication forces, particle collisions, elasticity of collisions or friction during collisions were also studied and implemented into the numerical framework.

Several difficulties in the development of the numerical framework had to be overcome to successfully simulate flow of the fibre reinforced self-compacting concrete. Fibres are particles of high aspect ratio, i.e. of high fibre length to fibre diameter ratio. The very low relative fibre diameter together with the requirement to simulate large number of fibres inevitably results in a sub-grid discrete fibre diameter. The sub-grid diameter leads to inaccuracies in the drag forces acting on the fibres. These inaccuracies were resolved by introducing a correction function. Formwork used in the structural industry is often smooth and slippery which results in an apparent slip of the fluid near formwork surface. We have therefore developed a method to include the Navier's slip into the Lattice Boltzmann fluid dynamics solver. Finally, we have studied whether the effect of immersed aggregates can be successfully modelled by the yield stress of the Bingham plastic fluid.

A range of field and laboratory experimental studies was conducted to verify the proposed numerical framework. Transparent gel Carbopol was used together with stainless steel fibres to mimic the flow of fibre reinforced self-compacting concrete. In total seven slabs were cast of fibre reinforced self-compacting concrete to validate the numerical framework and to study the effect of apparent slip near formwork on the fibre orientation and thus on the mechanical properties of the material. The slab castings were done in cooperation with Norwegian University of Science and Technology and in cooperation with Danish Technological Institute.

1.8 Limitations

Limited available computational power is a decisive factor for any design of a numerical simulation. We believe that the developed numerical framework is a reasonable trade-off between the accuracy and efficiency. The developed

numerical framework is capable of simulating thousands of immersed particles, such as fibres or aggregates, per computational core in a reasonable computational time. Tens or hundreds of thousands of the immersed particles can be then simulated using tens of computational cores in parallel. Using 32 computational cores, we were able to simulate at maximum approximately 100,000 immersed fibres. There are millions of aggregates in a cubic metre of concrete. The numerical framework is therefore capable of simulating only the largest fraction of the aggregates. Due to the computational resource limitations, many physical phenomena present in the flow of fibre reinforced self-compacting concrete had to be neglected or simplified. As an example, the numerical framework is currently not able to simulate multiphase flow, entrapped air bubbles, deformable immersed particles or arbitrarily shaped immersed particles. The scope of the research was further limited due to the time restrictions. Phenomena such as time dependent behaviour, heat transfer, thixotropy and many others were not studied during the research project. The numerical framework was further verified only on a limited set of examples and experiments.

1.9   Outline of the thesis

- Chapter 1: "Introduction"

  - This section introduces the research topic of the thesis. A brief state-of-the-art of the fibre reinforced self-compacting concrete is given with a primary focus on explaining the various aspects of fibre orientation.

- Chapter 2: "Journal paper 1"

  - The first journal article introduces the overall numerical framework that was developed to allow for the numerical simulations of explicitly represented rigid particles immersed in the self-compacting concrete.

- Chapter 3: "Journal paper 2"

  - The second journal article focuses on the accuracy of drag forces acting on rigid fibres immersed in Newtonian and non-Newtonian fluid. A correction function was proposed to correct drag forces acting on fibres of sub-grid size diameter. The proposed correction function was further validated both for the Newtonian and the Bingham plastic fluid.

- Chapter 4: "Journal paper 3"

    - The third journal article discusses the importance of the Navier's slip length boundary condition for the case of heterogeneous fluids such as self-compacting concrete. A method to incorporate the Navier's slip boundary condition into the Lattice Boltzmann method was proposed. The proposed method was validated both for Newtonian and Bingham plastic fluids.

- Chapter 5: "Conference paper 1"

    - The first conference paper shows the ability of the numerical framework to properly simulate the casting process of fibre reinforced self-compacting concrete. A plate was cast and cut into standard sized beams. The beams were then CT scanned. Result of the CT scanning was then compared to predictions of the numerical simulation.

- Chapter 6: "Conference paper 2"

    - The second conference paper validates the overall numerical framework against experiments of transparent gel Carbopol. Several L-Box castings were conducted using a suspension of stainless steel fibres immersed in the Carbopol gel. Results of the experiment were subsequently compared to predictions of the respective numerical simulations.

- Chapter 7: "Journal paper 4"

    - The fourth journal article discusses the importance of formwork surface on fibre orientation and consequently on the mechanical response of structures made of fibre reinforced self-compacting concrete. Experimental results of the fibre orientation obtained by the x-ray computed tomography were compared to respective numerical simulations of flow. Experimental results of the mechanical response were compared to numerical simulations of fracture behaviour.

- Chapter 8: "A collection of videos"

    - This chapter shows a range of videos collected during this research project. The videos indicate both experimental castings and numerical simulations.

- Chapter 9: "Conclusions and future perspectives"

    - Conclusions together with the future perspectives of the presented research project are given in this chapter.

1.10 Preface to the articles

This section presents information that might be of interest to better understand the following articles.

1.10.1 Technical information

The numerical framework presented in this thesis was developed in F# which is a strongly typed multi-paradigm programming language with a strong emphasis on the functional programming. The F# was developed by Microsoft and is part of the .NET family, similarly to C#, Visual Basic or Visual C++. The simplicity of the language together with novel features included in the core of the language such as units of measure allowed for fast and reliable development of the numerical framework.

The majority of the numerical simulations presented in this thesis were run on a server with 32 computation cores (4x Intel Xeon X7550, 64 GB RAM). The employed operating system was Microsoft Windows Server 2008R2.

1.10.2 Rescaling of the units of measurement

The fluid dynamics part of the framework is based on the Lattice Boltzmann method. The Lattice Boltzmann method origins from the kinetic theory of gases. The origin predefines several specific features of the method. One of the specific features is the fact that any physical problem must be rescaled into the Lattice Boltzmann units. The Lattice Boltzmann method as an example requires that the kinematic viscosity of the fluid oscillates around the value of 0.15 to obtain the highest accuracy and stability of the method. The maximum speed of the flow must be below the value of 0.05 to obtain a close to incompressible flow. Density of the fluid is usually set to 1. Any physical problem should be then rescaled to satisfy the aforementioned constrains.

As an example, let's assume a channel flow. The channel width is $w = 0.5\,\mathrm{m}$, the dynamic plastic viscosity is $\mu_{pl} = 50\,\mathrm{Pa.s}$, the yield stress is $\tau_y = 25\,\mathrm{Pa}$ and the density of the fluid is $\rho = 2500\,\mathrm{kg/m^3}$.

The rescaling of the physical problem often begins with the spatial and time discretization, based on the required resolution, efficiency and stability

of the numerical simulation. Let's assume that in the aforementioned example the channel width, w, was discretized into 20 lattice units. The spatial scaling factor is then $\delta_x = 20/0.5 = 40$, i.e. one physical meter corresponds to 40 lattice units.

The time discretization of the problem can be performed by relating time dependent physical quantities with their Lattice Boltzmann equivalents. As an example, velocity, acceleration or viscosity are good candidates. In the following articles, the apparent viscosity of the flow was often used for deriving the time scaling factor to assure a good accuracy of the numerical simulation in the flowing regions.

In the case of the Newtonian fluid, the apparent viscosity is equal to the viscosity of the fluid. In the case of the non-Newtonian fluid, such as Bingham plastic fluid, the apparent viscosity is variable in space and time and must be therefore estimated. For the case of the Bingham plastic fluid the apparent viscosity will be always higher than the plastic viscosity and depends on the shear rate, plastic viscosity and yield stress of the fluid. As a rule of thumb we assumed the apparent viscosity to be approximately 1.5 up to 2.0 multiple of the plastic viscosity of the Bingham plastic fluid.

In the aforementioned example, let's assume that the apparent viscosity was chosen to be $\mu_{ap} = 100\,\mathrm{Pa.s} = 2\mu_{pl}$. The apparent kinematic viscosity is then $\nu_{ap} = 100\,\mathrm{Pa.s}/2500\,\mathrm{kg/m^3} = 0.04\,\mathrm{m^2/s}$. The respective Lattice Boltzmann apparent viscosity is chosen to be $\nu_{ap,LB} = 0.15$. The time discretization can be then derived by comparing the physical apparent viscosity with its Lattice Boltzmann equivalent as $\delta_t = \nu_{ap}/\nu_{ap,LB} * \delta_x^2 = 0.04/0.15 * 40^2 = 427$. One second of the physical time is then equal to 427 time steps of the numerical simulation.

Having the spatial scaling factor δ_x and time scaling factor δ_t is satisfactory to rescale any physical quantity present in the following articles into the corresponding Lattice Boltzmann units and back. As and example, the physical yield stress in the aforementioned example can be rescaled into lattice units by $\tau_{y,LB} = \tau_y/\rho * \delta_x^2/\delta_t^2 = 25/2500 * 40^2/427^2 = 0.000088$.

Chapter 2

Journal paper 1

Title: Free surface flow of a suspension of rigid particles in a non-Newtonian fluid: a Lattice Boltzmann approach

Authors: Oldřich Švec, Jan Skoček, Henrik Stang, Mette R. Geiker and Nicolas Roussel

Published in: Journal of Non-Newtonian Fluid Mechanics, Volumes 179–180, July 2012, Pages 32-42, ISSN 0377-0257

Abstract

A numerical framework capable of predicting the free surface flow of a suspension of rigid particles in a non-Newtonian fluid is described. The framework is a combination of the lattice Boltzmann method for fluid flow, the mass tracking algorithm for free surface representation, the immersed boundary method for two-way coupled interactions between fluid and rigid particles and an algorithm for the dynamics and mutual interactions of rigid particles. The framework is able to simulate the flow of suspensions at the level of the largest suspended particles and, at the same time, the model is very efficient, allowing simulations of tens of thousands of rigid particles within a reasonable computational time. Furthermore, the framework does not require any fitting constants or parameters devoid of a clear physical meaning and it is stable, robust and can be easily generalized to a variety of problems from many fields.

Notation

Einstein summation convention is not used within the paper.

Fonts

v	scalar
$\mathbf{v}$, v_i, (v_1, v_2, v_3)	vector
I_{ij}, I	tensor

Superscripts

$\mathbf{x}^E$	Eulerian (fixed) node
$\mathbf{x}^L$	Lagrangian (moving) node

Subscripts

$\circ_p$	a quantity of solid particle p evaluated in its centre of gravity
$\circ_{p,n}$	a quantity of node n of solid particle p
$\circ_\alpha$	a quantity of lattice direction α
$\circ_{\bar{\alpha}}$	a quantity of lattice direction opposite to α
$\circ_f$	a quantity related to fluid
$\circ_s$	a quantity related to solids

Operators

δ_{ij}	Kronecker delta, $\delta_{ij} = 1 \Leftrightarrow i = j$ and $\delta_{ij} = 0$ otherwise
$\mathbf{v}.\mathbf{u}$	scalar product of two vectors
$\mathbf{v} \times \mathbf{u}$	cross product of two vectors
$\dot{\mathbf{v}}(t)$	time derivative of $\mathbf{v}(t)$
$\|\mathbf{v}\|$	Euclidean norm

2.1 Introduction

The free surface flow of suspensions plays an important role in many industrial and natural processes such as casting of concrete, mould filling, mud slides etc. An accurate description of the flow, often in complex geometries, is therefore required. Analytical and experimental approaches have a limited applicability and not negligible financial and time costs. Numerical modelling can therefore provide a reasonable substitute. We have developed a numerical framework capable of simulating a free surface flow of a suspension of rigid particles (called inclusions in this paper) in a non-Newtonian fluid. The presented framework is rather general and can easily be applied to a variety of problems in many fields.

As far as we know, there is no published contribution that would include an explicit representation of inclusions into a free surface flow of a non-Newtonian fluid and, at the same time, with the capability of simulating tens

of thousands of inclusions within a reasonable time. Our goal was therefore to create such a numerical framework. We aimed to properly capture the main phenomena at the scale of the largest inclusions, such as blocking of inclusions behind obstacles, mutual interactions among inclusions, mutual interactions between the inclusions and the fluid, etc.

We designed the framework with emphasis on its overall accuracy and, at the same time, its efficiency. The common denominator of all the algorithms and methods we chose is therefore simplicity and numerical effectiveness. Further, we tried to use models that are versatile and robust allowing application of the framework to a variety of problems.

In the presented framework, we chose and combined the Lattice Boltzmann Method (LBM) used for simulating the flow of the non-Newtonian fluid, a mass tracking algorithm representing the fluid-gas interface, an Immersed Boundary Method (IBM) used to simulate the two-way coupled interaction of fluid and inclusions and an algorithm for the dynamics and mutual interactions of inclusions.

Fluid dynamics is traditionally described by macroscopic partial differential Navier-Stokes equations. Individual methods such as the finite difference method, the finite volume method, the finite elements method, or the smooth-particle hydrodynamics method are differentiated only by the way they solve the Navier-Stokes equations. These approaches formulate the problem by means of macroscopic quantities such as macroscopic velocity or pressure fields. We decided to follow a completely different and historically younger approach called the LBM (Wolf-Gladrow, 2000). The method originated towards the end of 1980s when cellular automata began to be applied to the field of fluid dynamics. Originally, researchers dealt with lattice gas cellular automata and only in the beginning of 1990s the LBM was developed and applied to the field of fluid dynamics, see e.g. Chen and Doolen (1998); Aidun and Clausen (2010) for an overview of the history of the method. The LBM, contrary to the aforementioned traditional methods, is based on Boltzmann equations and thus on the theory of ideal gases. The method does not primarily work with macroscopic quantities but rather with mesoscopic particle distribution functions. We chose the LBM due to its effectiveness, a relatively simple implementation and straightforward representation of the free surface.

There are several ways to simulate multiple phases in the field of fluid dynamics. A multiphase algorithm (Gunstensen and Rothman, 1992) where all the phases, e.g. fluid and gas, are fully tracked is probably the most straightforward way. Such an approach provides the highest accuracy at the expense of high computational costs and possible stability issues for phases with a high contrast in their properties. Free surface algorithms, on the

other hand, neglect one of the phases, usually the gas. The mass tracking algorithm (Körner et al., 2005) we decided to use is one of the simplest and fastest algorithms that conserves mass precisely.

Modelling of the two-way coupled interaction between inclusions and the fluid significantly influences the accuracy, effectiveness and applicability of the model. Inclusions are commonly discretized by the same grid as is used in the LBM for fluid dynamics (Lallemand and Luo, 2003; Ladd, 2006a,b) and the interactions between the fluid and the inclusions are modelled in a similar manner to the bounce-back scheme discussed in Section 2.2.1. The bounce-back based interactions are efficient and accurate. On the other hand, the bounce-back scheme requires a fine discretization of inclusions and therefore a fine discretization of the entire domain. Too coarse discretization leads to distorted shapes of inclusions or even to stability issues (Feng and Michaelides, 2009; Ladd and Verberg, 2001). The need of the fine discretization significantly reduces the applicability of such an approach and exclude real-world simulations with thousands of inclusions. We therefore decided to implement an alternative method, the so-called Immersed Boundary Method with direct forcing (IBM) (Feng and Michaelides, 2005, 2009; Shu et al., 2007; Uhlmann, 2005; Wu and Shu, 2009, 2010).

Following Baraff (1997a), a numerically integrated Newton's second law was used to describe dynamics of inclusions. Continuous force interactions and direct collisions approximated by impulses (Baraff, 1997b) were used to mimic mutual interactions among inclusions.

During the development of our framework, we experienced difficulties in gathering and combining methods and approaches from various literature sources into a single frame. In this paper, we therefore introduce and describe the entire framework, the individual models and algorithms accentuating the experience we gained during the development of the framework. The paper is organized in the following way.

Section 2.2 describes our model and the methods we adopted to derive it. This section describes the LBM used as the fluid dynamics solver (Section 2.2.1), the dynamics of inclusions (Section 2.2.2) and the two-way coupled interactions between fluid and inclusions solved by the IBM (Section 2.2.3). Section 2.3 illustrates the applicability of the model by two examples. In the first example, empirical slump tests [1] of Bingham plastic with and without inclusions of various shapes were simulated. This example demonstrates the free surface algorithm and the non-Newtonian behaviour. In the case of the suspension, the effect of inclusions on the effective yield

---

[1]A standard test that involves pouring a given volume of a fluid from a given form (slump cone) and measuring its spread

stress and overall effectiveness of the model are discussed. The second example investigates the effect of inclusions on the effective properties of the resulting suspension and, among others, demonstrates the accuracy of the two-way coupled interactions between the fluid and inclusions and the accuracy of the mutual interactions among inclusions.

2.2 Framework description

Our primary goal was to develop a numerical framework capable of simulating a three dimensional free surface flow of a suspension of inclusions (rigid particles) of an arbitrary shape in a homogeneous non-Newtonian fluid. We aimed to explicitly simulate the effects of inclusions on the flow and therefore assumed that interactions between the inclusions and the fluid were two-way coupled. To simplify the description of the complex problem, we divided the overall framework, as well as this Section, into the 3 main logical levels shown in Figure 2.1:

a) **Level of fluid:** Free surface flow of a non-Newtonian fluid is solved at this level. The LBM is used as the fluid dynamics solver whereas the mass tracking algorithm describes the free surface of the flow. The current state of the fluid (velocity and pressure field) is sent to the level of fluid - inclusions interaction where an external force field is calculated and sent back to the level of fluid. The level of fluid is fully described in Section 2.2.1.

b) **Level of inclusions:** The dynamics of the inclusions of exact analytical shapes is calculated by solving Newton's equations of motion. Interactions among the inclusions and between the inclusions and the boundaries (such as walls etc.) are also solved. The current state of the inclusion (position, orientation etc.) is sent to the level of fluid - inclusions interaction where external interaction forces are calculated and sent back to the level of inclusions. The level of inclusions is fully described in Section 2.2.2.

c) **Level of fluid - inclusions interaction:** This intermediate level provides a two-way communication channel between the level of fluid and the level of inclusions. We have used the IBM with direct forcing to accommodate the communication between the two levels. Therefore, the communication is realized via force interactions. No-slip boundary condition between the fluid and the inclusions is assumed. To satisfy this condition, an interaction force field is created based on the current

state of fluid and the current state of inclusions and sent back to the level of fluid and the level of inclusions. The level of fluid - inclusions interaction is fully described in Section 2.2.3.
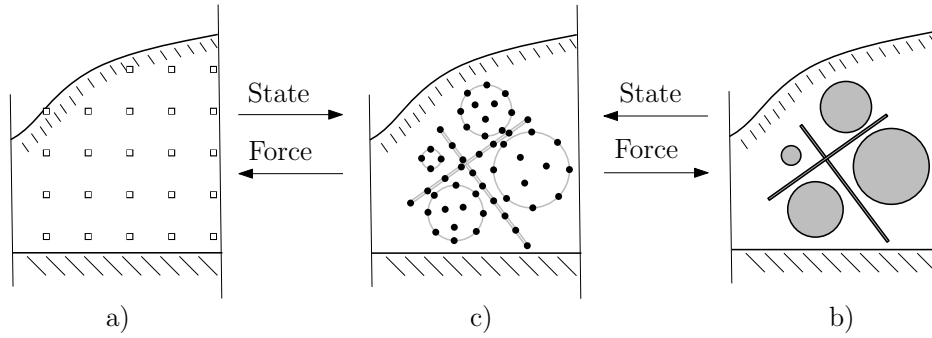

Figure 2.1: *Layout of the framework. a) Level of fluid, b) Level of inclusions, c) Level of fluid - inclusions interaction.*

2.2.1   Level of fluid: lattice Boltzmann method

The LBM, as discussed in Section 2.1, is based on Boltzmann equations and thus on the theory of ideal gases. The method does not primarily work with macroscopic quantities but rather with mesoscopic particle distribution functions. These can be seen as clouds of microscopic particles, e.g. molecules, chaotically moving in space. Space is commonly discretized into square (2D domain) or cubic Eulerian cells forming a fixed Cartesian grid (see Figure 2.2a). Eulerian nodes, $\mathbf{x}^E \in \Omega^E$, are placed into the centre of each cell and a lattice is formed by connecting the nearest Eulerian nodes. The movement of the microscopic particles is restricted onto the lattice directions, α, which leads into a discretization of continuous particle distribution functions into only a few particle distributions, $f_\alpha(\mathbf{x}^E, t)$, associated with lattice velocities, $\mathbf{c}_\alpha$. See Figure 2.2b) for a 2D example. There are several lattice types, differentiated on by the shape of the lattice. The $D2Q9$ and $D3Q15$, where D and Q stand for the dimension of the problem and the number of lattice velocities, are two of the most common types adopted.

The vertical and horizontal spacings of the nodes, the reference density of the fluid, $\rho_{f,0}$, and the length of the time step are usually set to unity for the most simple and common lattice types and the simulated problem is scaled accordingly. All quantities are therefore assumed to be dimensionless in the following text. The provided description of the LBM is general and

independent of the lattice used, provided that the reference fluid density, time step and spacing of the nodes are normalized to unity as described above. All the equations presented in this section can be found e.g. in Latt (2007), if not stated otherwise.
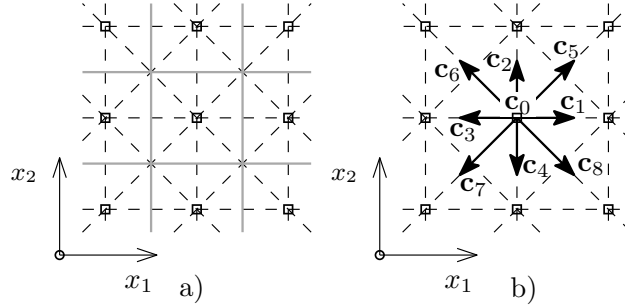
Figure 2.2: *a) Schematic representation of the D2Q9 lattice. Square marks stand for nodes, grey lines for cell boundaries and dashed lines for the lattice. b) Set of corresponding lattice velocity vectors, $\mathbf{c}_\alpha$, in a node.*

An evolution of the particle distributions in space and time is expressed by the lattice Boltzmann equation

$$\underbrace{f_\alpha\left(\mathbf{x}^E + \mathbf{c}_\alpha, t+1\right) = f_\alpha\left(\mathbf{x}^E, t\right)}_{\text{streaming}} + \underbrace{f_\alpha^{Ext}(\mathbf{x}^E, t)}_{\text{forcing}} + \underbrace{\Omega_\alpha\left(\mathbf{x}^E, t\right)}_{\text{collision}} . \qquad (2.1)$$

The equation consists of the streaming part, the forcing term and the collision part. The streaming part represents propagation of particle distributions from one node to another along the lattice links. The lattice velocities are chosen in such a way that a particle distribution streams from one node to another node during the unit time step. The forcing term accounts for the effect of an external force in the following way (Mohamad and Kuzmin, 2010; He et al., 1997; Guo et al., 2002)

$$f_\alpha^{Ext}\left(\mathbf{x}^E, t\right) = 3w_\alpha \mathbf{c}_\alpha.(\mathbf{F}^{fluid}\left(\mathbf{x}^E, t\right) + \mathbf{F}^{ext}\left(\mathbf{x}^E, t\right)), \qquad (2.2)$$

where w_α stands for weights defined by the type of the lattice and is defined for the adopted lattice later on in Eq. (2.12). $\mathbf{F}^{fluid}\left(\mathbf{x}^E, t\right)$ is a force coming from the level of fluid -inclusions interaction as described in Section 2.2.3. $\mathbf{F}^{ext}\left(\mathbf{x}^E, t\right)$ represents any other external force such as gravity.

The collision part mimics real collisions of the microscopic particles. The collisions are difficult to express explicitly and, therefore, an approximation of the collisions in the form of collision operator, $\Omega_\alpha\left(\mathbf{x}^E, t\right)$, was introduced into the LBM. We used one of the simplest collision operators, the so-called

BGK operator, see e.g. Chen and Doolen (1998). The BGK operator linearly deforms the actual particle distributions towards an equilibrium state. The operator reads

$$\Omega_\alpha \left(\mathbf{x}^E, t\right) = \frac{f_\alpha^{eq} \left(\mathbf{u}_f, \rho_f\right) - f_\alpha \left(\mathbf{x}^E, t\right)}{\tau \left(\mathbf{x}^E, t\right)}. \tag{2.3}$$

where $\mathbf{u}_f = \mathbf{u}_f \left(\mathbf{x}^E, t\right)$ and $\rho_f = \rho_f \left(\mathbf{x}^E, t\right)$ are the local macroscopic velocity and density of the fluid, respectively. The equilibrium state is represented by equilibrium particle distributions, $f_\alpha^{eq} \left(\mathbf{u}_f, \rho_f\right)$, which are derived from the Maxwell-Boltzmann equation. The equilibrium particle distributions have in the simplest case the following form

$$f_\alpha^{eq} \left(\mathbf{u}_f, \rho_f\right) = \rho_f w_\alpha \left(1 + 3\mathbf{c}_\alpha.\mathbf{u}_f + \frac{9}{2} \left(\mathbf{c}_\alpha.\mathbf{u}_f\right)^2 - \frac{3}{2}\mathbf{u}_f.\mathbf{u}_f\right) . \tag{2.4}$$

The local densities and velocities of the fluid are computed as the first two moments of the particle distributions

$$\rho_f \left(\mathbf{x}^E, t\right) = \sum^\alpha f_\alpha \left(\mathbf{x}^E, t\right), \tag{2.5}$$

$$\mathbf{u}_f \left(\mathbf{x}^E, t\right) = \frac{\sum^\alpha f_\alpha \left(\mathbf{x}^E, t\right) \mathbf{c}_\alpha}{\rho_f \left(\mathbf{x}^E, t\right)} .$$

For isothermal conditions, the local pressure is expressed as $p_f \left(\mathbf{x}^E, t\right) = c_s^2 \rho_f \left(\mathbf{x}^E, t\right)$ where c_s is the speed of sound in the given lattice.

The rate of the deformation of the particle distributions towards the equilibrium state is introduced by relaxation time, $\tau \left(\mathbf{x}^E, t\right)$. The relaxation time is computed from the local macroscopic kinematic viscosity of the fluid, $\nu \left(\mathbf{x}^E, t\right)$, by the following relation

$$\tau \left(\mathbf{x}^E, t\right) = \frac{1}{2} + 3\nu \left(\mathbf{x}^E, t\right) , \tag{2.6}$$

For a non-Newtonian fluid, the kinematic viscosity is a function of the shear rate tensor, $\dot{\gamma}_{ij} \left(\mathbf{x}^E, t\right)$, and the stress deviator tensor, $S_{ij} \left(\mathbf{x}^E, t\right)$. These tensors are approximated, as described e.g. in Mei et al. (2002), by

$$\dot{\gamma}_{ij} \left(\mathbf{x}^E, t\right) \approx \frac{3}{2\tau \left(\mathbf{x}^E, t - 1\right)} \sum^\alpha c_{i,\alpha} c_{j,\alpha} f_\alpha^{neq} \left(\mathbf{x}^E, t\right) , \tag{2.7}$$

$$S_{ij} \left(\mathbf{x}^E, t\right) \approx \left(1 - \frac{1}{2\tau \left(\mathbf{x}^E, t - 1\right)}\right) \sum^\alpha \left(c_{i,\alpha} c_{j,\alpha} - \frac{\delta_{ij}}{Dim}\mathbf{c}_\alpha.\mathbf{c}_\alpha\right) f_\alpha^{neq} \left(\mathbf{x}^E, t\right) , \tag{2.8}$$

where Dim is the dimension of the problem and

$$f_\alpha^{neq} \left(\mathbf{x}^E, t\right) = f_\alpha \left(\mathbf{x}^E, t\right) - f_\alpha^{eq} \left(\mathbf{u}_f, \rho_f\right) \tag{2.9}$$

is the non-equilibrium part of the particle distributions.

Implementation of the non-Newtonian behaviour - Bingham plastic

In the case of a non-Newtonian fluid, the apparent viscosity of the fluid, ν_{app}, is a function of the shear rate and stress deviator tensors. The tensors can be evaluated by Eqs. (2.7) and (2.8) and the apparent relaxation parameter, τ_{app}, can be evaluated from the apparent viscosity using Eq. (2.6). However, the value of the relaxation time influences the behaviour of the LBM. The relaxation time has to be greater than 0.5, provides an optimal accuracy for Newtonian fluids at around 0.8 (Latt, 2007), turns the LBM into the so-called lattice kinetic scheme (Inamuro, 2002) when equal to 1 and significantly reduces the accuracy and stability of the method for larger values (Latt, 2007).

Due to the kinematic nature of the LBM and due to the limited range of applicable relaxation times, behaviour of the Bingham plastic used in Section 2.3 cannot be modelled exactly. Recently, a lot of effort has been given into investigations of modelling of Bingham plastic rheology by the LBM, see e.g. Vikhansky (2008); Ohta et al. (2011); Chai et al. (2011); Leonardi et al. (2011), resulting in an iterative solution (Vikhansky, 2008) of the problem or resulting in various regularization and stabilization techniques in the remaining works. We decided, however, to use the most straightforward and "naive" implementation of the Bingham plastic. Since there always exist the bottom and upper limits of the relaxation time, i.e. $\tau_{min} \leq \tau_{app} \leq \tau_{max}$, where τ_{max} is the maximum allowed relaxation time with respect to accuracy and stability, we decided to implement the Bingham plastic as essentially a tri-viscosity fluid with an apparent viscosity defined as

$$\nu_{app} = \begin{cases} \frac{1}{3}\left(\tau_{max} - \frac{1}{2}\right) & \text{if} \quad \tau_{app} \geq \tau_{max} \\ \frac{1}{3}\left(\tau_{min} - \frac{1}{2}\right) & \text{if} \quad \tau_{app} \leq \tau_{min} \\ \nu_{pl} + \frac{S_{yield}}{\dot{\gamma}} & \text{otherwise,} \end{cases} \tag{2.10}$$

where $\dot{\gamma} = \sqrt{2\sum^i \sum^j \dot{\gamma}_{ij}\dot{\gamma}_{ji}}$ is the second invariant of the shear rate tensor and S_{yield} and ν_{pl} are the yield stress and plastic kinematic viscosity of the Bingham plastic, respectively. We found that $\tau_{min} = 0.501$ and $\tau_{max} = 8$ gives satisfactory results and stability for the investigated problems.

Applied parameters

We adopted the $D3Q15$ lattice type in our framework - a three dimensional lattice with 15 lattice velocities defined as

$$\mathbf{c}_\alpha^T = \begin{cases} (0,0,0) & \alpha = 0 \\ (\pm 1, 0, 0), (0, \pm 1, 0), (0, 0, \pm 1) & \alpha = 1 \dots 6 \\ (\pm 1, \pm 1, \pm 1) & \alpha = 7 \dots 14 \end{cases} \tag{2.11}$$

The speed of sound is then $c_s^2 = \frac{1}{3}$ and the weights introduced in Eq. (2.4) read

$$w_\alpha = \begin{cases} 2/9 & \text{if} \quad \|\mathbf{c}_\alpha\| = 0 \\ 1/9 & \text{if} \quad \|\mathbf{c}_\alpha\| = 1 \\ 1/72 & \text{if} \quad \|\mathbf{c}_\alpha\| = \sqrt{3} \end{cases} \tag{2.12}$$

Boundary conditions

Periodic boundaries are the simplest boundary conditions used in the LBM. When a particle distribution needs to be retrieved from a node lying outside of the computational domain, a node at the "opposite" side of the domain is taken instead. Details can be found e.g. in Sukop and Thorne (2005).

Rigid obstacles with no-slip contacts are simulated using the so-called bounce-back scheme. In the most simple case, the boundary of a non-moving obstacle lies halfway between two neighbouring nodes. The streaming part of Eq. (2.1) is then modified into

$$f_\alpha \left(\mathbf{x}^E + \mathbf{c}_\alpha, t + 1 \right) = f_{\bar{\alpha}} \left(\mathbf{x}^E + \mathbf{c}_\alpha, t \right), \tag{2.13}$$

where $\bar{\alpha}$ is a lattice direction opposite to α. The reader is referred to Mei et al. (1999) for more complex bounce-back schemes taking into account the curvature or movement of obstacles.

Velocity or pressure boundaries are achieved by modifying the particle distributions in the boundary nodes during the streaming and/or collision of the particle distributions. Many different modifications schemes with different accuracies and assumptions can be found in the literature, e.g. see Latt and Chopard (2008) for comparison of the most commonly adopted velocity boundary conditions.

Free surface

The mass tracking algorithm (Körner et al., 2005) we decided to use is one of the simplest and fastest algorithms that conserves mass precisely. The adopted mass tracking algorithm is applied directly at the level of the LBM, so the algorithm mimics the free surface by modifying the particle distributions. Lattice cells are differentiated into fluid, gas and interface cells, see Figure 2.3. Gas cells do not contain any particle distributions and thus carry no information, i.e. the LBM is not applied in the gas cells. Fluid cells behave as ordinary LBM cells.

Interface cells form a boundary layer between gas cells and fluid cells. This means that there must always be an interface cell between a gas cell and a fluid cell. Interface cells are treated in the same manner as fluid cells
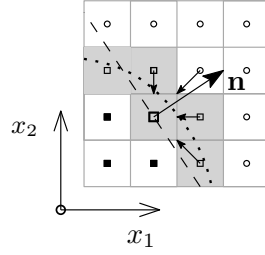
Figure 2.3: *Mass tracking algorithm scheme. Nodes with filled square marks belong to fluid cells, interface cells are grey and circle nodes belong to gas cells. Dotted curve is the actual free surface. Dashed line divides the space into positive and negative half-spaces based on the vector* **n** *normal to the free surface. Small arrows indicate particle distributions to be reconstructed for the investigated cell (larger hollow square mark).*

with an additional information, namely a local mass of the fluid in the cell, $m\left(\mathbf{x}^{E}, t\right)$.

Consider one interface cell at the position $\mathbf{x}^{E}$. An inflow of particle distributions coming from the neighbouring cells and an outflow of particle distributions leaving the current interface cell take place during the streaming part of Eq. (2.1). Difference between the inflow and outflow of the particle distributions leads to change of the mass of the current interface cell in the following way

$$m\left(\mathbf{x}^{E}, t+1\right) = m\left(\mathbf{x}^{E}, t\right) + \sum^{\alpha} b_{\alpha}\left[f_{\bar{\alpha}}\left(\mathbf{x}^{E} + \mathbf{c}_{\alpha}, t\right) - f_{\alpha}\left(\mathbf{x}^{E}, t\right)\right], \qquad (2.14)$$

where f_{α} and $f_{\bar{\alpha}}$ are particle distributions with opposite directions and

$$b_{\alpha} = \begin{cases} \frac{1}{2}\left[m\left(\mathbf{x}^{E}, t\right) + m\left(\mathbf{x}^{E} + \mathbf{c}_{\alpha}, t\right)\right] & \text{if } \left(\mathbf{x}^{E} + \mathbf{c}_{\alpha}, t\right) \text{ is an interface cell} \\ 1 & \text{if } \left(\mathbf{x}^{E} + \mathbf{c}_{\alpha}, t\right) \text{ is a fluid cell} \\ 0 & \text{if } \left(\mathbf{x}^{E} + \mathbf{c}_{\alpha}, t\right) \text{ is a gas cell} \end{cases}$$

$$(2.15)$$

The interface cell becomes a fluid cell when the mass reaches its density, i.e. when $m\left(\mathbf{x}^{E}, t\right) \geq \rho_{f}\left(\mathbf{x}^{E}, t\right)$, and vice versa the interface cell becomes a gas cell when the mass drops down to zero, $m\left(\mathbf{x}^{E}, t\right) \leq 0$. In such cases, some of the surrounding cells are converted into interface cells in order to assure consistency of the boundary layer, i.e. to avoid a direct contact of gas and fluid cells.

It is inevitable that the mass of an interface cell drops down below zero or overshoots density of the interface cell. This is of course not realistic, as there is for example no clear explanation for negative mass. It must be however

stressed that this is caused only by the discrete nature of the method and could be avoided by using a continuum time instead. In the discrete world, the negative mass or the exceeding mass has to be corrected to maintain the conservation of mass of the fluid. The shortage or surplus of the mass caused by the conversion of the interface cell to the fluid or gas cells are therefore usually distributed to surrounding interface cells. Due to domain parallelism we implemented, all the surplus or shortage of the mass was distributed uniformly to all interfaces.

During the streaming part of Eq. (2.1), some of the particle distributions should arrive at the current interface cell from gas cells. These particle distributions do not exist and therefore need to be reconstructed. Following Körner et al. (2005), it is assumed that velocities of the fluid and velocities of the gas are equal at the free surface, enforcing a no-slip boundary condition. It is further assumed that the density of the gas at the free surface is equal to $\rho_{gas} = 1$. Assuming that the pressure of gas equals to the pressure of fluid at the free surface, the pressure equality can be expressed in the form of forces acting between the gas and the fluid. This makes it possible to define the reconstructed particle distributions arriving from the gas as

$$f_\alpha \left(\mathbf{x}^E, t \right) = f_\alpha^{eq} \left(\rho_{gas}, \mathbf{u}_f \right) + f_{\bar{\alpha}}^{eq} \left(\rho_{gas}, \mathbf{u}_f \right) - f_{\bar{\alpha}} \left(\mathbf{x}^E, t \right) \qquad (2.16)$$

Some of the particle distributions arriving from the neighbouring interface cells must also be reconstructed. Consider a vector normal to the free surface of the fluid positioned at the current interface cell and pointing to the gas (vector $\mathbf{n}$ depicted in Figure 2.3). All the particle distributions arriving from the interface nodes located in the positive half-space defined by the normal vector must be reconstructed as well, as indicated in Figure 2.3 by small arrows.

It may happen during the computation that an interface cell becomes surrounded only by one type of cells, either fluid or gas cells. Such interface cells are called artefacts. These artefacts are removed by converting the interface cell either into a fluid or gas cell and distributing the mass shortage or surplus evenly into all interface cells.

Remarks

We have introduced and described the LBM that we apply to the isothermal fluid dynamics of a non-Newtonian fluid with a free surface. Most of the equations are simple and straightforward to implement.

It is worth noting how different the LBM is compared to traditional fluid dynamics solvers. Its alternative "bottom-up" approach helps to better un-

derstand the underlying physics of a given problem, especially the influence of microscopic properties on the macroscopic counterparts.

Take the relaxation time presented in Eq. (2.6) as an example. The higher the relaxation time, the fewer collisions of microscopic particles and the lower the damping of information. This corresponds to the notion of macroscopic viscosity, i.e. resistivity of the fluid to the rate of shearing.

The effectiveness of the method is illustrated by e.g. the computation of the local shear rate, see Eq. (2.7). The shear rate is commonly computed as a difference of neighbouring velocities of the fluid and thus in a purely non-local manner. In contrast, in the case of the LBM the shear rate is computed from the local non-equilibrium particle distributions. This favourably influences the computational demands of the method and provides some information on what the equilibrium state actually is (shear rate free state).

There are, however, some drawbacks of the method. Since the method primarily works with particle distributions, every macroscopic phenomenon must be converted into the micro-world and vice versa. Unfortunately, there is often no unique way to make such a conversion. Take the external forces as an example. Many different ways of incorporating the external forces exist in the LBM. We briefly compared 4 different force terms (Mohamad and Kuzmin, 2010; Martys and Douglas, 2001) and we observed, as in Feng and Michaelides (2009), that differences among the different approaches were negligible for the cases we investigated. We therefore decided to use the most simple and efficient yet accurate force term presented in Eq. (2.2). Similarly, a variety of LBM boundary conditions attempting to mimic a single macroscopic phenomenon exist. The boundary with a prescribed velocity mentioned in Section 2.2.1 is an example of this.

2.2.2   Level of inclusions

Dynamics of inclusions together with all the interactions of the inclusions are solved at this level. We assumed the inclusions to be rigid bodies of a simple analytical shape (sphere, ellipsoid, cylinder) with the ability to move, rotate and interact among each other, with fluid and walls, see Figure 2.1b). Applying the Newton's second law, the dynamics of inclusions is described by Baraff (1997a)

$$m_p \dot{\mathbf{u}}_p(t) = \mathbf{F}_p^{tot}(t) \tag{2.17}$$

$$\mathsf{I}_p(t)\dot{\boldsymbol{\omega}}_p(t) + \boldsymbol{\omega}_p(t) \times (\mathsf{I}_p(t)\boldsymbol{\omega}_p(t)) = \mathbf{T}_p^{tot}(t), \tag{2.18}$$

where m_p stands for the mass of the p-th inclusion, $\mathbf{u}_p(t)$ is the linear velocity, $\boldsymbol{\omega}_p(t)$ depicts the angular velocity and $\mathsf{I}_p(t)$ represents the moment of inertia

tensor. The total force and torque acting on inclusions, $\mathbf{F}_p^{tot}(t)$ and $\mathbf{T}_p^{tot}(t)$, consist of three contributions.

$$\mathbf{F}_p^{tot}(t) = \mathbf{F}_p^{fluid}(t) + \mathbf{F}_p^{int}(t) + \mathbf{F}_p^{ext}(t) \qquad (2.19)$$

$$\mathbf{T}_p^{tot}(t) = \mathbf{T}_p^{fluid}(t) + \mathbf{T}_p^{int}(t) + \mathbf{T}_p^{ext}(t). \qquad (2.20)$$

$\mathbf{F}_p^{fluid}(t)$ and $\mathbf{T}_p^{fluid}(t)$ are force and a torque coming from the mutual interaction between an inclusion and the fluid and are described in Section 2.2.3. $\mathbf{F}_p^{int}(t)$ and $\mathbf{T}_p^{int}(t)$ are interaction forces and torques among the inclusions and with boundaries which are discussed in Section 2.2.2. External forces and torques such as gravity are introduced by $\mathbf{F}_p^{ext}(t)$ and $\mathbf{T}_p^{ext}(t)$. All the vectors and the moment of inertia tensors are related to the centre of gravity of the inclusions unless otherwise stated. Eq. (2.18) contains second order tensors and is thus computationally intensive. In the case of a symmetrically shaped inclusion, the equation can be transformed to a local coordinate system of the inclusion where the moment of inertia tensor, $I_{ij,p}^l$, becomes diagonal and constant in time. The local form of Eq. (2.18) then splits into

$$\dot{\boldsymbol{\omega}}_p^l(t) = \begin{pmatrix} \frac{(I_{22,p}^l - I_{33,p}^l)\omega_{2,p}^l(t)\omega_{3,p}^l(t) + T_{1,p}^{tot,l}(t)}{I_{11,p}^l} \\ \frac{(I_{33,p}^l - I_{11,p}^l)\omega_{3,p}^l(t)\omega_{1,p}^l(t) + T_{2,p}^{tot,l}(t)}{I_{22,p}^l} \\ \frac{(I_{11,p}^l - I_{22,p}^l)\omega_{1,p}^l(t)\omega_{2,p}^l(t) + T_{3,p}^{tot,l}(t)}{I_{33,p}^l} \end{pmatrix} \qquad (2.21)$$

where $\omega_{i,p}^l(t)$ and $T_{i,p}^l(t)$ are components of the local angular velocity and torque. Aside from Eq. (2.21), all the computations were done in the global coordinate system. The orientation of the inclusions and the evolution of the orientation and other transformations involving orientation were represented by means of quaternions. This provided superior stability, accuracy and lower computational demands compared to e.g. Eulerian angles.

During the numerical integration of Eqs. (2.17) and (2.21), the state of an inclusion and its derivatives must be computed. The state is defined by position $\mathbf{x}_p(t)$, orientation $\mathcal{Q}_p(t)$, linear velocity $\mathbf{u}_p(t)$ and angular velocity $\boldsymbol{\omega}_p(t)$ of the inclusion. Based on knowledge of the current state, derivatives of the state such as linear velocity $\mathbf{u}_p(t)$, angular velocity $\boldsymbol{\omega}_p(t)$, linear acceleration $\dot{\mathbf{u}}_p(t)$ and angular acceleration $\dot{\boldsymbol{\omega}}_p(t)$ are computed. The accelerations are computed based on the total force $\mathbf{F}_p^{tot}(t)$ and torque $\mathbf{T}_p^{tot}(t)$.

Various integration methods differ in the number of states and derivatives they use to update the current state to a new step. The simplest time integration scheme, i.e. the explicit forward Euler method, begins with the current state of the inclusion. Derivatives of the position and orientation, i.e. the linear and angular velocities, are taken from the previous time step

whereas the derivatives of the linear and angular velocities, i.e. the linear and angular accelerations are computed by Eqs. (2.17) and (2.18). A new state is then calculated from the current state and the derivatives of the current state.

Different Runge-Kutta integration schemes calculate the new state using a more sophisticated approach, namely using a linear combination of derivatives that are calculated at various states. The various states and their derivatives are computed using the Butcher tableau.

The unit time step of the fluid solver is often too coarse for the dynamics of inclusions and must be subdivided into several sub-steps, e.g. by Runge-Kutta Fehlberg numerical time integration scheme with an adaptive time step that we adopted. Such a numerical integration scheme ensures stability and accuracy of the simulation even for a highly non-linear behaviour, i.e. for inclusions with a relatively low mass or high aspect ratio.

Interactions among inclusions

An accurate and robust treatment of interactions among the inclusions and between the inclusions and other obstacles such as walls or reinforcement plays an important role in a proper description of the problem. We included two types of interactions in our framework, namely mutual instantaneous collisions of inclusions and continuous forcing of a general type ($\mathbf{F}_p^{int}(t)$ and $\mathbf{T}_p^{int}(t)$). An example of the continuous forcing could be a lubrication force correcting the fluid flow between two inclusions in the case when the two inclusions approach each other to a sub-grid distance (Nguyen and Ladd, 2002).

We approximated the instantaneous collisions by impulses. As time remains constant, the time dependency was excluded from the following notations for brevity. During each time sub-step, inclusions were first checked for overlapping (see Figure 2.4). When two overlapping inclusions, p and q, were
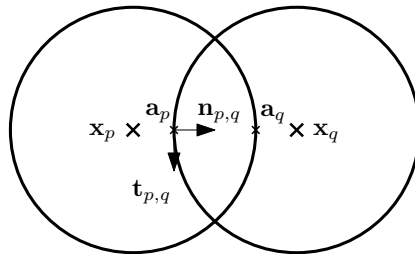
Figure 2.4: *Schematic representation of collision of two inclusions with overlapping.*

found, the impulse was computed and applied to both inclusions. $\mathbf{a}_p$ and $\mathbf{a}_q$ are points located on the surface of inclusion p and q and define a maximum overlapping of the inclusions (approximate points of contact). The velocities of the inclusions at these points are computed as $\mathbf{u}_{\mathbf{a}_p} = \mathbf{u}_p + \omega_p \times \mathbf{r}_p$ where $\mathbf{r}_p = \mathbf{a}_p - \mathbf{x}_p$ and similarly for $\mathbf{u}_{\mathbf{a}_q}$. The normal and tangent vectors of the contact are defined as

$$\mathbf{n}_{p,q} = \frac{\mathbf{a}_q - \mathbf{a}_p}{\|\mathbf{a}_q - \mathbf{a}_p\|} \tag{2.22}$$

and

$$\mathbf{t}_{p,q} = \mathbf{n}_{p,q} \times \left[\mathbf{n}_{p,q} \times \frac{\mathbf{u}_{\mathbf{a}_p} - \mathbf{u}_{\mathbf{a}_q}}{\|\mathbf{u}_{\mathbf{a}_p} - \mathbf{u}_{\mathbf{a}_q}\|} \right]. \tag{2.23}$$

The impulse on inclusion p caused by the collision with inclusion q, $\mathbf{j}_{p,q}$, is accordingly decomposed into normal and tangent impulses

$$\mathbf{j}_{p,q} = j_n \mathbf{n}_{p,q} + j_t \mathbf{t}_{p,q} = -\mathbf{j}_{q,p}. \tag{2.24}$$

These impulses are solved separately. The normal impulse obeys Newton's law of restitution and yields (Baraff, 1997b)

$$j_n = \frac{-(1+\varepsilon)(\mathbf{u}_{\mathbf{a}_p} - \mathbf{u}_{\mathbf{a}_q}) \cdot \mathbf{n}_{p,q}}{\left(\frac{1}{m_p} + \frac{1}{m_q}\right) + \left[\left(\mathsf{I}_p^{-1} \left(\mathbf{r}_p \times \mathbf{n}_{p,q} \right) \right) \times \mathbf{r}_p + \left(\mathsf{I}_p^{-1} \left(\mathbf{r}_q \times \mathbf{n}_{p,q} \right) \right) \times \mathbf{r}_q \right] \cdot \mathbf{n}_{p,q}}, \tag{2.25}$$

where ε is the coefficient of restitution. The tangent impulse is computed from an appropriate law of friction as $j_t = f(j_n, j_{t,max})$. The maximum allowable impulse, $j_{t,max}$, was then computed from Eq. (2.25), with $\mathbf{n}_{p,q}$ replaced by $\mathbf{t}_{p,q}$. The coefficient of restitution was set to $\varepsilon = 0$ as the tangent collisions were assumed to be plastic. The linear and angular acceleration of the inclusion was then computed using the resulting impulse vector and the linear and angular velocity were updated using an explicit forward Euler method. An example of the law of friction is given in Eq. (2.34).

We treated collisions of the inclusions with walls and other stationary obstacles in an identical manner. The mass and moment of inertia of the stationary obstacles were assumed to be infinite.

The complexity of distance computing among the inclusions are of an order of N^2, where N stands for the number of inclusions. We have included three main ingredients into our framework to limit the time consumption of the computations. Firstly, we split the computational domain into smaller sub-domains to allow for the parallelization of the code. The N^2 complexity was limited onto the smaller sub-domains as a side effect of the parallelization, i.e. the order of complexity became $(N/N_d)^2$, where N_d stands for the number of sub-domains. Secondly, we were holding a list of all potential

collisions of individual inclusions sorted by the time at which the collisions are predicted to happen. The length of the list is of an order of $(N/N_d)^2$. At each time step a fraction of the collisions related to that time step, $N_\% < 1$, was checked leading to an order of complexity equal to $N_\%(N/N_d)^2$. We have therefore substituted the computational complexity by an increased memory consumption. Finally, all the distance checks are based on analytical solutions, if the analytical solutions exist for the shapes in use. All the three ingredients make the computational time of the interactions marginal as discussed in Section 2.3.1.

We made several simplifications in our framework. For example, in some other approaches, when an overlapping of two inclusions is detected during the time integration, the time is reverted back to the last sub-step and the integration is redone with a shorter sub-step to precisely model the collision. We did not implement such a correction as we found the overlapping insignificant for our problems. We have further solved collisions explicitly one by one which may lead to extensive overlapping for larger time sub-steps and for denser systems of inclusions. Finally, the way we implemented the tangential component of the impulse into our framework is an approximation and a simplification of the real problem.

2.2.3 Level of fluid - inclusions interaction: Immersed Boundary Method

The IBM with direct forcing (Feng and Michaelides, 2005, 2009; Shu et al., 2007; Uhlmann, 2005; Wu and Shu, 2009, 2010) creates an interface between the level of fluid and the level of inclusions, i.e. description of the way the two levels communicate with each other. This communication is realized via interaction force fields used to mimic the real no-slip boundary conditions.

In the IBM, inclusions are discretized by a set of Lagrangian nodes, $\mathbf{x}_{p,n}^L(t)$, which are independent of the discretization of the fluid, as shown in Figure 2.5a) and Figure 2.1c). The force field is evaluated at these Lagrangian nodes. Velocity of the inclusions and velocity of the fluid should be equal in these nodes when assuming no-slip contact between the inclusions and the fluid. Nevertheless, differences in the velocities occur as the system evolves in discrete time steps. An interaction force is calculated from these differences and applied back both to the level of fluid and the level of inclusions.

The interaction forces between inclusions and fluid are computed in the following way. The velocity of the fluid and the velocity of the inclusions are evaluated in each Lagrangian node. The velocity of the inclusions in the

Lagrangian nodes is computed as

$$\mathbf{u}_{p,n}(t) = \mathbf{u}_p(t) + \boldsymbol{\omega}_p(t) \times (\mathbf{x}^L_{p,n}(t) - \mathbf{x}_p(t)), \qquad (2.26)$$

where $\mathbf{x}_p(t)$ denotes the centre of gravity of the inclusion. The velocity of the fluid at the Lagrangian nodes, $\mathbf{u}_f\left(\mathbf{x}^L_{p,n}(t), t\right)$, must be interpolated from the LBM nodes, $\mathbf{x}^E \in \Omega^E$, since the two types of nodes do not coincide. The interpolation is performed using a Dirac delta function as

$$\mathbf{u}_f\left(\mathbf{x}^L_{p,n}(t), t\right) = \int_\Omega \mathbf{u}_f(\mathbf{x}, t) D(\mathbf{x} - \mathbf{x}^L_{p,n}(t)) \, \mathrm{d}\mathbf{x} \qquad (2.27)$$

$$\approx \frac{\sum^{\mathbf{x}^E} \mathbf{u}_f(\mathbf{x}^E, t) D(\mathbf{x}^E - \mathbf{x}^L_{p,n}(t))}{\sum^{\mathbf{x}^E} D(\mathbf{x}^E - \mathbf{x}^L_{p,n}(t))}, \qquad (2.28)$$

where $D(\mathbf{x}^E - \mathbf{x}^L_{p,n}(t)) = D(\circ) = d(\circ_1)d(\circ_2)d(\circ_3)$ is the Dirac delta function. There exist several different Dirac delta functions (Yang et al., 2009) with various shapes and smoothing lengths. We adopted the following cosine Dirac delta function

$$d(\circ_i) = \begin{cases} 1 + \cos\left(\frac{\pi}{2}|\circ_i|\right) & \text{if } |\circ_i| < 2 \\ 0 & \text{otherwise.} \end{cases} \qquad (2.29)$$

The interaction force in the Lagrangian nodes is constructed on the basis of the difference between the velocity of the fluid and the velocity of the inclusion at these nodes. The simplest form of the force reads

$$\mathbf{F}^{fluid}_{p,n}(t) = \frac{\rho_{f,0}}{\Delta t}\left[\mathbf{u}_f\left(\mathbf{x}^L_{p,n}(t), t\right) - \mathbf{u}_{p,n}(t)\right]\Delta V_{p,n}, \qquad (2.30)$$

where $\Delta V_{p,n}$ is a volume associated with the n-th Lagrangian node (see Figure 2.5b). The reference density of the fluid, $\rho_{f,0}$, and the LBM time step, Δt, are set to unity, see Section 2.2.1.

The total interaction force and the torque between the inclusion and the fluid exerted on the $p - th$ inclusion are expressed as

$$\mathbf{F}^{fluid}_p(t) = \sum^n \mathbf{F}^{fluid}_{p,n}(t) \qquad (2.31)$$

$$\mathbf{T}^{fluid}_p(t) = \sum^n \left[\left(\mathbf{x}^L_{p,n}(t) - \mathbf{x}_p(t)\right) \times \mathbf{F}^{fluid}_{p,n}(t)\right] \qquad (2.32)$$

Eqs. (2.31) and (2.32) form an output which is sent back to the level of inclusions to Eqs. (2.19) and (2.20).

The total interaction force field between the inclusions and the fluid exerted on the LBM lattice nodes is obtained by an extrapolation of the forces

from the Lagrangian nodes to the LBM lattice nodes, similarly to Eqs. (2.27) and (2.28). The extrapolation is performed by means of the same Dirac delta function as

$$\mathbf{F}^{fluid}\left(\mathbf{x}^{E}, t\right) = -\sum^{p} \frac{\sum^{n}\left[\mathbf{F}_{p,n}^{fluid}\left(t\right) D(\mathbf{x}^{E} - \mathbf{x}_{p,n}^{L}(t))\right]}{\sum^{n} D(\mathbf{x}^{E} - \mathbf{x}_{p,n}^{L}(t))} \qquad (2.33)$$

Eq. (2.33) forms an output that is sent back to the level of fluid to Eq. (2.2).
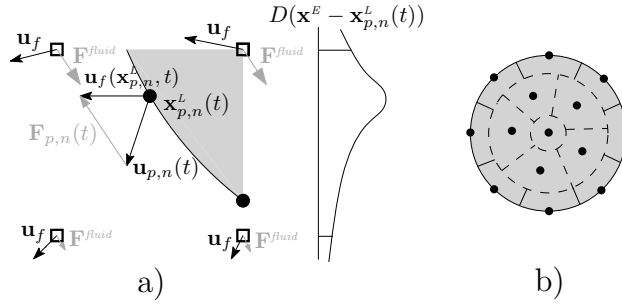
Figure 2.5: *a) Schematic representation of the IBM at a single Lagrangian node. Black and gray quantities are inputs and outputs of the method. b) Scheme of the uniform discretization of a circle by Lagrangian nodes (black circles) and corresponding volumes $\Delta V_{p,n}$.*

Remarks about the immersed boundary method

The IBM is a powerful method which makes the real-world simulations at the structural level achievable. The independent discretization of the fluid and the inclusions makes it possible to simulate inclusions of an arbitrary shape and size. It is even possible to simulate inclusions of a sub-grid size with a decreased accuracy, but not with a decreased stability (Švec et al., 2011). The IBM is computationally more expensive than the bounce-back scheme. On the other hand, due to its ability to use coarser grids for the fluid dynamics solver, the overall efficiency can increase by several orders of magnitude. We usually use inclusions of a size in a range of several lattice node spacings. The coarser computational grid results in an increased non-linearity of Newton's equations of motion of inclusions which is treated by the aforementioned numerical Runge-Kutta Fehlberg integration with adaptive time steps.

As for any other method, the IBM has several "problematic" features. One of them stems from the fact that there is no unique choice of the interpolating Dirac delta function. We briefly compared several types of the Dirac delta

functions which are mentioned in Yang et al. (2009). Our experience is that the larger the smoothing length of the function the slower the computation and the better the stability. The smaller the smoothing length the more concentrated forces are applied back to the level of fluid and the greater chance for instabilities. Eq. (2.29) has proven to be stable, accurate and with reasonable computational costs.

A more complex version of Eq. (2.30), where derivatives of velocity and pressure fields are not neglected, is described e.g. in Feng and Michaelides (2009). We compared the interaction force term presented in Eq. (2.30) with the more complex ones from Feng and Michaelides (2009) and found a negligible difference in the results for the cases we investigated. The increase in computational costs was, however, important and we therefore decided to use the simplified interaction force term.

Different choices of the volume associated with Lagrangian nodes, $\Delta V_{p,n}$, are reported in the literature. Some authors assume $\Delta V_{p,n} = 1$ (Aidun and Clausen, 2010), others assume a layer of a unit thickness at the surface of the inclusions (Feng and Michaelides, 2009). The volume of such a layer is divided uniformly between the Lagrangian nodes. In such an approach, the effect of the inertia of the internal fluid must be considered. This results in a more complex update of velocities of inclusions. In our simulations, we aimed to simulate many small sized inclusions. We therefore decided to distribute Lagrangian nodes uniformly within the volume of inclusions and the total volume of the inclusions was distributed uniformly among the Lagrangian nodes (see Figure 2.5b).

2.3 Applications

In this section, we demonstrate the applicability of the described framework by means of two examples. The first example simulates an empirical slump test of Bingham plastic. The first example, among others, demonstrates the accuracy of the free surface algorithm as well as the accuracy of the non-Newtonian behaviour. The second example investigates the effect of rigid inclusions on the effective viscosity of the suspension and therefore demonstrates and discusses the accuracy of the two-way coupled interactions and the accuracy of the mutual interactions among inclusions.

2.3.1 Study of the slump test

The slump test is a widely used method to measure workability and yield stress of homogeneous fluids or suspensions in industrial applications (Roussel

and Coussot, 2005). A primary goal of this study was to verify the correctness and the accuracy of the free surface algorithm and its coupling with the LBM (see Section 2.3.1). A secondary goal of this study was to indicate the overall accuracy of the framework on a more complex example with inclusions (see Section 2.3.1).

Homogeneous case

A free surface flow of a homogeneous non-Newtonian fluid was studied by means of a slump test. A standard slump cone (see BS EN 12350-2) as well as homogeneous fluid following a Bingham rheology were used during the simulation. The slump cone was discretized into $height \times bottom\,diameter \times top\,diameter = 75 \times 50 \times 25$ lattice units. Yield stress, plastic viscosity and density of the fluid were set to $8 \times 10^{-6}, 0.06$ and 1, respectively. The flow was driven by the gravity equal to 1.6×10^{-5}.

   The simulation started by an instantaneous release of the slump cone and terminated at the moment when the relaxation time of 90 % of the fluid cells reached $\tau_{max} = 8$ (see Section 2.2.1). Figure 2.6 shows the shape of the free surface in the initial state, after 0.16 s and 14.5 s of flowing.

$\qquad$ 0 s $\qquad\qquad\qquad$ 0.16 s $\qquad\qquad\qquad\qquad$ 14.5 s
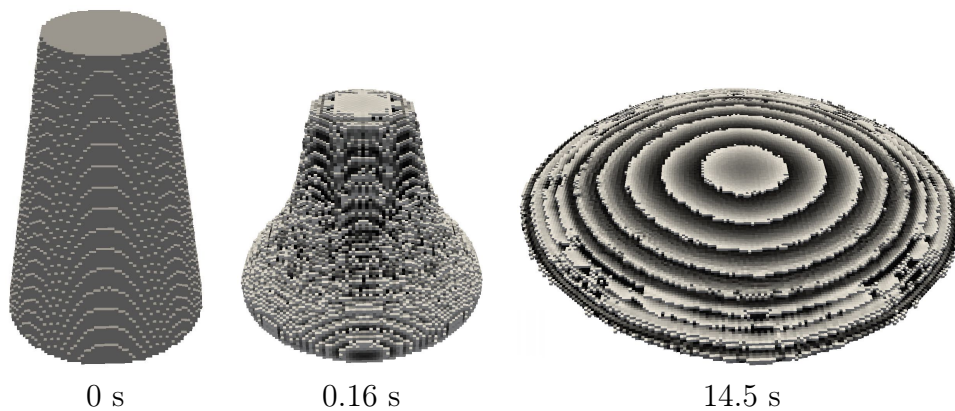
Figure 2.6: *3D view of the slump test in 3 different time steps (white = gas, black = fluid).*

   Figure 2.7 shows a comparison of the simulation with an analytical solution (Roussel and Coussot, 2005). The figure presents a final normalized height of fluid as a function of a normalized distance from the slump cone centre. The normalization was done with respect to the analytical solution. As can be seen in Figure 2.7, the final shape of the simulation favourably matches the analytical solution, proving the correct coupling of the LBM

with the free surface algorithm together with correctness of the non-Newtonian behaviour.
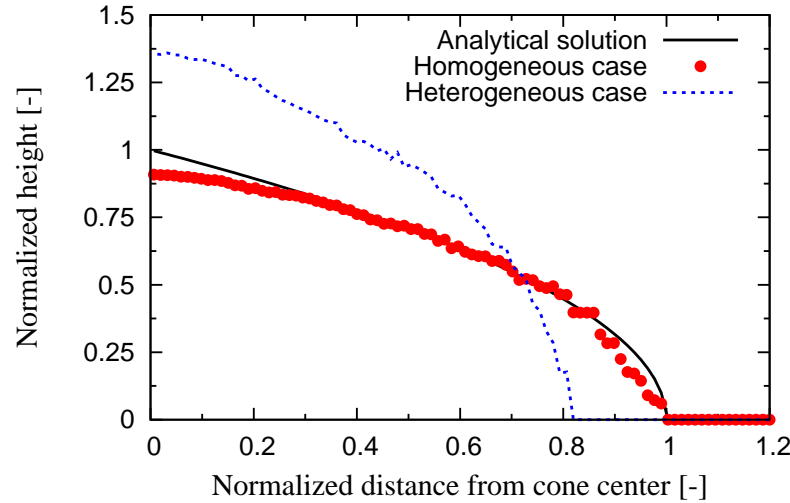
Figure 2.7: *Comparison of the final shapes of the spread material in the slump test.*

Heterogeneous case

A free surface flow of a suspension of rigid inclusions in a homogeneous non-Newtonian fluid was studied also by means of a slump test. Randomly placed rigid mono-sized spheres as well as rigid fibres were included into the study. Volume fraction, length, aspect ratio and density of the fibres was set to 0.2 %, 15, 80 and 3.14, respectively. Volume fraction, diameter and density of the spheres was set to 25 %, 2.5 and 1.04. In total, 2626 spheres and 415 fibres was generated. All other parameters were identical to Section 2.3.1.

Figure 2.8 shows the inclusions suspended in the matrix in the initial state, after 0.16 s and 14.5 s of flowing, whereas Figure 2.7 indicates the final shape of the heterogeneous case simulation (blue dotted curve). The heterogeneous case resulted in a smaller spread and higher height of the material suggesting an increased effective yield stress of the suspension.

All the case studies were run in parallel on 9 cores spatially dividing the computational domain into 3×3 sub-domains. The simulation of the heterogeneous case took ca. 1 week of the computation and ca. 80 000 of the numerical time steps. Approximately 55 % of the computational time was spent on the level of fluid - inclusions interaction whereas ca. 25 % was

<div align="center">
0 s   0.16 s   14.5 s
</div>
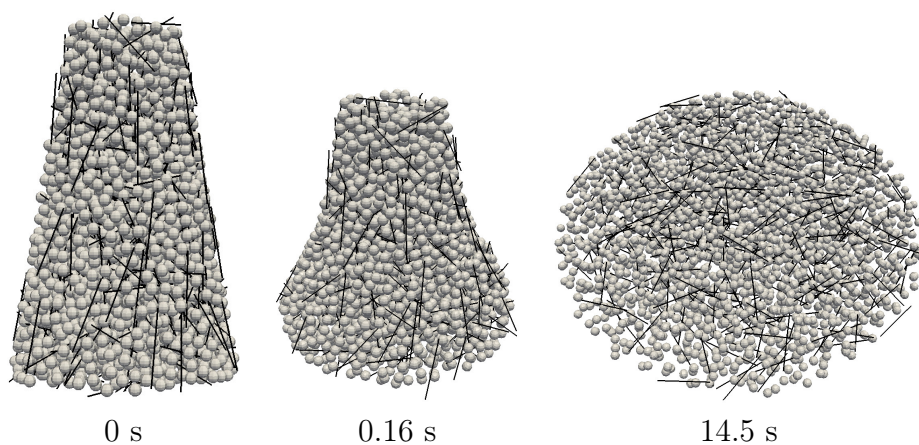
Figure 2.8: *3D view of the slump test in 3 different time steps.*

spent on the level of fluid and only 5 % of the computational time was spent on the level of inclusions. Approximately 15 % of the computational time was spent on other tasks such as inter-domain communication.

2.3.2   Study of the effective viscosity of the suspension

In this study, the effect of spherical rigid inclusions immersed in a Newtonian fluid on the effective viscosity of the suspension was of a primary interest. We investigated suspensions below the percolation limit preventing creation of a percolated network of direct contacts. Couette flow was used in the study (see Figure 2.9 for the geometry of the problem) where the 3D computational domain was bounded by periodic boundaries in two horizontal directions. In the vertical direction, the computational domain was bounded by two rigid walls moving with a prescribed velocity.
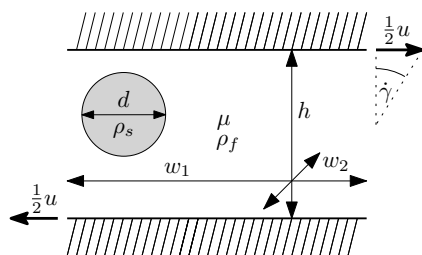
Figure 2.9: *Couette geometry used to investigate the effective viscosity of suspensions.*

The numerical values of individual parameters entering the simulation

were based on our experience obtained from brief parametric convergence studies, such as varying the diameter of sphere, varying the domain dimensions or varying the total shear of the problem. The resulting numerical values are presented in the following.

Rigid inclusions were of a spherical shape of a diameter equal to 8 lattice units, $d = 8$ and were discretized by uniformly spaced Lagrangian nodes of spacing $\delta = 1$ giving 296 Lagrangian nodes per sphere. The density of the inclusions was set to $\rho_s = 1.2\rho_f$. Dimensions of the computational domain were set to $h \times w_1 \times w_2 = 8d \times 4d \times 4d$ whereas the prescribed velocity of the walls was set to $u = 0.008$. The viscosity of the fluid was set to 0.175 lattice units. The coefficient of restitution of all collisions was set to $\varepsilon = 0$, i.e. all the collisions were assumed to be plastic. Coulomb friction was used to model friction among the spheres and to model friction of the spheres with the walls. The friction coefficient was set to $\mu_C = 0.6$. The resulting law of friction read

$$f(j_n, j_{t,max}) = j_{t,max} \min\left\{\frac{\mu_C|j_n|}{|j_{t,max}|}; 1\right\}. \tag{2.34}$$

A correction of lubrication forces was included in the numerical study. As proposed by several authors (Nguyen and Ladd, 2002; Kromkamp et al., 2006), the LBM accurately simulates the flow of the fluid between two inclusions when the distance of the two inclusions is greater than 1.1 lattice units. The lubrication force becomes underestimated for closer distances. Following Nguyen and Ladd (2002), the normal component of the lubrication force correction for spheres reads

$$\mathbf{F}_p^{int}(t) = -\mathbf{F}_q^{int}(t) = -6\nu\pi \left(\mathbf{u}_p(t) - \mathbf{u}_q(t)\right) \cdot \mathbf{n}_{p,q}\frac{r_p^2 r_q^2}{(r_p + r_q)^2}\left(\frac{1}{h} - \frac{1}{h_{lub}}\right),$$
$$\tag{2.35}$$

where $\mathbf{n}_{p,q}$ is the unit normal vector pointing from sphere p to sphere q. The radii of spheres are denoted as r_p and r_q and h is the distance between the two spheres.

At the beginning, both the fluid and the randomly distributed inclusions were at rest. During the initial part of the simulation, the fluid and the inclusions accelerated. This was accompanied by a decrease of the stress on the walls.

The main outcome of this study was the effective dynamic viscosity of the suspension, μ, which was computed by $\mu = \xi/\dot{\gamma}$, where ξ stands for an average shear stress and $\dot{\gamma}$ represents an average shear rate. Both the shear stress and the shear rate varies in the case of suspensions in space and time.

The spatially averaged shear stress was computed by $\xi(t) = \frac{F_t(t)}{A}$ where $F_t(t)$ is the tangential component of the force acting on the walls and A

stands for the area of the walls. The local shear rates were computed from the local second invariants of the shear rate tensors (see Eq. (2.7)). The spatially averaged shear rates were computed from a domain excluding regions close to the boundaries ($\circ < d/2$) as the composition of the suspension changes significantly in these regions.

The time averaging of the spatially averaged shear stresses and shear rates was also conducted. The time averaging started at the moment when the relative stress difference on the walls in two successive time steps was smaller than 10^{-5}. At the same moment, measurement of the shear of the fluid, $\gamma = \frac{u\delta t}{h}$ was initiated where δt is a time duration from the initiation of the simulation. The simulation terminated when the shear $\gamma = 2$ was reached.

Figure 2.10 presents results of the simulation, i.e. the relative effective viscosity, ν_{eff}^{rel}, of the suspension as a function of the volume fraction of inclusions, ϕ. The simulation was compared to Krieger-Dougherty (Krieger, 1959) estimation known to approximate experimental results reasonably well.

$$\nu_{eff}^{rel} = \left(1 - \frac{\phi}{\phi_m}\right)^{-2.5\phi_m} \tag{2.36}$$

with maximal volume fraction $\phi_m = 0.6$ for large volume fractions and to Batchelors's (Batchelor and Green, 2006) relationship for small volume fractions reading

$$\nu_{eff}^{rel} = 1 + 2.5\phi + 5\phi^2. \tag{2.37}$$

The obtained results match very well the theoretical predictions, proving that the fluid-inclusions interactions and mutual interactions among inclusions were properly implemented.
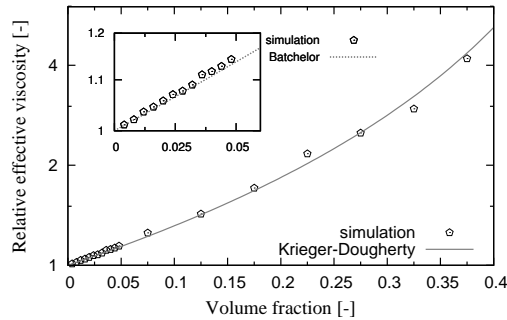
Figure 2.10: *Effective viscosity of suspension.*

2.4 Conclusions

We developed and implemented a numerical framework capable of simulating the flow of suspensions of rigid inclusions in a non-Newtonian fluid. The framework is based on a combination of the lattice Boltzmann method used for fluid dynamics, on the mass tracking algorithm for free surface representation and on the immersed boundary method for two-way coupled fluid-inclusions interactions. We further implemented a method for accurately representing the dynamics of inclusions by means of Runge-Kutta Fehlberg numerical time integration scheme and quaternion representation of rotations. The framework includes direct interactions, such as collisions, as well as continuous force interactions among inclusions.

We tried to carefully balance the way the individual phenomena were modelled with respect to both accuracy and the efficiency of the framework. As a result, the developed framework is capable of accurately simulating the flow of suspensions on the level of the largest inclusions and, at the same time, the framework is very efficient, allowing simulation of real-sized laboratory experiments with realistic amounts of inclusions within a reasonable time. Moreover, the framework does not require any fitting constants or parameters devoid of a clear physical meaning. In spite of this, the framework is stable, robust and easily extendible to a variety of problems in many fields.

The accuracy and effectiveness of the framework were shown on an example of a slump test. For the case of a homogeneous Bingham plastic, the analytical final shape of the fluid was matched favourably proving an accurate implementation of the Bingham rheology and of the free surface. The slump test of the suspension demonstrated the effect of rigid inclusions on the effective yield stress. The accuracy of the framework was further demonstrated on an example investigating the role of rigid inclusions on effective rheological properties of suspensions. The well established empirical relationship between the volume fraction of rigid spheres and effective viscosity of suspension was numerically recovered.

Within the field of self compacting concrete, the framework provides a useful tool for the design of material, as it makes possible a realistic simulation of the form-filling process. Moreover, the framework can be used to approach the material in a more general way and to investigate and understand the underlying processes of the form filling process such as e.g. segregation of aggregates in a suspension, blocking of aggregates behind reinforcement, the role of fibre-aggregate interactions on fibre orientation and distribution etc.

2.5   Acknowledgments

Chapter 3

Journal paper 2

Title:	Numerical simulation of the free surface flow of rigid fibres immersed in the non-Newtonian fluid
Authors:	Oldřich Švec, Jan Skoček
Submitted to:	Journal of Non-Newtonian Fluid Mechanics

Abstract

The ability of the Immersed boundary method to properly simulate immersed rigid particles of high aspect ratio, i.e. fibres, is presented. The Immersed boundary method is a part of the previously developed numerical framework capable of predicting the free surface flow of a suspension of rigid particles in a non-Newtonian Bingham plastic fluid. The framework is a combination of the Lattice Boltzmann method for fluid flow, the Immersed boundary method for two-way coupled interactions between fluid and rigid particles and an algorithm for the dynamics and mutual interactions of rigid particles. It is shown that the accuracy of the Immersed boundary method diverges for sub-grid diameters of fibres. An empirically obtained correction function is proposed to improve the accuracy of fibres of sub-grid diameter. The proposed correction function is then verified by means of two distinct examples. The proposed correction function allows for numerical simulations of hundreds of thousands of immersed rigid fibres within a reasonable computational time yet with a satisfactory accuracy.

3.1 Introduction

The free surface flow of suspensions plays an important role in many industrial and natural processes such as casting of concrete, mould filling, mud slides etc. An accurate description of the flow, often in complex geometries, is therefore required. We developed and described a numerical framework capable of simulating a free surface flow of a suspension of rigid inclusions in a non-Newtonian Bingham plastic fluid (Švec et al., 2012b).

In the developed framework, we combined the Lattice Boltzmann method used for simulating the flow of the non-Newtonian Bingham plastic fluid, a mass tracking algorithm representing the free surface, the Immersed boundary method (sometimes called External boundary force method (Wu and Aidun, 2009; Salahuddin et al., 2011)) used to simulate the two-way coupled interaction between fluid and inclusions and an algorithm for the dynamics and mutual interactions of inclusions. The framework is robust and efficient due to the adoption of the Immersed boundary method which makes it possible to accurately represent the two-way coupled interaction between fluid and small immersed inclusions of the size only a few lattice units. The lattice unit is a unit of the spatial discretization of the fluid domain.

Inclusions of high aspect ratio[1] such as elongated cylinders or fibres are often used in industrial applications of suspensions. Numerical simulation of flow of such systems poses significant computational demands. Take a cylindrical inclusion of a moderate aspect ratio of 50 as an example. A fine discretization of the fluid domain is necessary to achieve a reasonable accuracy of the two-way coupled interaction modelled by the Immersed boundary method. Namely, the fluid domain must be discretized in such a way that the discrete diameter of the cylinder is in the range of several lattice units. The fine discretization of the diameter of the cylinder shifts the discretized length of the cylinder to the range of hundreds lattice units which makes simulations of representative volumes of such suspension extremely time consuming if not impossible.

Several fundamentally different approaches exist on how to efficiently numerically simulate a large number the immersed rigid inclusions of high aspect ratio (fibres). One way is to replace the explicit representation of each individual fibre by a statistical representation of the fibres, i.e. by a second or higher order orientation tensors (Dupret and Verleye, 1999; Phelps and Tucker, 2009; Montgomery-Smith et al., 2010). Differential equations of time of the orientation tensors are then numerically solved. Hundreds or

---

[1]The aspect ratio is the ratio of the long dimension of an inclusion to its short dimension, such as length of the fibre to the diameter of the fibre.

thousands of the immersed fibres can be replaced by a single orientation tensor making the numerical simulation highly efficient. The trade-off is, among others, a significant loss of accuracy and poor representation of accompanying phenomena at the scale of fibres such as collisions among the fibres. Another approach is to explicitly represent individual fibres, their evolution and interaction with the surrounding environment (Wu and Aidun, 2010). The main drawback of that approach is the significantly increased computational costs.

In this paper, we focus our attention on numerical simulations of flow of suspensions of explicitly represented rigid fibres in Newtonian and non-Newtonian Bingham plastic fluid. We further focus on the accuracy of the Immersed boundary method for the case of fibres of sub-grid diameters and propose an empirical function correcting the Immersed boundary method.

Our aim is to numerically simulate a large number of fibres within a reasonable computational time. This brings a necessity to employ a coarse discretization of time and the fluid domain and consequently to employ fibres of a diameter below one lattice unit. The sub-grid size of the diameter of the immersed fibres brings several sources of error. Lattice Boltzmann method, as the fluid dynamics solver, is said to be between first up to second order accurate in space depending on many factors such as boundary condition implementation (Chen and Doolen, 1998). Similarly, the accuracy of the Immersed boundary method ranges from first up to second order depending on the implementation (Griffith and Peskin, 2005). Dynamics of the solid immersed inclusions is solved by means of the fourth order accurate Runge-Kutta Fehlberg numerical iteration scheme. All these are expectable losses in accuracy when employing coarse discretization of space and time.

After a brief introduction to the overall numerical framework in Section 3.2, Section 3.3 introduces the reader into the problem of numerical simulations of rigid fibres having sub-grid sized diameters. Section 3.3.1 investigates the effect of the diameter of fibres on the accuracy of the two-way coupled interaction modelled by the Immersed boundary method in a simple two dimensional flow. In Section 3.3.2, we propose an empirical function correcting the drag forces acting on the immersed fibres of sub-grid diameter. We further validate the proposed correction function by a distinct example in Section 3.3.3. The correction function is finally applied in Section 3.3.4 on a practical example of a slump test of fibre reinforced self-compacting concrete to highlight the importance of the usage of the correction function. Section 3.4 summarizes the main conclusions of the presented work.

3.2   Overview of the numerical framework

We have developed and implemented a numerical framework capable of predicting the free surface flow of a suspension of rigid particles in a non-Newtonian Bingham plastic fluid. In this section, we briefly summarize parts of the framework that are relevant to the discussed topic. The reader is referred to Švec et al. (2012b) for the full description of the framework.

To simplify the description of the complex problem, we divided the overall numerical framework into the three main levels illustrated in Figure 3.1:

a) **Level of fluid:** Free surface flow of a non-Newtonian Bingham plastic fluid is solved at this level. The Lattice Boltzmann method is used as the fluid dynamics solver whereas the mass tracking algorithm describes the free surface of the flow. The current state of the fluid (velocity and pressure field) is sent to the *level of fluid - inclusions interaction* where an external force field is calculated and sent back to the *level of fluid.* The *level of fluid* is briefly described in Section 3.2.1 whereas the free surface algorithm, the implementation of non-Newtonian Bingham plastic fluid and other details are described in Švec et al. (2012b).

b) **Level of inclusions:** Dynamics of inclusions of exact analytical shapes is calculated by solving Newton's equations of motion. Interactions among the inclusions and between the inclusions and the boundaries (such as walls etc.) are also solved. The current state of the inclusion (position, orientation etc.) is sent to the *level of fluid - inclusions interaction* where external interaction forces are calculated and sent back to the *level of inclusions.* The *level of inclusions* is fully described in Švec et al. (2012b).

c) **Level of fluid - inclusions interaction:** This intermediate level provides a two-way communication channel between the *level of fluid* and the *level of inclusions.* We have used the Immersed boundary method with direct forcing to accommodate the communication between the two levels Feng and Michaelides (2005). Thus, the communication is realized via force interactions. No-slip boundary condition between the fluid and the inclusions is assumed. To satisfy this condition, an interaction force field is created based on the current state of fluid and the current state of inclusions and sent back to the *level of fluid* and the *level of inclusions.* The *level of fluid - inclusions interaction* is introduced in Section 3.2.2 and fully described in (Švec et al., 2012b).
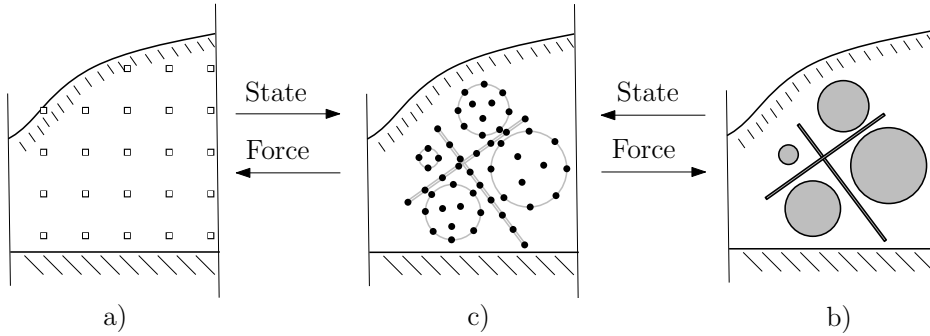
Figure 3.1: *Layout of the framework. a) Level of fluid, b) Level of inclusions, c) Level of fluid - inclusions interaction.*

3.2.1   Level of fluid: Lattice Boltzmann method

The Lattice Boltzmann method is based on Boltzmann equations and thus on the theory of ideal gases. Contrary to macroscopic fluid dynamics solvers such as the Finite element method, the Lattice Boltzmann method does not primarily work with macroscopic quantities but rather with mesoscopic particle distribution functions. These can be seen as clouds of microscopic particles, e.g. molecules, chaotically moving in space. Space is commonly discretized into square (2D domain) or cubic Eulerian cells forming a fixed Cartesian grid (see Figure 3.2a). Eulerian nodes, $\mathbf{x}^E \in \Omega^E$, are placed into the centre of each cell and a lattice is formed by connecting the nearest Eulerian nodes. The movement of the clouds of the microscopic particles is restricted onto the lattice directions, α, which leads into a discretization of continuous particle distribution functions into only a few particle distributions, $f_\alpha \left(\mathbf{x}^E, t \right)$, associated with lattice velocities, $\mathbf{c}_\alpha$. See Figure 3.2b) for a 2D example. There are several lattice types, differentiated on by the shape of the lattice. The $D2Q9$ and $D3Q15$, where D and Q stand for the dimension of the problem and the number of lattice velocities, are two of the most common types adopted.

The vertical and horizontal spacing of the nodes, the reference density of the fluid, $\rho_{f,0}$, and the length of the time step are usually set to unity for the most simple and common lattice types and the simulated problem is scaled accordingly. All the numerical simulations presented in this paper follow this assumption. The provided description of the Lattice Boltzmann method is general and independent of the lattice used, provided that the reference fluid density, time step and spacing of the nodes are normalized to unity as described above. All the equations presented in this section can be found e.g. in Latt (2007), if not stated otherwise.
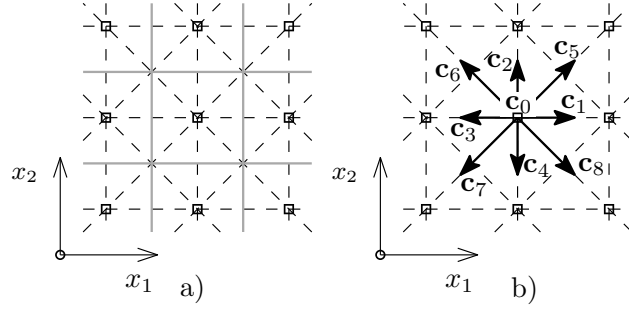
Figure 3.2: *a) Schematic representation of the D2Q9 lattice. Square marks stand for nodes, grey lines for cell boundaries and dashed lines for the lattice. b) Set of corresponding lattice velocity vectors, $\mathbf{c}_\alpha$, in a node.*

An evolution of the particle distributions in space and time is expressed by the Lattice Boltzmann equation

$$\underbrace{f_\alpha \left(\mathbf{x}^E + \mathbf{c}_\alpha, t+1\right) = f_\alpha \left(\mathbf{x}^E, t\right)}_{\text{streaming}} + \underbrace{f_\alpha^{Ext}(\mathbf{x}^E, t)}_{\text{forcing}} + \underbrace{\Omega_\alpha \left(\mathbf{x}^E, t\right)}_{\text{collision}} . \qquad (3.1)$$

The equation consists of the streaming part, the forcing term and the collision part. The streaming part represents propagation of particle distributions from one node to another along the lattice links. The lattice velocities are chosen in such a way that a particle distribution streams from one node to another node during the unit time step. The forcing term accounts for the effect of an external force in the following way (Mohamad and Kuzmin, 2010; He et al., 1997; Guo et al., 2002)

$$f_\alpha^{Ext} \left(\mathbf{x}^E, t\right) = 3w_\alpha \mathbf{c}_\alpha.(\mathbf{F}^{fluid} \left(\mathbf{x}^E, t\right) + \mathbf{F}^{ext} \left(\mathbf{x}^E, t\right)), \qquad (3.2)$$

where w_α stands for weights defined by the type of the lattice. $\mathbf{F}^{fluid} \left(\mathbf{x}^E, t\right)$ is a force coming from the *level of fluid - inclusions interaction* as described in Eq. (3.10). $\mathbf{F}^{ext} \left(\mathbf{x}^E, t\right)$ represents any other external force such as gravity.

The collision part mimics real collisions of the microscopic particles. The collisions are difficult to express explicitly and, therefore, an approximation of the collisions in the form of collision operator, $\Omega_\alpha \left(\mathbf{x}^E, t\right)$, was introduced into the Lattice Boltzmann method. We used one of the simplest collision operators, the so-called BGK operator, see e.g. Chen and Doolen (1998). The BGK operator linearly deforms the actual particle distributions towards an equilibrium state.

The local macroscopic quantities of the fluid such as densities and velocities are computed as the first two moments of the particle distributions.

Further information on the *level of fluid* including the non-Newtonian Bingham plastic fluid representation, free surface description and others can be found in Švec et al. (2012b).

3.2.2 Level of fluid - inclusions interaction: Immersed boundary method

The Immersed boundary method with direct forcing (Feng and Michaelides, 2005, 2009; Shu et al., 2007; Uhlmann, 2005; Wu and Shu, 2009, 2010) creates an interface between the *level of fluid* and the *level of inclusions*, i.e. a description of the way the two levels communicate with each other. This communication is realized via interaction force fields used to mimic the no-slip boundary conditions.

In the Immersed boundary method, solid particles, p, are discretized by a set of Lagrangian nodes, n, which are independent of the discretization of the fluid, as shown in Figure 3.3a) and Figure 3.1c). Position of the Lagrangian nodes is denoted $\mathbf{x}_{p,n}^L(t)$. The force field is computed at these Lagrangian nodes. Velocity of the inclusions and velocity of the fluid should be equal in these nodes when assuming no-slip contact between the inclusions and the fluid. Nevertheless, differences in the velocities occur as the system evolves in discrete time steps. An interaction force is calculated from these differences and applied back both to the *level of fluid* and the *level of inclusions*.

The interaction forces between inclusions and fluid are computed in the following way. The velocity of the fluid and the velocity of the inclusions are computed in each Lagrangian node. The velocity of the inclusions in the Lagrangian nodes is computed as

$$\mathbf{u}_{p,n}(t) = \mathbf{u}_p(t) + \boldsymbol{\omega}_p(t) \times (\mathbf{x}_{p,n}^L(t) - \mathbf{x}_p(t)), \qquad (3.3)$$

where $\mathbf{x}_p(t)$, $\mathbf{u}_p(t)$ and $\boldsymbol{\omega}_p(t)$ denote position and linear and angular velocity of the centre of gravity of the inclusion. The velocity of the fluid at the Lagrangian nodes, $\mathbf{u}_f\left(\mathbf{x}_{p,n}^L(t), t\right)$, must be interpolated from the Lattice Boltzmann nodes, $\mathbf{x}^E \in \Omega^E$, since the two types of nodes do not coincide. The interpolation is performed using a Dirac delta function as

$$\mathbf{u}_f\left(\mathbf{x}_{p,n}^L(t), t\right) = \int_\Omega \mathbf{u}_f(\mathbf{x}, t) D(\mathbf{x} - \mathbf{x}_{p,n}^L(t)) \, \mathrm{d}\mathbf{x} \qquad (3.4)$$

$$\approx \frac{\sum^{\mathbf{x}^E} \mathbf{u}_f(\mathbf{x}^E, t) D(\mathbf{x}^E - \mathbf{x}_{p,n}^L(t))}{\sum^{\mathbf{x}^E} D(\mathbf{x}^E - \mathbf{x}_{p,n}^L(t))}, \qquad (3.5)$$

where $D(\mathbf{x}^E - \mathbf{x}_{p,n}^L(t)) = D(\circ) = d(\circ_1)d(\circ_2)d(\circ_3)$ is the Dirac delta function. There exist several different Dirac delta functions (Yang et al., 2009) with

various shapes and smoothing lengths. We adopted the following cosine Dirac delta function

$$d(\circ_i) = \begin{cases} 1 + \cos\left(\frac{\pi}{2}|\circ_i|\right) & \text{if} \quad |\circ_i| < 2 \\ 0 & \text{otherwise.} \end{cases} \tag{3.6}$$

The interaction force in the Lagrangian nodes is constructed on the basis of the difference between the velocity of the fluid and the velocity of the inclusion at these nodes. The simplest form of the force reads

$$\mathbf{F}_{p,n}^{fluid}(t) = \frac{\rho_{f,0}}{\Delta t}\left[\mathbf{u}_f\left(\mathbf{x}_{p,n}^L(t), t\right) - \mathbf{u}_{p,n}(t)\right]\Delta V_{p,n}, \tag{3.7}$$

where $\Delta V_{p,n}$ is a volume associated with the n-th Lagrangian node (see Figure 3.3b). The reference density of the fluid, $\rho_{f,0}$, and the Lattice Boltzmann time step, Δt, are set to unity, see Section 3.2.1.

The total interaction force and the torque between the inclusion and the fluid exerted on the $p - th$ inclusion are expressed as

$$\mathbf{F}_p^{fluid}(t) = \sum^n \mathbf{F}_{p,n}^{fluid}(t) \tag{3.8}$$

$$\mathbf{T}_p^{fluid}(t) = \sum^n \left[\left(\mathbf{x}_{p,n}^L(t) - \mathbf{x}_p(t)\right) \times \mathbf{F}_{p,n}^{fluid}(t)\right] \tag{3.9}$$

Eqs. (3.8) and (3.9) form an output which is sent back to the *level of inclusions* to the Newton's equations of motion.

The total interaction force field between the inclusions and the fluid exerted on the Lattice Boltzmann nodes is obtained by an extrapolation of the forces from the Lagrangian nodes to the Lattice Boltzmann nodes, similarly to Eqs. (3.4) and (3.5). The extrapolation is performed by means of the same Dirac delta function as

$$\mathbf{F}^{fluid}(\mathbf{x}^E, t) = -\sum^p \frac{\sum^n\left[\mathbf{F}_{p,n}^{fluid}(t) D(\mathbf{x}^E - \mathbf{x}_{p,n}^L(t))\right]}{\sum^n D(\mathbf{x}^E - \mathbf{x}_{p,n}^L(t))} \tag{3.10}$$

Eq. (3.10) forms an output that is sent back to the *level of fluid* to Eq. (3.2).

We refer the reader to Švec et al. (2012b) for the full description of the numerical framework.

3.3 Study of the level of fluid - inclusions interaction

The need to numerically simulate large number of immersed fibres together with limited computational resources brings the necessity to employ fibres of
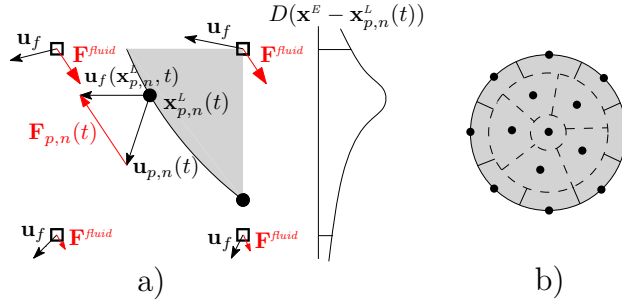
Figure 3.3: *a) Schematic representation of the Immersed boundary method at a single Lagrangian node. Black and red quantities are inputs and outputs of the method. b) Scheme of the uniform discretization of a circle by Lagrangian nodes (black dots) and corresponding volumes $\Delta V_{p,n}$.*

diameter below one lattice unit. The following sections will therefore study the accuracy of the level of fluid - inclusions interaction for immersed fibres of sub-grid diameters. A function correcting drag forces acting on the immersed fibres will be introduced and validated.

3.3.1   Accuracy of the level of fluid - inclusions interaction

In this section, we analyse the accuracy of drag forces exerted on inclusions immersed in an incompressible Newtonian fluid. The correct drag force serves as the main indicator of the accuracy of the level of fluid - inclusions interaction. Similarly to Ben Richou et al. (2004), we investigated a numerical simulation of a Poiseuille flow of a Newtonian fluid. A rigid cylindrical obstacle was immersed in the Poiseuille flow and the drag force acting on the obstacle was computed. The computed drag force was then compared with an approximate solution developed by Faxén (1946).

We simulated an infinite circular cylinder of diameter d fixed in place midway between two parallel plates (see Figure 3.4). The two parallel plates positioned normal to the z axis were modelled as a no-slip boundary condition by means of a bounce-back scheme (Aidun and Lu, 1995). A periodic boundary condition (Sukop and Thorne, 2005) was applied in y direction. The flow was driven by a prescribed Poiseuille velocity profile (Latt and Chopard, 2008) at the left edge of the domain, i.e. at $x = 0$, and at the right edge of the domain, i.e. at $x = L_x$. The Poiseuille velocity profile had the
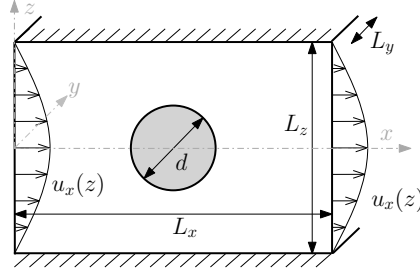
Figure 3.4: *Geometry of the Poiseuille flow with the infinite circular cylinder.*

following form (Ben Richou et al., 2004):

$$u_x(z) = u_{x,max} \left[1 - \left(\frac{z}{L_z/2} \right)^2 \right], \tag{3.11}$$

where $u_{x,max}$ is the prescribed maximum speed of the flow and L_z is the vertical dimension of the domain.

The initial velocity of the flow was set to zero. After initiation of the simulation, the flow accelerated until it reached a steady state. The steady-state was assumed when the relative change of the drag force acting on the circular cylinder in time dropped below 10^{-8}. The drag force acting on the infinite cylindrical obstacle, $F_{x,study}$, was computed by Eq. (3.8) when the numerical simulation reached the steady state. The numerically obtained drag force was then compared to an approximate solution (Ben Richou et al., 2004; Faxén, 1946):

$$F_{x,Faxen}(k) = \frac{4\pi}{f(k) + g(k)}, \tag{3.12}$$

where $k = d/L_z$ and

$$
\begin{aligned}
f(k) &= A_0 - (1 + 0.5k^2 + A_4k^4 + A_6k^6 + A_8k^8)ln(k), \\
g(k) &= B_2k^2 + B_4k^4 + B_6k^6 + B_8k^8
\end{aligned}
$$

with coefficients set to $A_0 = -0.9156892732$, $A_4 = 0.05464866$, $A_6 = -0.26462967$, $A_8 = 0.792986$ and $B_2 = 1.26653975$, $B_4 = -0.9180433$, $B_6 = 1.8771010$, $B_8 = -4.66549$. Notice that Eq. (3.12) is valid only for $k < 0.5$ and for very low Reynold's numbers, $Re \ll 1$ (Ben Richou et al., 2004).

A parametric study containing 1000 individual simulations was run to obtain the accuracy of the drag forces for a range of combinations of the

input parameters. We have chosen an artificial quantity labelled "time factor", $t_f = d^2/\nu$, to be the main variable quantity of the parametric study, where ν is the kinematic viscosity of the Newtonian fluid.

The following parameters of the parametric study were randomly generated obeying a uniform distribution and bounded by an interval: Time factor, $\{t_f \in \mathbb{R}|10^{-5} \leq t_f \leq 10^4\} = [10^{-5}, 10^4]$; Reynold's number of the problem, $Re = u_{x,max}d/\nu$ in $[10^{-5}, 10^{-3}]$; Kinematic viscosity of the fluid, ν in $[0.005, 0.2]$; Vertical dimension of the domain, L_z in $[L_{z,min}, 3L_{z,min}]$, where $L_{z,min} = max(20, 3d)$.

The remaining dimensions of the domain were set to $L_x = 3L_z$, $L_y = 1$. Density of the Newtonian fluid was set to $\rho_f = 1$. Diameter of the immersed cylindrical obstacle was computed as $d = \sqrt{t_f \nu}$ whereas the maximum speed of the flow was calculated as $u_{x,max} = Re\nu/d$. The selected intervals of the parameters assured that $u_{x,max} < 0.05$ and hence that the assumption of incompressibility was fulfilled.

Figure 3.5 presents individual results of the parametric study in the form of the relative drag force $F_{x,rel} = F_{x,study}/F_{x,Faxen}$ as a function of the diameter, d, of the immersed infinite cylinder. We split the plot into two parts by a vertical dashed line at $d = 1$. The right part of the plot exhibits an expectable error of the numerical simulation. The error moreover diminishes with the increasing diameter of the immersed cylinder, proving a correct numerical implementation. The left part of the plot on the other hand shows a significant decrease of the relative drag force, $F_{x,rel}$, i.e. a significant increase of the error of the numerical simulation.

Our primary aim was to study and correct the drag forces present in the left part of the plot. All the successive plots and parametric studies will therefore take into account immersed cylinders with diameter smaller than 1.
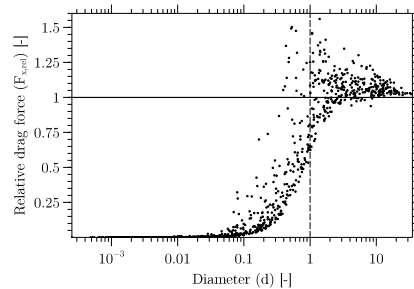
Figure 3.5*: Result of the parametric study in the form of the relative drag force as a function of the diameter of the immersed cylinder.*

Figure 3.6 presents the individual results of the parametric study in the form of the relative drag force, $F_{x,rel}$, as a function of the time factor, t_f. The plot is shown twice, both using a log-log scale (black circle marks) and using a log-linear scale (red cross marks). Contrary to Figure 3.5, the red log-linear plot in Figure 3.6 reveals a strong dependency of the error of the drag forces on the time factor, t_f. The black log-log plot shows that the relative drag forces significantly reduce their values following a linear trend of the slope close to 1 : 1. The linear trend suggests that the relative drag forces actually tend to zero as the time factor decreases making the relative error of the drag forces tend to infinity.
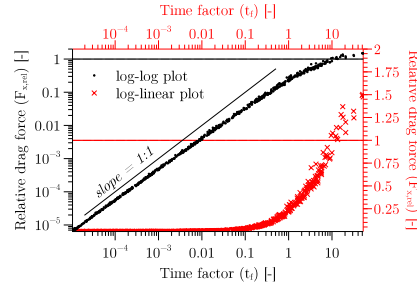
Figure 3.6: *Result of the parametric study in the form of the relative drag force as a function of the time factor.*

Figure 3.5 highlights that in the case of immersed rigid cylinders the numerical model, as described in Section 3.2 and in Švec et al. (2012b), is valid only when the diameter of the immersed cylinders remains above $d \gtrsim 1$. To be able to use the level of fluid - inclusions interactions for immersed cylinders of diameter $d \lesssim 1$, while maintaining an acceptable accuracy, the drag forces must be corrected.

3.3.2 Correction of the level of fluid - inclusions interaction

As presented in Section 3.3.1, the level of fluid - inclusions interaction is capable of relatively accurately simulating only immersed cylinders of diameter, $d \gtrsim 1$ lattice units. This section therefore aims to correct the level of fluid - inclusions interaction to allow for coarsely discretized fibres of subgrid diameter with an acceptable accuracy.

Figure 3.5 points that the level of fluid - inclusions interaction fails to properly compute the drag forces when the diameter of fibres falls below $d \lesssim 1$. Figure 3.6 further reveals that the error of the drag forces is mainly

dependent on the time factor, t_f. We therefore propose to extend Eq. (3.7) by a correcting value C:

$$\mathbf{F}_{p,n}^{fluid}(t) = C\frac{\rho_{f,0}}{\Delta t}\left[\mathbf{u}_f\left(\mathbf{x}_{p,n}^L(t), t\right) - \mathbf{u}_{p,n}(t)\right]\Delta V_{p,n}. \tag{3.13}$$

A parametric study as presented in Section 3.3.1 was run once again, this time including the modified Eq. (3.13). Each individual numerical simulation of the parametric study was run several times for different values of C. The primary goal was to find a value of C which would make the computed drag forces equal to Eq. (3.12) within an error of 5 %. We employed classical Newton-Raphson method to find the optimal value of C.
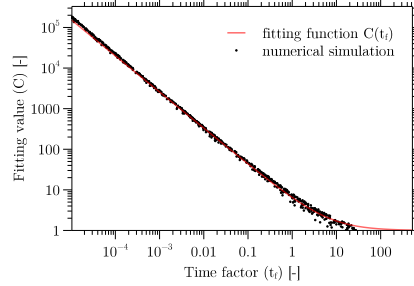
Figure 3.7: *The resulting correcting values for all the numerical simulations of the parametric study.*

Figure 3.7 presents the resulting values of C as a function of the time factor, t_f. Similarly to Figure 3.6, the result shows a strong correlation of the values, C, with the time factor, t_f. Based on the resulting correcting values, we have constructed the following curve fitting function (see red line in Figure 3.7)

$$C(t_f) = \frac{5.5}{t_f^{0.89}} + 1. \tag{3.14}$$

The performance of the correction function, $C(t_f)$, was verified by means of the very same parametric study, as presented in Section 3.3.1. This time, Eq. (3.13) together with Eq. (3.14) were employed. Figure 3.8 presents the relative drag force as a function of the time factor, t_f, both for the uncorrected state (red cross marks) and for the corrected state (black circle marks). Notice that the relative error remains below approx. 20% for all numerical simulations in the parametric study when the correction function, $C(t_f)$, is used whereas the relative error tends to infinity if no correction is employed.

In this section, we proposed a simple empirical function to correct the drag forces acting on the immersed cylinders. We managed to convert an
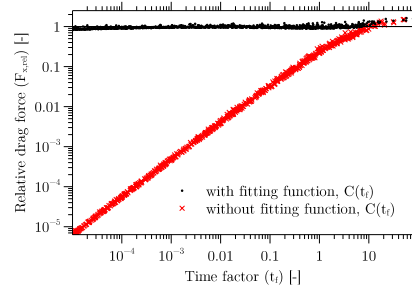
Figure 3.8*: Comparison of the relative drag force for both corrected (black circle marks) and uncorrected state (red cross marks).*

error that tended to infinity to a maximum error of 20% for the investigated cases. The next section will further validate the correction function on a more complex problem.

3.3.3 Verification of the correction function

The correction function, Eq. (3.14), was proposed in Section 3.3.2 to correct the drag forces acting on immersed cylinders of low time factor, t_f. The correction function was calibrated by a simple example containing a single infinite stationary cylinder immersed in an incompressible Newtonian fluid. Many industrial processes, such as casting of fibre reinforced self-compacting concrete, involve non-Newtonian fluids. This section therefore presents the ability of the corrected model to properly predict the effective viscosity of rigid fibres immersed in the non-Newtonian fluid undergoing a Couette flow. The main goal of the study is to compare the numerically obtained effective viscosity of the fibre suspension with an analytical solution by Ghanbari and Karihaloo (2009).

We simulated a set of rigid fibres immersed in a non-Newtonian Bingham plastic fluid undergoing a Couette flow (see Figure 3.9). Couette flow is a laminar flow of a viscous fluid bounded between two parallel plates where the two parallel plates move in the mutually opposite directions. The two parallel plates, positioned normal to the z axis at $-0.5L_z$ and $0.5L_z$, were modelled as a no-slip boundary condition by means of the bounce-back scheme. The periodic boundary condition was applied in x and y direction. The Bingham plastic fluid was modelled as a bilinear fluid in the same manner as in Švec et al. (2012b). The density and plastic viscosity of the Bingham plastic fluid were set to 2300 kg/m^3 and $\nu_{pl} = 10$ Pa s, respectively. The length and density of the fibres was set to 6 cm and 7850 kg/m^3. All the real units
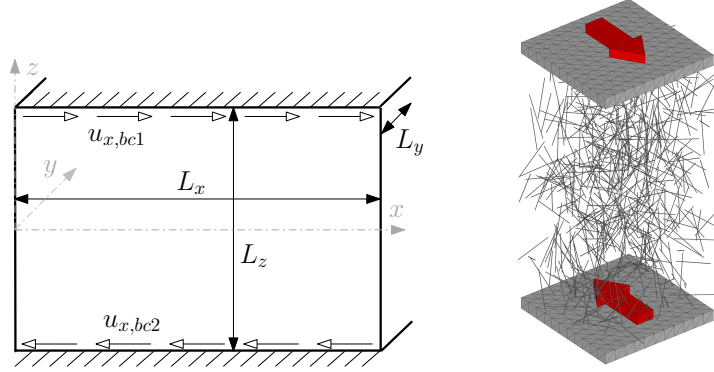
Figure 3.9: *2D and 3D Layout of the Couette flow.*

were appropriately rescaled to the Lattice Boltzmann units assuming their dimensionless equivalents defined in the next paragraph.

A parametric study containing 200 individual numerical simulations was run to verify the accuracy of the proposed correction term for all possible combinations of the input parameters. Two distinct simulations, $s1$ and $s2$, having the velocity of the parallel plates set to $u_{x,bc1} = -u_{x,bc2} = 0.03$ and 0.06 lattice units were run for each set of parameters in the parametric study.

The following parameters of the parametric study were randomly generated following a uniform distribution. Fibre volume fraction was randomly generated in the interval Φ in $[0\%, 0.5\%]$. The discretized length of the fibres, l_f, ranged between 3 lattice units and 12 lattice units whereas the fibre aspect ratio, l_d, ranged from 40 to 80. Finally, the yield stress of the Bingham plastic fluid was varied from 0 to 30 Pa. Dimensions of the domain read $L_x \times L_y \times L_z = 6l_f \times 3l_f \times 3l_f$.

The initial position and orientation of all the fibres were randomly generated following a uniform distribution leading to an approximately homogeneous and isotropic distribution of the fibres. The fibres were not allowed to change their initial orientation to maintain the isotropic state of the fibre orientation. Mutual collisions of the fibres were thus deactivated.

The analytical effective viscosity of the fibre suspension, $\nu_{eff,an}$, read (Phan-Thien and Karihaloo, 1994; Ghanbari and Karihaloo, 2009):

$$\nu_{eff,an} = \nu_{pl} \left(1 - \Phi + \frac{\pi \Phi l_d^2}{3ln(2l_d)} \right). \qquad (3.15)$$

The analytical equation is valid only for dilute isotropic suspensions of fibres of maximum fibre volume fraction, $\Phi_{max} = 2\%$ (Ghanbari and Karihaloo, 2009). The numerically obtained effective viscosity of the fibre suspension was computed as

$$\nu_{eff,sim} = \frac{\bar{\sigma}_{bc,x,s2} - \bar{\sigma}_{bc,x,s1}}{\bar{\dot{\gamma}}_{s2} - \bar{\dot{\gamma}}_{s1}}, \qquad (3.16)$$

where $\bar{\sigma}_{bc,x}$ is the average stress acting on the two parallel plates in x direction. The average stress was computed from the absolute value of x component of total force acting on the two parallel plates divided by their area. The value $\bar{\dot{\gamma}}$ is the spatially averaged second invariant of the shear rate tensor and read

$$\bar{\dot{\gamma}}(t) = \frac{1}{n} \sum_{n \in \Omega_s^E} \dot{\gamma}\left(\mathbf{x}_n^E, t\right), \qquad (3.17)$$

$$\dot{\gamma}\left(\mathbf{x}_n^E, t\right) = 2\sqrt{\dot{\gamma}_{ij}\left(\mathbf{x}_n^E, t\right) \dot{\gamma}_{ij}\left(\mathbf{x}_n^E, t\right)}, \qquad (3.18)$$

where $\dot{\gamma}_{ij}\left(\mathbf{x}_n^E, t\right)$ and $\dot{\gamma}\left(\mathbf{x}_n^E, t\right)$ are shear rate tensor and second invariant of the shear rate tensor of Eulerian node, n. Value Ω^E represents a set of all Eulerian nodes in the computational domain as described in Section 3.2.1. The spatial averaging of the shear rate tensor was conducted in the whole computational domain with an exception of regions close to the parallel plates at a distance smaller than the length of a fibre, l_f. The reduced spatial domain was denoted Ω_s^E.
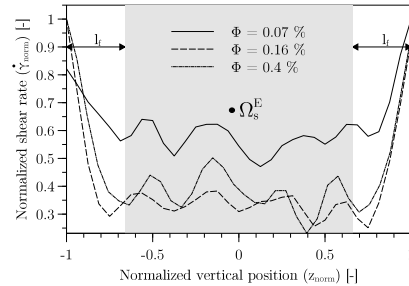
Figure 3.10: *Indication of the wall effect by means of the normalized shear rate.*

Figure 3.10 presents the normalized shear rate, $\dot{\gamma}_{norm}$, as a function of the normalized vertical position of the Eulerian nodes, $z_{norm} = z/L_z$. The normalized shear rate was computed as $\dot{\gamma}_{norm} = \dot{\gamma}\left(\mathbf{x}_p^E, t\right) / max\left(\dot{\gamma}\left(\mathbf{x}_p^E, t\right)\right)$. Notice that the regions at the vicinity of the two parallel plates have significantly larger shear rates. This observed wall effect is caused by the fewer number of fibres occurring in that region. To obtain the representative effective viscosities, the region in the vicinity of the two parallel plates must be neglected.

Before initiation of the numerical simulation, the initial velocity of the flow was set to zero. After initiation of the simulation, the flow accelerated until it reached a steady state. The steady-state was assumed to be reached when the spatially averaged second invariant of the shear rate tensor, $\bar{\dot{\gamma}}$, converged to its final value within a certain threshold. The error of the numerically obtained effective viscosity of the fibre suspension was then measured in terms of the relative effective viscosity, $\nu_{eff,rel} = \nu_{eff,sim}/\nu_{eff,an}$.
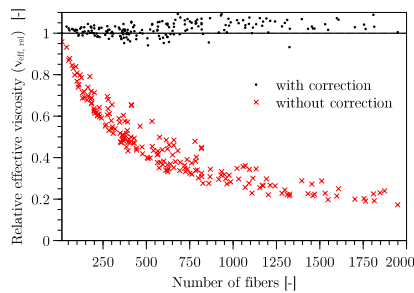
Figure 3.11: *Comparison of the relative effective viscosity both for the corrected and the uncorrected state.*

Figure 3.11 presents the relative effective viscosity of individual numerical simulations of the parametric study as a function of the number of fibres contained in the computational domain. The relative effective viscosity is presented both for the numerical simulations without the correction function (red cross marks) and for the numerical simulations having the correction function included (black circle marks).

The relative effective viscosity of the fibre suspension for the case of the uncorrected numerical simulations seems to diminish with an increasing number of fibres in the computational domain. This results in the error tending to infinity, similarly to Section 3.3.1. The proposed correction function effectively reduced the heavily increasing error to the range of $\pm 10\%$ for the investigated cases.

In this section, the accuracy of the proposed correction function was shown on a more complex example of fibre suspension in non-Newtonian Bingham plastic fluid. The next section will indicate the influence of the correct drag forces and consequently the importance of the proposed correction function on a practical example.

3.3.4   Applications - Slump test

Section 3.3.2 introduced an empirical function that corrected drag forces acting on the immersed cylinders. The correction function was also verified by a distinct example as presented in Section 3.3.3.

Orientation and distribution of fibres plays an important role of many industrial processes. The main aim of this section is therefore to show the impact of the correction function on the orientation and distribution of fibres on a practical example of a slump test. The slump test is a widely used method to measure workability and yield stress of homogeneous fluids or suspensions in industrial applications of concrete (Roussel and Coussot, 2005). The spreading nature of the slump test makes the fibres quickly orient normal to the flow directions. The slump test thus serves as a benchmark test for the location and orientation of fibres.

| 0 s | 0.13 s | 0.25 s |
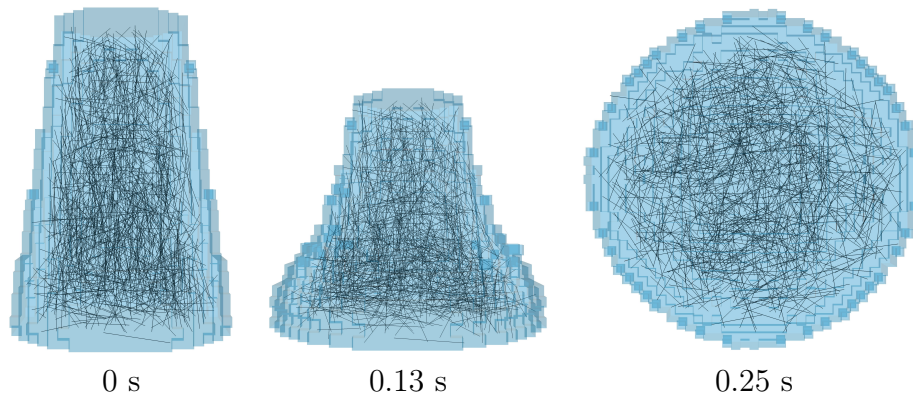
Figure 3.12*: 3D and top view of the slump flow at three different time steps.*

A free surface flow of a suspension of randomly placed rigid fibres in a incompressible homogeneous non-Newtonian Bingham plastic fluid was studied by means of the slump test (see Figure 3.12 left). A standard slump cone (see BS EN 12350-2) as well as homogeneous Bingham plastic fluid were assumed in the numerical simulation. The given problem was initially set up in real physical units and appropriately rescaled into Lattice Boltzmann units. For simplicity, we present the discretized Lattice Boltzmann units only.

The slump cone was discretized into *height × bottom diameter × top diameter* $= 30 \times 20 \times 10$ lattice units. Yield stress, plastic viscosity and density of the fluid were set to $5 \times 10^{-5}, 0.074$ and 1, respectively. The flow was driven by the gravity equal to 4.2×10^{-4}. Volume fraction, length, aspect ratio and density of the fibres was set to 0.5 %, $l_f = 6$, $l_d = 80$ and 3.05, respectively. In total, 1038 fibres were generated. The diameter of the

fibres was computed as $d = l_f/l_d = 6/80 = 0.075$ whereas the time factor was calculated as $t_f = d^2/\nu_{pl} = 0.075^2/0.074 = 0.076$. Both collisions and rotations of fibres were allowed. The correction function read

$$C(t_f) = \frac{5.5}{t_f{}^{0.89}} + 1 \approx 55.5 \ . \tag{3.19}$$

Two distinct numerical simulations were run. The drag forces acting on the rigid fibres were not corrected in the first numerical simulation, i.e. $C(t_f, \nu_{pl}) = 1$. In the second case, the drag forces were corrected, i.e. $C(t_f, \nu_{pl}) = 55.5$.

The numerical simulations started by an instantaneous release of the slump cone and terminated after 1000 discrete time steps corresponding to approx. 1 second. Figure 3.12 presents a 3D view of the slump flow of the uncorrected numerical simulation at its initial stage and after 0.13 seconds. A top view of the slump test is shown for the stage at 0.25 seconds after the initiation of the numerical simulation. The blue colour in Figure 3.12 represents the shape of the non-Newtonian Bingham plastic fluid and the black lines are the immersed rigid fibres. Figure 3.13 compares location and orientation of the rigid fibres for the two different numerical cases at the different time stages. The black lines represent the fibres of the corrected numerical simulation whereas the red lines stand for fibres of the uncorrected case. The fluid phase is hidden for clarity.

As seen in Figure 3.13 - left, the fibres were initially at identical positions and orientations both for the corrected and uncorrected state. As the time evolved, positional and orientation discrepancies occurred. The side view of the numerical simulation at 0.25 seconds shows that the red fibres of the uncorrected case settled significantly faster than the corresponding black fibres of the corrected case. The top view at 0.25 seconds further reveals that the majority of the fibres of the two numerical cases were positioned at mutually different locations and orientations.

The previous section presented validity of the proposed correction function. This section aimed to present differences in distribution and orientation of fibres for the numerical cases where the drag forces were either corrected or remained uncorrected. Without studying whether correct solutions were obtained, we observed not negligible discrepancies in mutual positions and orientations of fibres for the two studied cases, as presented in Figure 3.13 - right. This section therefore illustrates the importance of the proposed correction function.

0 s   0.13 s   0.25 s
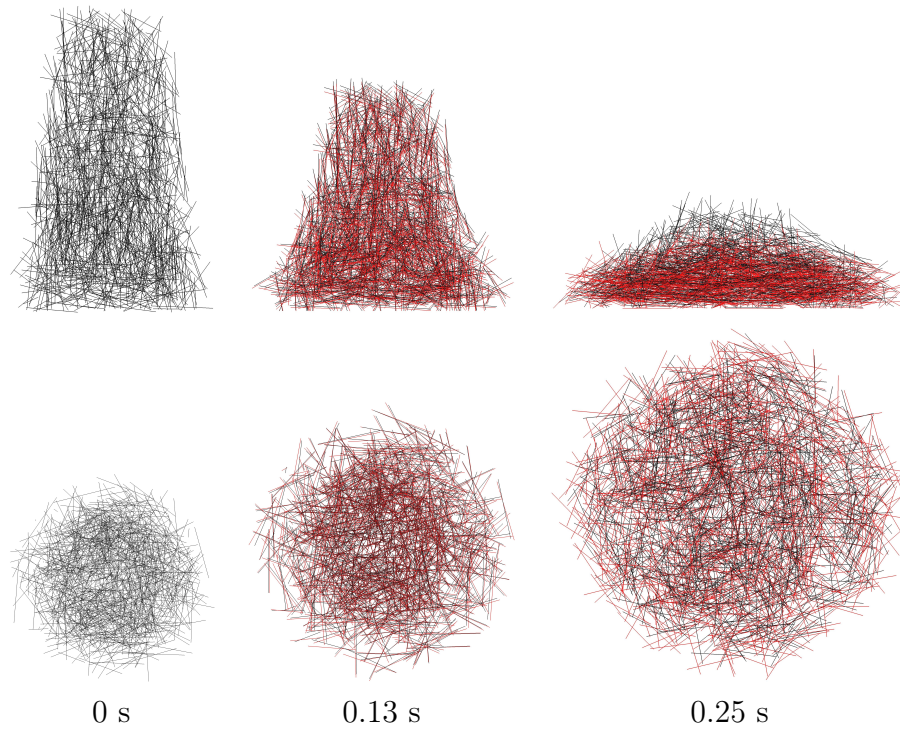
Figure 3.13: *Comparison of the orientation and distribution of fibres for both the corrected (black) and the uncorrected (red) state.*

3.3.5   Discussion

In this section we discuss limitations, advantages and disadvantages of the correction function approach.

The proposed correction function was validated only by means of the presented numerical simulations. We tested the proposed correction function only by Poiseuille and Couette creeping flows of dilute suspensions of thin rigid cylinders immersed in the Newtonian and Non-Newtonian Bingham plastic fluid. The validation was conducted with the primary aim to allow numerical simulations of steel fibres immersed in fibre reinforced self-compacting concrete flow. General limits of the proposed correction function are unknown and are not of a primary concern of the presented study.

The main motivation for the introduction of the correction function is the inability of the level of fluid - inclusions interaction to accurately represent fibres of sub-grid diameter. With the proposed correction function, the accuracy of the two-way interactions can be maintained at an acceptable level. The coarser discretization of the spatial domain on the other hand brings a reduced accuracy of the overall model even when the correction function is

employed. In all the practical numerical simulations that we did so far, we therefore did not go below the discrete length of fibres of 6 lattice units.

Due to the discrete nature of the fluid dynamics solver, lubrication forces among fibres are also inaccurate. Corrections of the lubrication forces were therefore proposed by e.g. Yamane et al. (1994). The lubrication forces become significant when two fibres get into close contact not exceeding the distance of approx. diameter of the fibre. In case of fibres of sub-grid diameter, the lubrication forces act only for an extremely short period of time. We therefore usually do not correct the lubrication forces by e.g. Yamane et al. (1994), but instead, we approximate the effect of the lubrication forces by plastic collisions among the fibres.

The coarser discretization of the spatial domain further brings coarsening of the time scale as the time scale scales with square of the length scale, $T \sim L^2$. As the time scale gets coarser, the interaction forces acting between the immersed fibres and the surrounding fluid become more non-linear and stiffer. The Runge-Kutta time integration scheme, as presented in Švec et al. (2012b), must then use relatively fine sub-steps to properly follow the highly non-linear functions. This inevitably leads to higher computational demands of the numerical simulations per fibre and per time step.

3.4   Conclusions

In the presented paper, we have introduced the problem of accuracy of interaction forces between the immersed rigid cylinders of high aspect ratio and the incompressible Newtonian and non-Newtonian Bingham plastic fluid. We have shown that the Immersed boundary method and consequently the numerical framework as presented in Švec et al. (2012b) is not capable of correctly simulating immersed fibres of sub-grid diameter. Many industrial and natural processes, however, contain a large number of the immersed fibres of high aspect ratio. The use of the fibres of the sub-grid diameter is then inevitable to keep the computational time within reasonable bounds. Our aim was therefore to correct the numerical framework to allow for an accurate representation of the fibres of sub-grid diameter. We have suggested a correction function to recover a correct behaviour of the drag forces acting on the immersed fibres. We have validated the proposed correction function by a distinct example and we have discussed the importance of the correction function to properly simulate distribution and orientation of fibres on a practical example.

3.5   Acknowledgments

Chapter 4

Journal paper 3

Abstract

The ability of the Lattice Boltzmann method, as the fluid dynamics solver, to properly simulate macroscopic Navier's slip boundary condition is investigated. An approximate equation relating the Lattice Boltzmann variable slip boundary condition with the macroscopic Navier's slip boundary condition is proposed. The proposed relation is validated both for the case of Newtonian and non-Newtonian fluids. The importance of employing the Navier's slip boundary condition is highlighted by a practical industrial problem.

4.1 Introduction

The no-slip boundary condition for viscous fluids states that at a solid boundary, the fluid has zero velocity relative to the boundary. The no-slip boundary condition has been a satisfactory representation for majority of the practical problems especially when dealing with homogeneous Newtonian fluids. Complex fluids such as suspensions of solid particles in the non-Newtonian multiphase fluid behave at the molecular level in the same manner as the simple homogeneous Newtonian fluids. The complex fluids are then also commonly assumed to satisfy the no-slip boundary condition. At the macroscopic level, effective properties of the complex fluids start to change as the distance to the solid boundary approaches the size of solid immersed particles. In such a case it can be advantageous to replace the change of the effective properties by a simple Navier's slip boundary condition. The Navier's slip boundary condition was first proposed by Navier in Navier (1823) which states that the component of fluid velocity tangent to the surface should be proportional to the rate of strain at the surface.
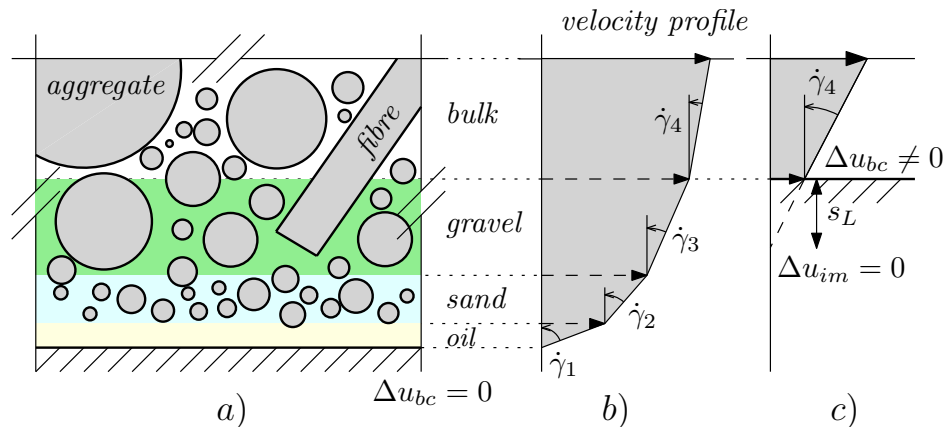
Figure 4.1: *a) Material composition of a typical cross-section of fibre reinforced concrete b) Flow velocities and shear rates of the individual layers c) Illustration of the Navier's slip boundary condition de Gennes (2002); Ahmed and Hecht (2009)*

Figure 4.1a, as an example, illustrates a non-Newtonian heterogeneous fluid used in the structural industry, namely the fibre reinforced self-compacting concrete. Concrete is a highly heterogeneous material as it consists of multiple phases such as gravel, sand, cement, water or even steel fibres. Large immersed particles, such as aggregates or fibres, cannot get into close contact with the solid boundary, which results in the so called wall effect. The

wall effect together with the various types of the solid boundaries of different roughness and treatment add up to a high change rate of the effective properties of the suspension at the vicinity of the solid boundaries. It can no longer be assumed that the macroscopic properties of the fluid (density, viscosity etc.) in the bulk of the material and at the boundary layers are identical. Figure 4.1a, as an example, illustrates composition of the four different layers of the fluid (oil layer, layer of sand, gravel layer and bulk layer). Figure 4.1b illustrates velocity profile of the cross-section together with shear rates of the four individual layers, $\dot{\gamma}_{1-4}$. For the case of Figure 4.1a and Figure 4.1b, the relative velocity between the boundary condition and the adjacent fluid is zero, $\Delta u_{bc} = 0$, satisfying the no-slip boundary condition.

Highly heterogeneous and complex fluids can be numerically represented in different ways. The individual methods are often differentiated by the amount of detail each method provides. The highest resolution is provided by the nature itself. Any current numerical simulation is only a very low resolution approximation of the nature. The larger the structure that we aim to simulate is, the lower resolution of the numerical simulation can be provided. The most straightforward and correct way to numerically simulate a flow of a complex fluid, such as depicted in Figure 4.1a, is to explicitly represent and simulate all the individual constituents of the fluid, which inevitably limits the spatial region of interest. We aim to numerically simulate the casting process of fibre reinforced self-compacting concrete and hence large spatial regions of interest. The resolution of the boundary layers must be therefore significantly reduced.

The various boundary layers, such as the form oil layer, sand or gravel layers, can be then replaced by the aforementioned Navier's slip boundary condition (Navier, 1823; Liao and Wang, 2011; Thrane, 2007). The Navier's slip boundary condition describes the complex boundary problem by a single scalar variable - slip length, s_L (see Figure 4.1c). Contrary to Figure 4.1a, the fluid at the vicinity of the solid boundary of Figure 4.1c does not have zero velocity relative to the boundary, $\Delta u_{bc} \neq 0$. The slip length is then defined as the distance of the solid boundary to an imaginary point where the linearly extrapolated relative velocity of the flow is zero, $\Delta u_{im} = 0$.

Navier's slip boundary condition is commonly incorporated into fluid dynamics solvers directly, i.e. on macroscopic level (Thrane, 2007). Such macroscopic implementation has been widely studied both for the case on Newtonian and non-Newtonian fluids. Lattice Boltzmann method origins in the microscopic theory of ideal gasses. An alternative microscopic representation of the Navier's slip boundary condition might be therefore in the framework of Lattice Boltzmann of interest. A combination of bounce-back boundary condition with specular (mirror like) boundary condition is a very

simple and widely used method of incorporating various types of slip into the Lattice Boltzmann method (Lim et al., 2002; Succi, 2002; Guo et al., 2006). Such a boundary condition deals with reflection behaviour of molecules hitting a solid boundary and thus operates on a microscopic level. To differentiate such a boundary condition from the macroscopic Navier's slip boundary condition, the boundary condition is in this paper called molecular slip boundary condition. Ahmed and Hecht Ahmed and Hecht (2009) pioneered the use of the molecular slip boundary condition to mimic the macroscopic Navier's slip boundary condition for the case of Newtonian fluids. As far as we know, there is currently no paper that shows or validates the use of the molecular slip boundary condition for the case of non-Newtonian fluids. As presented in this paper, we further believe that the function proposed by Ahmed and Hecht Ahmed and Hecht (2009) linking the molecular and macroscopic Navier's slip boundary condition is not completely correct.

The primary aim of this paper is therefore to correct the function proposed by Ahmed and Hecht Ahmed and Hecht (2009) and to validate the corrected function both for the case of Newtonian and non-Newtonian fluids. In this paper, we further show that the corrected function results in a very low and more or less constant error of slip length in the range of 0.015 lattice unit.

This article is a part of a series of articles dealing with development and implementation of a numerical framework capable of simulating flow of fibre reinforced self-compacting concrete. The first article (Švec et al., 2012b) introduced the overall numerical framework. The second article (Švec and Skoček, 2013a) showed a method to numerically simulate a large number of rigid immersed fibres. This article presents a method to include the Navier's slip boundary condition into the Lattice Boltzmann fluid dynamics solver for the case of non-Newtonian fluids.

The fluid dynamics solver is briefly summarized in Section 4.2. Section 4.2.1 describes the Lattice Boltzmann method. Section 4.2.2 introduces a concept of integration of the slip length into the Lattice Boltzmann method by means of the so called molecular slip coefficient. Section 4.3 focuses on various aspects of the Navier's slip boundary condition. Section 4.3.1 proposes a relation linking the molecular slip coefficient to the macroscopic Navier's slip length. The accuracy of the relation is presented for the case of Newtonian fluids in Section 4.3.1 and for the case of non-Newtonian fluids in Section 4.3.3. Section 4.3.2 outlines different methods to compute local shear rates to be used for the Navier's slip boundary condition as well as the influence of the various methods on the accuracy of the proposed relation. The significance of employing the Navier's slip boundary condition is highlighted by a practical industrial problem in Section 4.3.4. Section 4.5 summarizes the article and discusses the main outcomes of the article.

4.2 Fluid dynamics solver

Fluid dynamics is traditionally described by macroscopic partial differential Navier-Stokes equations. Individual methods such as the finite difference method, the finite volume method, the finite elements method, or the smooth-particle hydrodynamics method are differentiated only by the way they solve the Navier-Stokes equations. These approaches formulate the problem by means of macroscopic quantities such as macroscopic velocity or pressure fields. We decided to follow a completely different and historically younger approach called the Lattice Boltzmann method (Wolf-Gladrow, 2000). In the following sections we introduce the Lattice Boltzmann method and explain the implementation of the non-Newtonian behaviour together with the implementation of the Navier's slip into the Lattice Boltzmann method.

4.2.1 Lattice Boltzmann method

The Lattice Boltzmann method, contrary to the aforementioned traditional methods, is based on Boltzmann equations and thus on the theory of ideal gases. One of the advantages of the origin of the Lattice Boltzmann method is the ability to implement slip in a very simple manner (Succi, 2002; Ahmed and Hecht, 2009).

As the Lattice Boltzmann method is based on the theory of ideal gases, the method does not primarily work with macroscopic quantities but rather with mesoscopic particle distribution functions. These can be seen as clouds of microscopic particles, e.g. molecules, chaotically moving in space. Space is commonly discretized into square (2D domain) or cubic Eulerian cells forming a fixed Cartesian grid (see Figure 4.2a). Eulerian nodes, $\mathbf{x}^E \in \Omega^E$, are placed into the centre of each cell and a lattice is formed by connecting the nearest Eulerian nodes. The movement of the microscopic particles is restricted onto the lattice directions, α, which leads into a discretization of continuous particle distribution functions into only a few particle distributions, $f_\alpha \left(\mathbf{x}^E, t \right)$, associated with lattice velocities, $\mathbf{c}_\alpha$. See Figure 4.2b) for a 2D example. There are several lattice types, differentiated on by the shape of the lattice. The $D2Q9$ and $D3Q15$, where D and Q stand for the dimension of the problem and the number of lattice velocities, are two of the most common types adopted.

The vertical and horizontal spacings of the nodes, the reference density of the fluid, $\rho_{f,0}$, and the length of the time step are usually set to unity for the most simple and common lattice types and the simulated problem is scaled accordingly. The provided description of the Lattice Boltzmann method is general and independent of the lattice used, provided that the
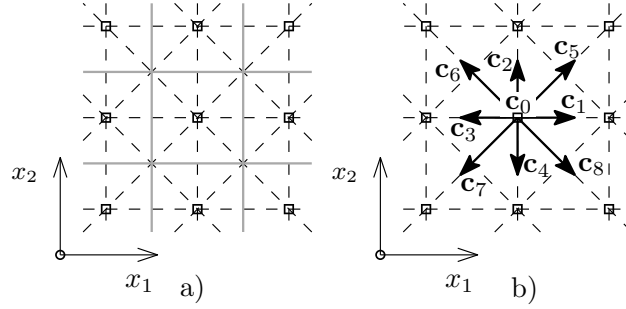
Figure 4.2: *a) Schematic representation of the D2Q9 lattice. Square marks stand for nodes, grey lines for cell boundaries and dashed lines for the lattice. b) Set of corresponding lattice velocity vectors, $\mathbf{c}_\alpha$, in a node.*

reference fluid density, time step and spacing of the nodes are normalized to unity as described above. All the equations presented in this section can be found e.g. in Latt (2007), unless otherwise stated.

An evolution of the particle distributions in space and time is expressed by the Lattice Boltzmann equation

$$\underbrace{f_\alpha\left(\mathbf{x}^E + \mathbf{c}_\alpha, t + 1\right) = f_\alpha\left(\mathbf{x}^E, t\right)}_{\text{streaming}} + \underbrace{f_\alpha^{Ext}(\mathbf{x}^E, t)}_{\text{forcing}} + \underbrace{\Omega_\alpha\left(\mathbf{x}^E, t\right)}_{\text{collision}} . \qquad (4.1)$$

The equation consists of the streaming part, the forcing term and the collision part. The streaming part represents propagation of particle distributions from one node to another along the lattice links. The lattice velocities are chosen in such a way that a particle distribution streams from one node to another node during the unit time step. The forcing term accounts for the effect of an external force in the simplest form in the following way (Mohamad and Kuzmin, 2010; He et al., 1997; Guo et al., 2002)

$$f_\alpha^{Ext}\left(\mathbf{x}^E, t\right) = 3w_\alpha \mathbf{c}_\alpha \cdot \mathbf{F}\left(\mathbf{x}^E, t\right), \qquad (4.2)$$

where w_α stands for weights defined by the type of the lattice. $\mathbf{F}\left(\mathbf{x}^E, t\right)$ represents any external force such as gravity.

The collision part mimics real collisions of the microscopic particles. The collisions are difficult to express explicitly and, therefore, an approximation of the collisions in the form of collision operator, $\Omega_\alpha\left(\mathbf{x}^E, t\right)$, was introduced into the Lattice Boltzmann method. We used one of the simplest collision operators, the so-called Bhatnagar-Gross-Krook operator, see e.g. Chen and Doolen (1998). The Bhatnagar-Gross-Krook operator linearly deforms the

actual particle distributions towards an equilibrium state. The collision operator reads

$$\Omega_\alpha \left(\mathbf{x}^E, t \right) = \frac{f_\alpha^{eq} \left(\mathbf{u}_f, \rho_f \right) - f_\alpha \left(\mathbf{x}^E, t \right)}{\tau \left(\mathbf{x}^E, t \right)}. \tag{4.3}$$

where $\mathbf{u}_f = \mathbf{u}_f \left(\mathbf{x}^E, t \right)$ and $\rho_f = \rho_f \left(\mathbf{x}^E, t \right)$ are the local macroscopic velocity and density of the fluid, respectively. The equilibrium state is represented by equilibrium particle distributions, $f_\alpha^{eq} \left(\mathbf{u}_f, \rho_f \right)$, which are derived from the Maxwell-Boltzmann equation. The equilibrium particle distributions have in the simplest case the following form

$$f_\alpha^{eq} \left(\mathbf{u}_f, \rho_f \right) = \rho_f w_\alpha \left(1 + 3\mathbf{c}_\alpha.\mathbf{u}_f + \frac{9}{2} \left(\mathbf{c}_\alpha.\mathbf{u}_f \right)^2 - \frac{3}{2} \mathbf{u}_f.\mathbf{u}_f \right). \tag{4.4}$$

The local densities and velocities of the fluid are computed as the first two moments of the particle distributions

$$\rho_f \left(\mathbf{x}^E, t \right) = \sum^\alpha f_\alpha \left(\mathbf{x}^E, t \right), \tag{4.5}$$

$$\mathbf{u}_f \left(\mathbf{x}^E, t \right) = \frac{\sum^\alpha f_\alpha \left(\mathbf{x}^E, t \right) \mathbf{c}_\alpha}{\rho_f \left(\mathbf{x}^E, t \right)}.$$

For isothermal conditions, the local pressure is expressed as $p_f \left(\mathbf{x}^E, t \right) = c_s^2 \rho_f \left(\mathbf{x}^E, t \right)$ where c_s is the speed of sound in the given lattice.

The rate of the deformation of the particle distributions towards the equilibrium state is introduced by relaxation time, $\tau \left(\mathbf{x}^E, t \right)$. The relaxation time is computed from the local macroscopic kinematic viscosity of the fluid, $\nu \left(\mathbf{x}^E, t \right)$, by the following relation

$$\tau \left(\mathbf{x}^E, t \right) = \frac{1}{2} + 3\nu \left(\mathbf{x}^E, t \right). \tag{4.6}$$

For a non-Newtonian fluid, the kinematic viscosity is a function of the shear rate tensor, $\dot{\gamma}_{ij} \left(\mathbf{x}^E, t \right)$, and the stress deviator tensor, $S_{ij} \left(\mathbf{x}^E, t \right)$. These tensors are approximated, as described e.g. in Boyd et al. (2006), by

$$\dot{\gamma}_{ij} \left(\mathbf{x}^E, t \right) \approx \frac{3}{2\tau \left(\mathbf{x}^E, t-1 \right)} \sum^\alpha c_{i,\alpha} c_{j,\alpha} f_\alpha^{neq} \left(\mathbf{x}^E, t \right), \tag{4.7}$$

$$S_{ij} \left(\mathbf{x}^E, t \right) \approx \left(1 - \frac{1}{2\tau \left(\mathbf{x}^E, t-1 \right)} \right) \sum^\alpha \left(c_{i,\alpha} c_{j,\alpha} - \frac{\delta_{ij}}{Dim} \mathbf{c}_\alpha.\mathbf{c}_\alpha \right) f_\alpha^{neq} \left(\mathbf{x}^E, t \right), \tag{4.8}$$

where δ_{ij} is the Kronecker delta, Dim is the dimension of the problem and

$$f_\alpha^{neq} \left(\mathbf{x}^E, t \right) = f_\alpha \left(\mathbf{x}^E, t \right) - f_\alpha^{eq} \left(\mathbf{u}_f, \rho_f \right) \tag{4.9}$$

is the non-equilibrium part of the particle distributions.

Description of other parts of the framework such as the implementation of the Bingham plastic rheological model, the free surface implementation or the addition of the immersed solid particles into the fluid dynamics solver can be found in e.g. Švec et al. (2012b); Švec and Skoček (2013a).

4.2.2 Navier's slip boundary condition

Navier's slip boundary condition can be implemented in different ways. One can follow a macroscopic approach by applying, for example, a shear stress boundary condition (Thrane, 2007). Another approach is to utilize the fact that the Lattice Boltzmann method originates from the theory of ideal gasses. The Navier's slip boundary condition can be then approximated as a combination of the no-slip boundary condition and the specular (mirror like) boundary condition, similarly to Succi (2002); Ahmed and Hecht (2009).

Boundary conditions are usually implemented into the Lattice Boltzmann method by a modification of the particle distributions. As a consequence, there is no unique modification of the particle distributions that results in the desired macroscopic boundary condition. Various approaches of different accuracies therefore exist to model a single boundary condition.
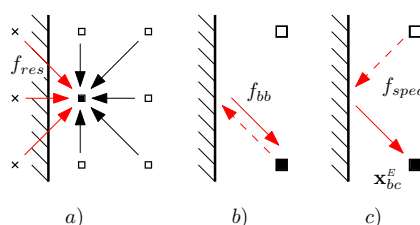
Figure 4.3: *Streaming process of the particle distributions to the node adjacent to the solid boundary (filled black square). a) Black and red arrows stand for known and unknown distributions, respectively b) Bounce-back reflection. c) Specular reflection.*

The simplest form of the no-slip boundary condition is represented by the bounce-back boundary condition (Sukop and Thorne, 2005). Take Figure 4.3a as an example. When a fluid node of interest (filled black square mark) lies next to solid boundary nodes (black cross marks), some particle distributions (red arrows) should be streamed from the solid boundary nodes to the fluid node. These particle distributions do not exist and must be reconstructed. Bounce-back boundary condition provides the simplest possible

form of the reconstruction of the particle distributions, as depicted in Figure 4.3b. Particle distribution (red dashed arrow) is during the streaming process of Eq. (4.1) streamed from the fluid node of interest. The particle distribution hits the solid boundary and reverts back to the original node with opposite velocity (red solid arrow). Bounce-back boundary condition is a very simple boundary condition exhibiting a second order accuracy and a slight numerical slip (He et al., 1997). More complex no-slip boundary conditions have been created to eliminate the numerical slip (Inamuro et al., 1995). The bounce-back boundary condition results in a zero slip length.

Specular boundary condition is illustrated in Figure 4.3c. Particle distribution (red dashed arrow) is streamed from the fluid node adjacent to the fluid node of interest. The particle distribution hits the solid boundary and after the specular reflection it reaches the fluid node of interest (red solid arrow). The specular boundary condition results in an infinite slip length.

Any desired slip length can been reconstructed as a linear combination of the specular and bounce-back boundary condition as

$$f_{res} = (1 - s_c)f_{bb} + s_c f_{spec} , \qquad (4.10)$$

where f_{res} is the resulting particle distribution arriving to the fluid node of interest after the streaming process (see Figure 4.3a). Values f_{bb} and f_{spec} stand for particle distributions obeying the bounce-back and specular boundary conditions, respectively. The linear combination of the two boundary conditions is determined by slip coefficient, s_c. Slip coefficient $s_c = 0$ and $s_c = 1$ correspond to pure bounce-back and specular reflections, respectively.

As an example, the streaming part of Eq. (4.1) will have for an arbitrarily chosen particle distribution, f_8, the following form

$$f_{res} = f_8\left(\mathbf{x}_{bc}^E, t+1\right) = \underbrace{(1 - s_c)f_6\left(\mathbf{x}_{bc}^E, t\right)}_{bounce-back \ reflection} + \underbrace{s_c f_7\left(\mathbf{x}_{bc}^E + \mathbf{c}_2, t\right)}_{specular \ reflection} , \qquad (4.11)$$

where $\mathbf{x}_{bc}^E$ is position of the fluid node of interest, as depicted in Figure 4.3c. The digits in f_6, f_7, f_8 or $\mathbf{c}_2$ stand for particular lattice directions, α, defined in Figure 4.2b.

The described implementation of the variable slip length boundary condition has a completely different origin than the Navier's slip boundary condition. Navier's slip boundary condition is a purely macroscopic description as introduced in Section 4.1 and in Navier (1823); Liao and Wang (2011). Lavallee in Lavallée et al. (1991) on the other hand showed a direct relation between the described boundary condition and molecular experiments conducted by Knudsen back in 1934. The boundary condition therefore in

certain situations behaves differently compared to the Navier's slip boundary condition (Lavallée et al., 1991).

The following section relates the described molecular slip boundary condition to the Navier's slip boundary condition and highlights the ability of the molecular slip boundary condition to effectively mimic the Navier's slip boundary condition for the specified problems.

4.3 Study of the Navier's slip boundary condition

The molecular slip boundary condition, as presented in the previous section, originates from the theory of ideal gasses which determines the behaviour of the boundary condition. In the following sections, we therefore, similarly to Ahmed and Hecht (2009), propose an approximate relation between the molecular slip coefficient, s_c, and the macroscopic slip length, s_L. We further validate the use of the molecular slip boundary condition as the approximation of the macroscopic Navier's slip boundary condition both for Newtonian fluids and non-Newtonian Bingham plastic fluids. We conclude this section by highlighting the importance of inclusion of the Navier's slip boundary condition into the fluid dynamics solver on a practical industrial example.

4.3.1 Newtonian fluids

To validate the molecular slip boundary condition as the approximation of the Navier's slip boundary condition, it is necessary to understand the behaviour of the slip coefficient as defined in Eq. (4.10). The slip coefficient should preferably behave as a material property, similarly to the macroscopic slip length. Thus, the slip coefficient should be devoid of dependency on any non-material property. We have conducted three parametric studies to better understand the behaviour of the slip coefficient for the case of Newtonian fluids.

Parametric study 1

Similarly to Ahmed and Hecht (2009), we simulated the Poiseuille flow of an incompressible Newtonian fluid, i.e. a two dimensional gravity driven flow bounded by two parallel plates (see Figure 4.4). The two parallel plates positioned normal to the z axis were modelled as the molecular slip boundary condition by means of Eq. (4.10). A periodic boundary condition (Sukop and Thorne, 2005) was applied in x and y directions. The flow was driven by

the prescribed constant acceleration, g_x, applied onto the bulk of the fluid. Dimensions of the domain were set to $L_x = 2$, $L_y = 1$ and $L_z = varied$ whereas the density of the Newtonian fluid was set to $\rho_f = 1$.
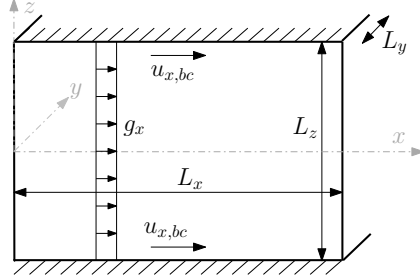
Figure 4.4: *Geometry of the Poiseuille flow*

The Navier's slip length was computed by a linear extrapolation of the velocity of the fluid at the vicinity of the boundary condition as (see Figure 4.1c)

$$s_{L,com} = \frac{u_{x,f} - u_{x,bc}}{2\dot{\gamma}_{xz}} - 0.5 \; , \tag{4.12}$$

where $u_{x,bc}$ is the horizontal speed of the two parallel plates, as depicted in Figure 4.4. Term $u_{x,f}$ is the horizontal component of the velocity of the fluid at the node adjacent to the boundary condition and $\dot{\gamma}_{xz}$ is the xz component of the shear rate tensor at the node adjacent to the boundary condition. The approximation of the shear rate tensor was computed by Eq. (4.7).

The initial velocity of the flow was set to zero. After initiation of the simulation, the flow accelerated until it reached a steady state. The steady-state was assumed when the relative change of the computed slip length in time dropped below 10^{-8}.

A parametric study containing 2000 individual simulations was run to obtain behaviour of the slip length for a range of combinations of the input parameters. In total 500 individual simulations were run for each of the four different values of slip coefficient, $s_c = \{0.1, 0.5, 0.9, 0.98\}$.

The following parameters of the parametric study were randomly generated obeying a uniform distribution and bounded by an interval: Kinematic viscosity of the fluid, $\{\nu \in \mathbb{R} | 0.005 \leq \nu \leq 0.2\} = [0.005, 0.2]$; Vertical length of the domain, L_z in $[30, 60]$; Horizontal acceleration of the fluid, g_x in $[0.005, 0.2]$; Horizontal speed of the two parallel plates, $u_{x,bc}$ in $[-0.03, 0.03]$. The selected intervals of the parameters assured that the maximum speed of the fluid does not exceed 0.05 and hence that the assumption of incompressibility was fulfilled.

Figure 4.5 presents individual results of the parametric study in the form of the macroscopic slip length $s_{L,com}$ as a function of the numerical kinematic viscosity, ν. The figure illustrates the predominant dependency of the slip length on the molecular slip coefficient and on the numerical kinematic viscosity of the fluid. The same observation was also made by Ahmed and Hecht (2009).
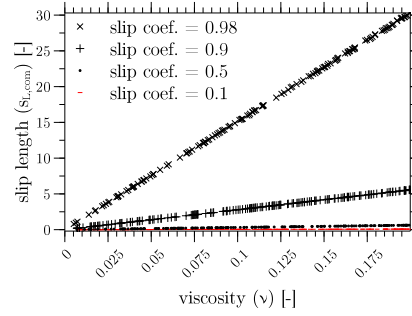
Figure 4.5*: Result of the parametric study in the form of the macroscopic slip length as a function of the numerical kinematic viscosity of the fluid.*

We therefore propose the following approximate relation between the macroscopic slip length and molecular slip coefficient

$$s_{L,approx} = 3\nu \frac{s_c}{1 - s_c} = 3\nu \frac{1 - b_c}{b_c} \ , \tag{4.13}$$

where $b_c = 1 - s_c$ is the molecular bounce-back coefficient. The inverse of the relation then reads

$$s_c = \frac{s_L}{3\nu + s_L}, \qquad b_c = \frac{3\nu}{3\nu + s_L} \ . \tag{4.14}$$

The parametric study showed that aside from the linear dependency on the numerical kinematic viscosity of the fluid, ν, the slip coefficient seems to be devoid of any other non-material property. The conclusion is however limited only to the scope of the presented parametric study. Extremely different time or space scales can result in a different conclusion.

Parametric study 2

The same parametric study as in Section 4.3.1 was run once again, to check the accuracy of the proposed approximate Eq. (4.13) and to validate correctness of the numerical implementation. This time, the macroscopic slip length, $s_{L,in}$, served as an input parameter of the parametric study. The

slip length was inserted into Eq. (4.14). The output of Eq. (4.14), i.e. the slip coefficient, was then inserted into Eq. (4.10). The slip length was randomly generated obeying a uniform distribution and bounded by an interval $s_{L,in} = [0, 100]$. The numerical simulation terminated when the computed slip length, $s_{L,com}$, (see Eq. (4.12)) converged to its final value.

The error of the computed slip length relative to the input slip length was computed as $(s_{L,com} - s_{L,in})/s_{L,in}$. The parametric study resulted in the maximum error of 5% and the average error of 2%. The accuracy of the proposed approximate Eq. (4.13) can be further improved by a modification of the way the local shear rates used in Eq. (4.12) are computed, as presented in Section 4.3.2.

Parametric study 3

A small parametric study of the same layout as depicted in Figure 4.4 was run to compare the proposed approximate Eqs. (4.13) and (4.14) to the proposed approximate solution by Ahmed and Hecht (2009)

$$s_{L,Ahmed} = \frac{\tau s_c}{3(1 - s_c)} \; .$$
(4.15)

Bounce-back coefficient was the main parameter of the parametric study and ranged from $b_c = 0.1$ up to $b_c = 0.999$. Numerical kinematic viscosity of the fluid was set to value $\nu = 0.05$ and $\nu = 0.1$, respectively. Dimensions of the domain were set to $L_x \times L_y \times L_z = 60 \times 1 \times 2$, density of the fluid was set to $\rho_f = 1$ and the horizontal acceleration of the fluid read $g_x = 1 \times 10^{-3}$. Horizontal speed of the two parallel plates was set to $u_{x,bc} = 0$.

Figure 4.6 presents results of the small parametric study in the form of the macroscopic slip length as a function of the molecular bounce-back coefficient. Result of the parametric study matches the proposed approximate Eq. (4.13) reasonably well with the maximum error of approx. 4%. The result of the study, on the other hand, does not match the proposed approximate relation presented in Eq. (4.15) by Ahmed and Hecht (2009). The main difference between Eq. (4.13) and Eq. (4.15) by Ahmed and Hecht (2009) is the use of the kinematic viscosity, ν, instead of the relaxation time, τ (see Eq. (4.6)). We believe that for any non-zero slip coefficient the slip length should approach zero, $s_{L,approx} \to 0$, as the kinematic viscosity of the fluid approaches zero, $\nu \to 0$, (i.e. $\tau \to 0.5$). The proposed approximate Eq. (4.13) complies the requirement.
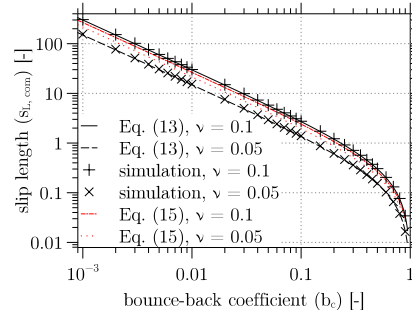
Figure 4.6*: Result of the small parametric study in the form of the macroscopic slip length as a function of the bounce-back coefficient.*

4.3.2   Study of the shear rates

Navier's slip boundary condition, as presented in Section 4.1, requires knowledge of shear rate tensors in the vicinity of the boundary condition (see Eq. (4.12)). The shear rate tensors can be calculated in several ways. The most common approach is to compute local velocity gradients. In the framework of the Lattice Boltzmann method, the shear rate tensors can be approximated by Eq. (4.7), where the Eq. (4.7) computes the average shear rate tensor in the node of interest. Eq. (4.7) therefore computes the shear rate tensor located at the distance of 0.5 lattice units from the edge of the Navier's slip boundary condition. The Navier's slip boundary condition, however, requires knowledge of the shear rate tensors at the edge of the boundary condition. We have therefore constructed yet another approximation of the shear rate tensor and compared it to Eq. (4.7).
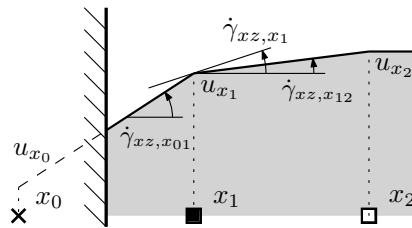
Figure 4.7*: Flow velocity profile in vicinity of the Navier's slip boundary.*

Figure 4.7 illustrates a flow velocity profile at the vicinity of the Navier's slip boundary condition. The aim is to obtain the xz component of the shear rate tensor at the edge of the boundary condition, $\dot{\gamma}_{xz,x_{01}}$, which is unknown. The value of $\dot{\gamma}_{xz,x_1}$ can be either computed from Eq. (4.7) or as the average

of the xz components of the adjacent shear rate tensors, $\dot{\gamma}_{xz,x_{01}}$ and $\dot{\gamma}_{xz,x_{12}}$ as

$$\dot{\gamma}_{xz,x_1} = \frac{\dot{\gamma}_{xz,x_{01}} + \dot{\gamma}_{xz,x_{12}}}{2} = \frac{(u_{x_1} - u_{x_0}) + (u_{x_2} - u_{x_1})}{2} \ . \tag{4.16}$$

The value of u_{x_0} and consequently the value of $\dot{\gamma}_{xz,x_{01}}$ is unknown. The value of $\dot{\gamma}_{xz,x_{01}}$ can be therefore expressed from Eq. (4.16) as

$$\dot{\gamma}_{xz,x_{01}} = 2\dot{\gamma}_{xz,x_1} - \dot{\gamma}_{xz,x_{12}} \ , \tag{4.17}$$

where $\dot{\gamma}_{xz,x_1}$ is computed by Eq. (4.7) and $\dot{\gamma}_{xz,x_{12}} = u_{x_2} - u_{x_1}$.

Section 4.3.1 presented a parametric study of the Poiseuille flow of the Newtonian fluid that resulted in the maximum relative error of 5% and the average relative error of 2%. The relative error was computed as the relative difference between the numerically computed and the analytically computed value of the macroscopic slip length. The parametric study computed the local shear rates by means of Eq. (4.7), i.e. by means of $\dot{\gamma}_{xz,x_1}$ depicted in Figure 4.7.

The computed slip lengths, $s_{L,com}$, (see Eq. (4.12)) of the parametric study were recomputed by means of the alternatively defined shear rate, $\dot{\gamma}_{xz,x_{01}}$ from Eq. (4.17). Figure 4.8 presents the absolute error of the slip lengths, $s_{L,com} - s_{L,in}$, as a function of the input slip length, $s_{L,in}$.
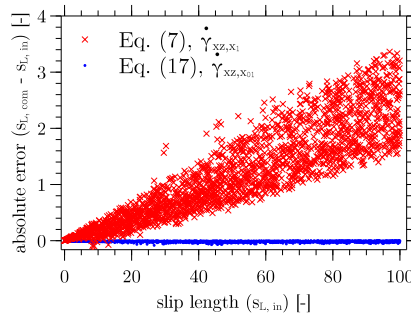
Figure 4.8: *The absolute error of the slip lengths as a function of the input slip length. Both x and y axes are given in lattice units.*

The results are shown both for the traditional shear rates computed by Eq. (4.7) and for the alternative shear rates computed by Eq. (4.17). Results of the traditional shear rates indicate a linear dependence of the absolute error on the input slip length whereas results of the alternative shear rates indicate a constant dependency of the absolute error on the input slip length. The average absolute error of the results of the alternative shear rates oscillates around 0.015 lattice units.

This section presented a modified way of calculation of the shear rates to be used in Eq. (4.12). The presented modification of the shear rates resulted in almost constant and very low absolute error of the numerically computed slip length with respect to the input slip length. The observation further strengthens the validity of the proposed approximate Eq. (4.13).

4.3.3 Non-Newtonian fluids

In Section 4.3.1, we have introduced the relation between the molecular slip coefficient and the macroscopic Navier's slip length. Similarly to Ahmed and Hecht (2009), we have observed that the molecular slip coefficient is a function of both the macroscopic slip length and the numerical kinematic viscosity of the fluid (see Eq. (4.14)). The kinematic viscosity of the fluid is in the case of the incompressible Newtonian fluids constant both in time and space. The viscosity is on the other hand in the case of the Non-Newtonian fluids, such as a Bingham plastic fluid, variable and often shear-dependent. The molecular slip coefficient therefore becomes variable and shear-dependent as well. For a typical numerical problem, the macroscopic slip length is predefined and constant both in time and space. The molecular slip coefficient is then computed from Eq. (4.14) and applied into Eq. (4.10).

We propose in Eq. (4.14) to use a local kinematic viscosity of the fluid positioned at the same location as the fluid node of interest. As an example, the local kinematic viscosity of the fluid to be used in Eq. (4.14) and subsequently in Eq. (4.11) can be computed as the average of the two adjacent local viscosities, $\nu = 0.5 \left[\nu \left(\mathbf{x}_{bc}^E, t \right) + \nu \left(\mathbf{x}_{bc}^E + \mathbf{c}_2, t \right) \right]$.

Parametric study 1

A small parametric study was run to validate correctness of the aforementioned proposition. Similarly to Section 4.3.1, a gravity driven Poiseuille flow was used in the parametric study. Dimensions of the domain were set to $L_x \times L_y \times L_z = 20 \times 1 \times 2$. Molecular slip coefficient was set to $s_c = 0.9$. Horizontal acceleration of the fluid read $g_x = 0.01$. Horizontal speed of the two parallel plates was set to $u_{x,bc} = 0$ whereas the density of the Newtonian fluid was set to $\rho_f = 1$. Numerical kinematic viscosity of the fluid cells directly adjacent to the boundary nodes was set to $\nu_{outer} = 0.05$ (see grey region in Figure 4.9). Four different numerical simulations were run. In each numerical simulation, the bulk of the fluid had one of the following numerical kinematic viscosities $\nu_{inner} = \{0.05, 0.08\bar{3}, 0.11\bar{6}, 0.15\}$, corresponding to relaxation times $\tau_{inner} = \{0.65, 0.75, 0.85, 0.95\}$.
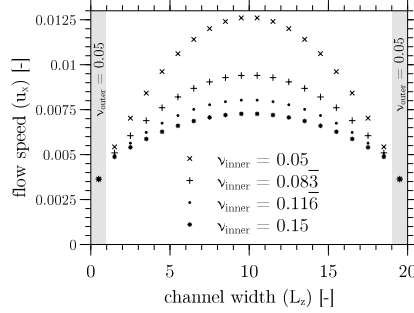
Figure 4.9: *Velocity profiles of the Poiseuille flow for various numerical kinematic viscosities in the bulk of the fluid domain.*

All the individual numerical simulations of the parametric study ended up having the same computed macroscopic slip length, $s_{L,com} = 1.42$. The proposed approximate Eq. (4.13) predicts the following macroscopic slip length

$$s_{L,approx} = 3\nu \frac{s_c}{1 - s_c} = 3 \times 0.05 \frac{0.9}{1 - 0.9} = 1.35 \qquad (4.18)$$

indicating approx. 5% relative error between the two macroscopic slip lengths. The fact that all the numerical simulations resulted in the same macroscopic slip length, $s_{L,com} = 1.42$, indicates that the molecular slip coefficient is, aside from the slip length, dependent only on the local kinematic viscosity of the fluid nodes directly adjacent to the boundary condition node of interest. If the proposed approximate Eq. (4.13) was dependent on the kinematic viscosity in the bulk of the fluid, the individual numerical simulations of the parametric study would result in various different macroscopic slip lengths, $s_{L,com}$.

Parametric study 2

A parametric study similar to Section 4.3.1 was run to check the accuracy of the proposed approximate Eq. (4.13) for the case of non-Newtonian Bingham plastic fluids. The macroscopic slip length, $s_{L,in}$, served as an input parameter of the parametric study. The slip length was randomly generated obeying a uniform distribution and bounded by an interval $s_{L,in} = [0, 100]$. The yield stress of the Bingham plastic fluid was randomly generated ranging from $S_{yield} = 0$ up to $S_{yield} = 2 \times 10^{-5}$. The numerical simulation terminated when the slip length, $s_{L,com}$, computed by Eq. (4.12) converged to its final value. Eq. (4.7) was used to calculate the shear rate tensors at the nodes adjacent to the boundary condition.

The error of the computed slip length relative to the desired slip length was computed as $(s_{L,com} - s_{L,in})/s_{L,in}$. The numerical parametric study resulted in the maximum error of 6% and the average error of 3%.

4.3.4 Application - Plate casting

Previous sections presented the implementation of the Navier's slip boundary condition into the framework of the Lattice Boltzmann method and highlighted its validity for a wide range of applications. This section illustrates the importance of employing the Navier's slip boundary condition on a practical industrial problem. Numerical framework applied in the following section is a combination of the various parts of the framework presented in this paper and in Švec et al. (2012b); Švec and Skoček (2013a). Preliminary results of the work are presented in Švec et al. (2012c).

A growing portion of civil structures are nowadays constructed of self-compacting concrete. Contrary to an ordinary concrete, the self-compacting concrete flows and fills the form-work without any need of vibration or other agitation. Steel reinforcement is often used to improve the behaviour of concrete loaded in tension. It is, for example, very advantageous to add steel fibres into a self-compacting concrete to maintain a simple casting procedure, yet featuring better tensile properties of the concrete. The immersed steel fibres very quickly orient due to the flow of the concrete and as such, properties of the final structural elements are heavily dependent on the flow the material experienced during the casting process of the elements. Especially for thin elements, the flow of the material is significantly influenced by the boundary-fluid interaction.

The following section therefore highlights the importance of inclusion of the Navier's slip boundary condition model into the fluid dynamics solver to properly predict the final orientation of the steel fibres immersed in the self-compacting concrete.

Plate of dimensions $1.2\,\text{m} \times 1.2\,\text{m} \times 0.15\,\text{m}$ and made of the self-compacting fibre reinforced concrete was cast (see Figure 4.10). Rheology of the self-compacting concrete can be approximated by a Bingham plastic model. Density, plastic viscosity and yield stress of the fibre reinforced self-compacting concrete were $2500\,\text{kg/m}^3$, $75\,\text{Pa s}$ and $25\,\text{Pa}$, respectively. The fibre volume fraction of the immersed steel fibres was 0.5%. The length of the fibres, the aspect ratio and the density of the fibres was $6\,\text{cm}$, 80 and $7850\,\text{kg/m}^3$, respectively. The casting was conducted from a rubber tube located at a distance of $0.25\,\text{m}$ from one of the corners of the plate (marked as a blue cylinder in Figure 4.10). The cast plate was left to harden for a period of 28 days. A beam of dimensions of $0.6\,\text{m} \times 0.15\,\text{m} \times 0.15\,\text{m}$ was cut out of the
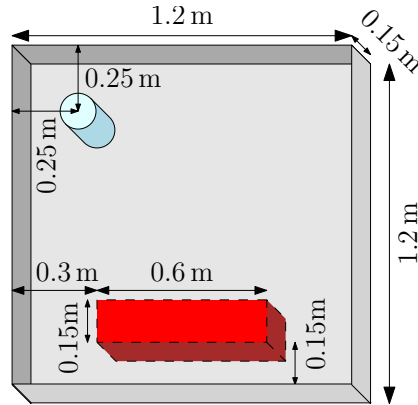
Figure 4.10: *Geometry of plate casting. Grey denotes the form-work, blue stands for the rubber inlet and red represents the cut beam.*

plate (marked as a red prism in Figure 4.10). The whole beam was afterwards scanned by a medical computed tomography device to obtain the 3D view of all the steel fibres located in the beam.

Figure 4.11a depicts the orientation of the immersed fibres located in the lower half of the beam by means of 2D orientation tensors, i.e. orientation ellipses (Advani and Tucker, 1987). Each orientation tensor usually replaces tens or hundreds of the immersed fibres. The more circular the orientation ellipse is, the more random orientation of the immersed fibres is present in that area. Elongated ellipses on the other hand represent highly oriented immersed fibres in that region. Figure 4.11a, as an example, shows both the immersed fibres and their respective orientation ellipses. Figure 4.11a indicates that the majority of the immersed fibres are oriented vertically.

A numerical simulation (see Figure 4.12) was run to compare the experimentally obtained orientation ellipses to the numerically obtained orientation ellipses and thus to highlight the importance of the inclusion of the Navier's slip boundary condition into the fluid dynamics solver.

All the parameters of the numerical simulation were identical to the aforementioned experiment. Space was discretized by $1\,\mathrm{cm} = 1$ lattice unit. Time was discretized by fixing the relation between the numerical kinematic viscosity of the fluid and the effective viscosity of the fluid as $90\,\mathrm{Pa\,s} = 0.1$ lattice unit. All the sides of the form-work (see grey regions of Figure 4.10) were modelled by the Navier's slip boundary condition. In total 3 numerical simulations were run differentiated by the slip length applied, $s_L = \{0\,\mathrm{cm}, 8\,\mathrm{cm}, \infty\,\mathrm{cm}\}$.

Figure 4.11b,c,d presents the results of the numerical simulation in the
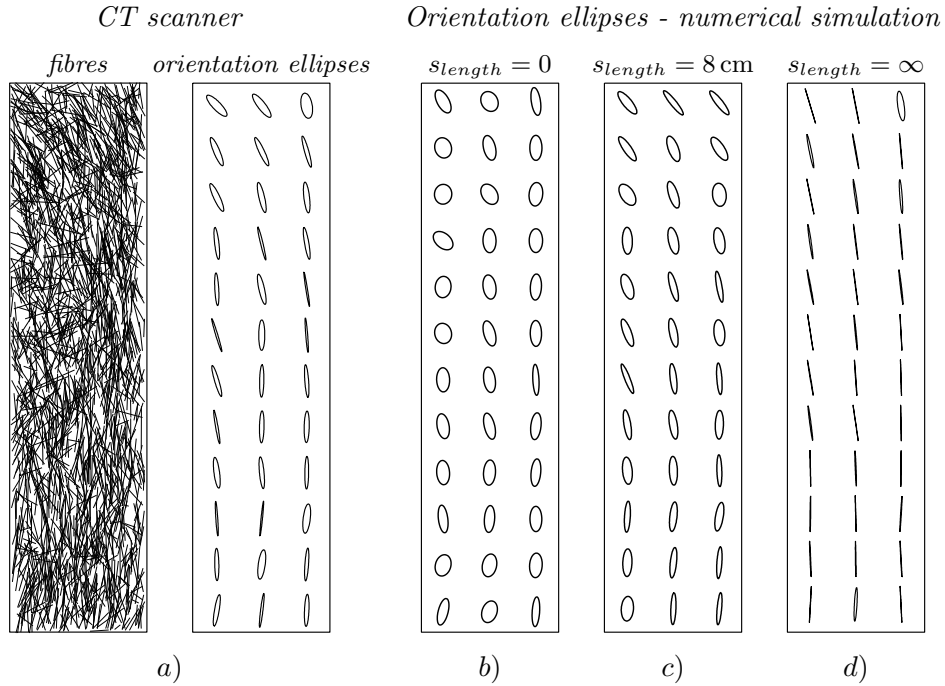
Figure 4.11: *Top view of the lower half of the cut beam. Each ellipse stands for the 2D orientation tensor and replaces tens of fibres.*

form of the orientation ellipses computed at the same location as the orientation ellipses obtained experimentally and presented in Figure 4.11a. If the simple no-slip bounce-back scheme is used in the numerical simulations, the Navier's slip length becomes $s_L = 0$ cm and the orientation ellipses depicted in Figure 4.11b will be obtained. Notice the big differences in the shapes of the respective orientation ellipses between Figure 4.11a and Figure 4.11b. The numerical simulation predicts too random orientation of the immersed fibres in the region close to the boundary condition when the no-slip boundary condition is employed. This observation suggests that in reality some kind of the macroscopic apparent slip occurs, as introduced in Section 4.1.

The effect of the apparent slip naturally vanishes with an increasing distance from the boundary condition. The difference between Figure 4.11a and Figure 4.11b,c,d therefore shows the importance of employing the Navier's slip boundary condition and the importance of correctly estimating the macroscopic slip length, especially for the case of thin structural elements, such as plates or beams.
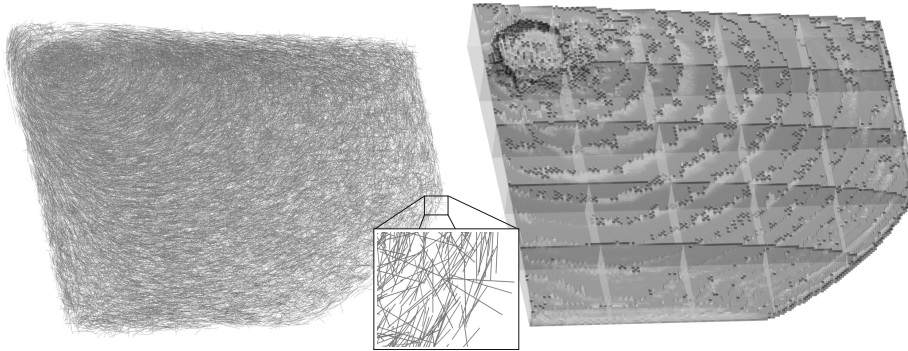
Figure 4.12*: 3D view of the numerical simulation at an intermediate step. Left = immersed steel fibres; Right = Bingham plastic fluid.*

4.4   Discussion

Spatial discretization of the fluid domain in Section 4.3.4 was set to $1\,cm =$ 1 lattice unit. The immersed steel fibres of length $6\,cm$ are then discretized into 6 lattice units. Such a discretization was chosen based on our experience. We have run a range of various numerical simulations with fibres discretized into 3 lattice units, 6 lattice units, 12 lattice units or 24 lattice units. The accuracy of the resulting fibre orientation expectably reduced with the reduced fibre discrete length. We however found the accuracy of simulations with fibre discrete length of 6 lattice units satisfactory and comparable with the finer fibre discretization lengths. For large scale simulations, we therefore find 6 lattice units as a reasonable trade-of between the accuracy and the computational speed.

The proposed representation of the macroscopic Navier's slip boundary condition in form of molecular boundary condition was in this paper validated on a limited set of examples. All the examples were targeted towards validation of the proposed method to properly mimic various formwork surfaces in the building industry, especially for the case of fibre reinforced self-compacting concrete casting. It therefore remains unclear how the proposed representation would behave in other situations, such as for the case of curved surfaces.

4.5   Conclusions

In the presented paper, we have introduced the problem of correctly implementing the macroscopic Navier's slip boundary condition into the framework

of the Lattice Boltzmann method. We have proposed an approximate relation linking the molecular slip coefficient to the macroscopic slip length. We have validated the proposed relation both for the case of Newtonian and non-Newtonian fluids. An alternative way to compute local shear rates to be used for computing the macroscopic slip length was presented. We have shown that the alternative way to compute the shear rates results in a very low and almost constant error of the computed slip lengths compared to the input slip lengths. We have shown the significance of employing the macroscopic Navier's slip boundary condition into the fluid dynamics solver on a practical industrial problem.

4.6 Acknowledgments

Chapter 5

Conference paper 1

Title:	Application of the fluid dynamics model to the field of fibre reinforced self-compacting concrete
Authors:	O. Švec, J. Skoček, H. Stang, J. F. Olesen, L. N. Thrane
Conference:	In Proceedings of the International Conference on Numerical Modeling Strategies for Sustainable Concrete Structures (SSCS), Aix-en-Provence, France, 2012.

Abstract

Ability to properly simulate a form filling process with steel fibre reinforced self-compacting concrete is a challenging task. Such simulations may clarify the evolution of fibre orientation and distribution which in turn significantly influences final mechanical properties of the cast body. We have developed such a computational model and briefly introduce it in this paper. The main focus of the paper is towards validation of the ability of the model to properly mimic the flow of the fibre reinforced self-compacting concrete. An experiment was conducted where a square slab was filled with the fibre reinforced self-compacting concrete. A computational tomography scanner together with an image analysis were used to obtain a field of fibre orientation tensors. These tensors were compared to the tensors obtained by the simulation. The comparison shows the ability of the model to predict the real behaviour of the self-compacting fibre reinforced concrete.

5.1 Introduction

Concrete is a complex material. Its composition makes it extremely difficult to predict the final detailed behaviour of structural elements. Adding steel fibres to self-compacting concrete makes the concrete even more unpredictable. It cannot be assumed to be an isotropic material any more since the fibres orient and disperse during the flow. The knowledge of the final orientation and dispersion of fibres in the structural elements could provide a basis for understanding how the fibres influence the final mechanical properties of the structural elements.

Experimental work leading to the knowledge of orientation and dispersion of fibres is often a very time and resource consuming procedure. One has to do the casting of the elements. The cast element has to be left to harden, cut into pieces and only then a computational tomography (CT) scanner can be used to obtain the 3D image of the fibres in the elements. However, only small parts of the elements can be CT scanned due to the fast overheating of the device. Another option could be to cut the element into many slices and then visually compute the number and position of individual fibres along these sections (Sarmiento, 2011). A completely different approach might be to use a transparent yield stress fluid such as Carbopol (Švec et al., 2012a) to replace the fluid matrix of self-compacting concrete. All these approaches are not simple and, therefore, only a limited amount of information is obtained from such experiments. On the other hand, numerical simulations are limited only by the computational power. A simulation tool capable of simulating a flow of self-compacting concrete together with fibres and the largest aggregates could provide a sufficient alternative for obtaining the required information.

In this paper, we introduce such a model. We further present a comparison of the simulation model with a real-world experiment. At the end of the paper, we show that our model predicts the final orientation of fibres sufficiently well and in a reasonable amount of time.

5.2 Methods

In this section, we present the two-way coupled model for the flow of suspensions of rigid solid particles in a non-Newtonian fluid. The model consists of the fluid dynamics part used to predict the free surface flow of a homogeneous fluid. The model is also capable of predicting the time and space evolution of the solid particle suspensions.

Due to the diversity of the individual phenomena, the overall model is separated into three distinct levels (Figure 5.1):

a) **Level of fluid:** Flow of a non-Newtonian free surface fluid is solved at this level. The Lattice Boltzmann method (Wolf-Gladrow, 2000; Sukop and Thorne, 2005) is used as the fluid dynamics solver whereas the Mass Tracking Algorithm describes the free surface of the flow. This level is influenced by the interaction forces coming from the "Level of fluid - solid particles interaction".

b) **Level of fluid - solid particles interaction:** This intermediate level provides a communication channel between the "Level of fluid" and the "Level of solid particles". The communication takes place via force interactions. We have used the Immersed boundary method with direct forcing (Feng and Michaelides, 2005) to accommodate the communication between the two levels. No-slip boundary condition between the fluid and the solid particles is enforced. To satisfy this condition, an interaction force is created and sent back to the "Level of fluid" and the "Level of solid particles".

c) **Level of solid particles:** Solid particles with an exact analytical geometry are used at this level. The dynamics of the solid particles is solved using Newton's equations of motion. Interactions among the solid particles and between the solid particles and the boundaries (such as walls etc.) are also solved. This level is influenced by the interaction forces coming from the "Level of fluid - solid particles interaction".
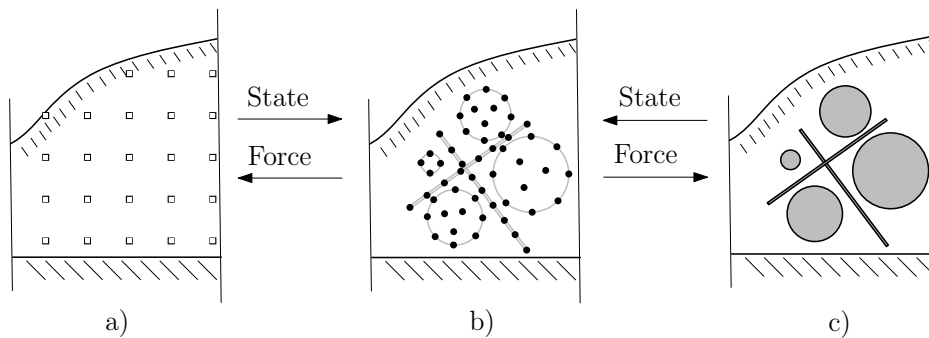
Figure 5.1: *Scheme of the model. a) Level of fluid, b) Level of fluid - solid particles interaction, c) Level of solid particles.*

5.2.1   Level of fluid

Level of fluid solves the flow of a homogeneous non-Newtonian free surface fluid and thus consists of the fluid dynamics and free surface solver.

Fluid dynamics solver

In contrast to the traditional computational fluid dynamics methods, where the problem is formulated by means of macroscopic quantities such as space and time dependent velocity and pressure fields, the Lattice Boltzmann method, with its roots in the kinetic theory of gases, treats the fluid as clouds of microscopic particles (e.g. molecules). Individual microscopic particles are assumed to be freely propagating through the space while instantaneously colliding among each other from time to time (see Lattice gas cellular automata (Wolf-Gladrow, 2000)). The clouds of particles are approximated by continuous particle distribution functions (i.e. probability of a particle occurrence). The particle distribution functions are further discretized by a set of discrete particle distributions to limit the number of unknowns. Lattice Boltzmann equation provides rules for mutual collisions and propagation of the particle distributions. The macroscopic quantities (density, velocity et.) can then be computed as moments of the particle distributions.

The computational domain is typically discretized by a set of Eulerian cells[1] of a uniform size (see Figure 5.1a). Continuous fields of macroscopic quantities (such as velocity fields) are then approximated by the mean values of the quantities in the discretized cells. Similarly, the time is discretized into uniform time steps.

In a given time step, the state of the fluid in a cell is fully described by the particle distributions in that cell. The particle distributions in the given time step at a certain position are computed from the particle distributions in neighbouring cells in the previous step. This accounts for the propagation of the particle distributions. Collisions of the particle distributions are in the simplest case approximated by a linear transformation of the particle distributions towards the local equilibrium state. Such a transformation is called Bhatnagar-Gross-Krook collision operator (Chen and Doolen, 1998). The local equilibrium state is based on the Maxwell-Boltzmann distribution, and is computed from the local macroscopic velocity and pressure (density) of the fluid.

Free surface algorithm

A free surface has been implemented in the form of the Mass Tracking Algorithm (Körner et al., 2005). The algorithm makes use of the same Eulerian discretized domain as the Lattice Boltzmann method where fluid, gas and interface cells are introduced. The Lattice Boltzmann equation is computed in the fluid and interface cells, only. Gas cells are empty cells where noth-

---

[1]Nodes fixed in space

ing is computed. Interface cells separate fluid phase and gas phase and are therefore responsible for a correct implementation of the free surface algorithm and for the correct mass conservation of the fluid. Interface cells are moreover the only place where the Mass Tracking Algorithm comes into play in the form of local mass tracking and reconstruction of missing information from the gas phase.

5.2.2   Level of fluid - solid particles interaction

The Immersed boundary method with direct forcing (Feng and Michaelides, 2005) provides a direct linkage between the "Level of fluid" and the "Level of solid particles". The fluid can "feel" the solid particles in the form of a force field. In the same manner, the solid particles can "feel" the fluid in the form of forces acting on the solid particles. At this level, the solid particles are discretized into a set of Lagrangian nodes[2] (see black circle marks in Figure 5.1b). It is assumed that the velocity of a solid particle and the fluid at the same Lagrangian node are equal due to the no-slip boundary condition. Non-equal velocities are transformed into a force field acting on both the particle and the fluid. The force is in the simplest form computed based on Newton's second law of motion (i.e. such a force to accelerate a certain volume of the fluid that is surrounding the Lagrangian node to the velocity of the solid particle at that Lagrangian node). Since the Lagrangian nodes usually do not coincide with the Eulerian nodes (coming from the "Level of fluid"), the velocity of the fluid in the Lagrangian nodes is obtained by a volume averaging of the velocities at the Eulerian nodes. The volume averaging is conducted by means of a Dirac delta function (Yang et al., 2009). The resulting forces are usually extrapolated from the Lagrangian nodes back to the Eulerian nodes (i.e. to the "Level of fluid") using the same Dirac delta function.

The Immersed Boundary Method provides, contrary to other methods (e.g. bounce-back wall scheme (Ladd, 2006a,b)), smooth and stable time evolution of all the quantities (i.e. the position of the solid particles or forces acting on them). The most important feature of the Immersed Boundary Method, however, is its ability to simulate small objects of only a few lattice units or even sub-grid sized objects, see (Švec et al., 2011). This results in a significant reduction of the computational time needed.

---

[2]Position of the nodes evolves in time

5.2.3   Level of solid particles

At this level, the solid particles are assumed to be rigid bodies of a simple geometric shape (sphere, ellipsoid or cylinder) with the ability to move, rotate and interact among each other, with fluid, walls and other obstacles. The dynamics of those immersed solid particles is driven by Newton's second law of motion which is discretized with the explicit Runge-Kutta-Fehlberg time integration scheme with an adaptive time step. The numerical integration scheme that we adopted ensures the stability and accuracy of the simulation even for a highly non-linear behaviour.

An accurate and robust treatment of interactions among the solid particles and between the solid particles and other obstacles such as walls or reinforcement plays an important role in a proper description of the relevant phenomena. The model includes two types of interactions, namely mutual instantaneous collisions of solid particles and continuous forcing of a general type. The instantaneous collisions were approximated by means of force impulses (Švec et al., 2012b) An example of the continuous forcing could be a lubrication force correcting the fluid flow between two solid particles in the case when the two solid particles approach each other to a sub-grid distance (Nguyen and Ladd, 2002).

5.3   Applications

Any simulation tool should be validated preferably against both analytical solutions and as many experiments as possible. The in-depth description of the presented model and its basic validation was performed in Švec et al. (2012b). The main task of this paper is to show the capability of the model to properly describe the complex behaviour of fibre suspension in a self-compacting concrete. To do so, the orientation of fibres as a result of the simulation model is compared with the orientation of fibres in the real experiment.

5.3.1   Plate experiment

The plate experiment was conducted by the Danish Technological Institute where a plate of size 1.6 x 1.6 x 0.15 m was cast (see Figure 5.2a). The casting was performed from a circular inlet with a diameter of 20 cm and positioned in the corner of the plate at a distance of 300 mm from the sides of the slab. The speed of filling was 2 m/s. Density of the self-compacting concrete was approximately 2300 kg/m^3 whereas density of the fibres was 7850 kg/m^3. Bingham rheology parameters, i.e. plastic viscosity and yield

stress, of the suspension of steel fibres in the self-compacting concrete were measured using 4C-Rheometer (Thrane et al., 2010). The averaged resulting values at the time of casting were 45 Pa and 75 Pa s for the yield stress and the plastic viscosity, respectively. A volume fraction of 0.5 % of straight steel fibres with hooked ends (Bekaert Dramix RL 80/60 BN) were used in the experiment, corresponding to 40 kg/m^3.

a)   b)
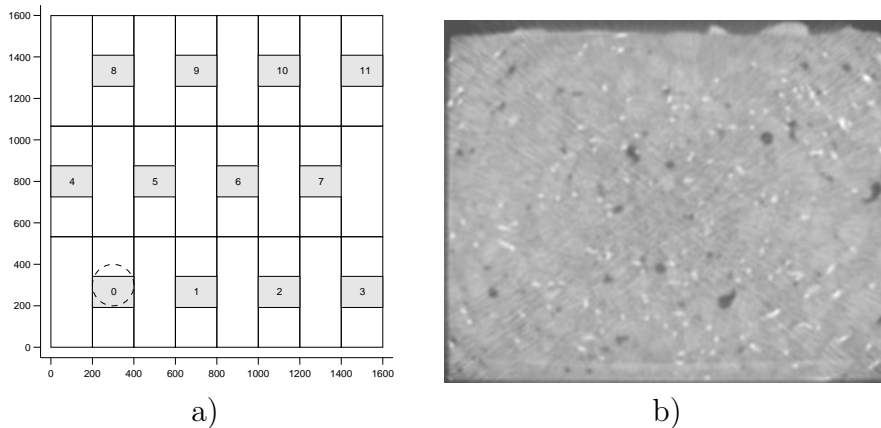
Figure 5.2: *a) Scheme of the plate. White rectangles represent the standard beams. Grey rectangles stand for the CT scanned regions. The dashed circle mark is the inlet. b) An example of a CT scanned slice. White regions represent sections of the steel fibres whereas dark regions are the air voids.*

The casting lasted for approximately 30 seconds. The plate was left to harden for 28 days and then cut into 24 standard sized beams. "HiSpeed CT/i" scanner produced by "Ge Medical Systems" was used to scan 12 middle sections of the chosen standard beams (see grey rectangles in Figure 5.2a). The dimensions of the scanned volume were 200 x 150 x 150 mm. A set of DICOM images was obtained as the output of the CT scanner where each image represented a slice of the specimen (see Figure 5.2b). A 3D model was reconstructed from the series of slices (see Figure 5.3a). A 3D thresholding technique was used to remove the concrete and the air voids (i.e. the dark regions). Subsequently, a 3D skeletonization technique was applied to obtain a set of 3D lines (see Figure 5.3b).

The orientation of fibres in individual regions was represented by means of second order orientation tensors similarly to Advani and Tucker (1987). The orientation tensors were visualized in the form 3D ellipsoids and in this paper in the form of 2D ellipses (see Figure 5.4). The orientation of the ellipses represent the mean orientation of fibres in the region. Aspect ratio of the ellipses represents the alignment of fibres in the region. High aspect

ratio of the ellipses corresponds to a high alignment of the fibres and vice versa the circular shape of the ellipses corresponds to a uniformly random orientation of fibres.

a)   b)
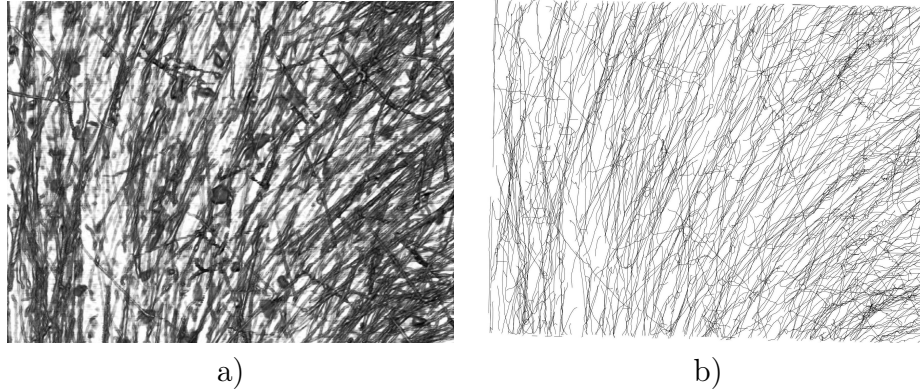
Figure 5.3: *a) Top view of the 3D model. b) Top view of the thresholded and skeletonized 3D model of the CT scanned sample.*

The main outcome of the experiment was a set of 3D ellipsoids representing the orientation of fibres in the plate. Figure 5.4 presents two top views of the plate together with orientation ellipses in the CT scanned regions. The upper third and the lower third of the plate are shown in the figure to highlight the differences in ellipses through the depth of the plate.

One may notice that the fibres orient quite significantly. The fibres tend to orient normal to the flow direction which forms a circular pattern. The longer the distance from the inlet the more the orientation of fibres increase. The fibres in the bottom third of the plate seem to be more randomly distributed in comparison to the upper third of the plate but the difference is not that pronounced.

This was surprising, as the presented simulation predicted an almost complete randomness of the fibre orientation in the bottom third of the plate. A reasonable explanation might be a boundary effect as described in Jacobsen et al. (2010). An apparent Navier's slip (Thrane, 2007) probably occurred during the experiment and should be taken into account in the simulation.

5.3.2 Plate simulation

A simulation of the aforementioned plate was run using the model introduced in the Section 5.2 (see Figure 5.5). All the parameters (geometry, rheology) were taken from the experiment. Coulomb friction was applied among the fibres and between the fibres and the boundary condition. The values of static
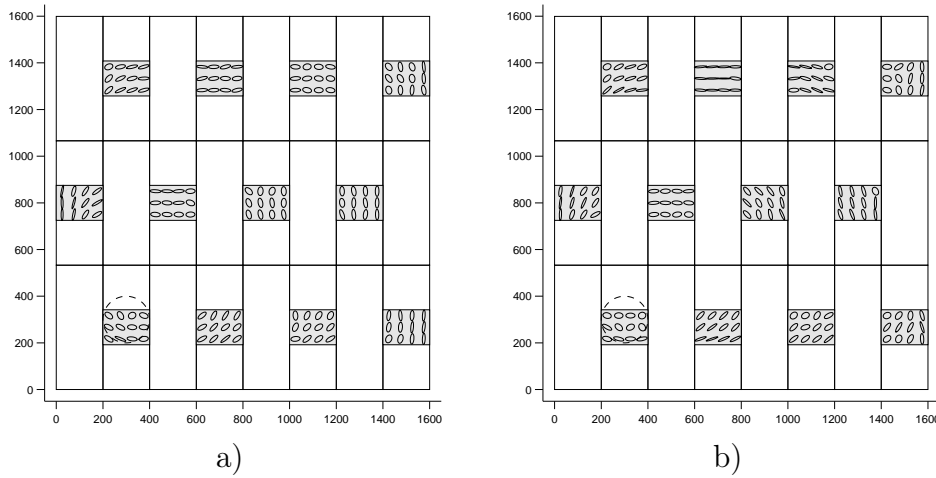
Figure 5.4: *Top view of the lower (a) and upper (b) third of the plate cut into standard beams (white rectangles). Ellipses represent fibre orientations of the CT scanned regions (grey rectangles).*

and dynamic friction were both set to 0.3. In addition, all the collisions of the fibres were assumed to be plastic, i.e. coefficient of restitution was set to 0.
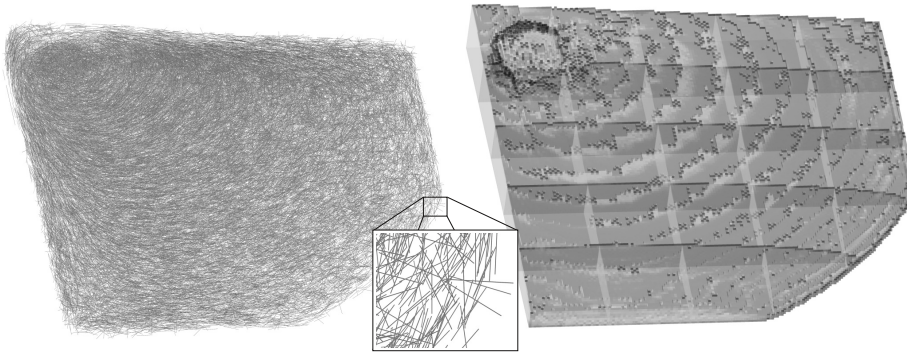
Figure 5.5: *A 3D view of the fibres (left) and the fluid (right) during the simulation.*

The computational domain of the fluid was discretized by 1 cm = 1 lattice units. Length and diameter of the discretized fibres was then 6 and 0.075 lattice units. A correction term of the forcing evaluated by the Immersed boundary method (introduced in Švec et al. (2011)), which allows for sub-grid sized diameters of the fibres, was applied during the simulation. The overall domain was spatially parallelized, i.e. sub-divided into 25 sub-domains (see

Figure 5.5 right) to speed up the computations. The computation started with one running sub-domain, adding additional sub-domains as the flow spread. The total number of fibres reached 72 433, i.e. ca. 2900 fibres per sub-domain. The simulation was run on 32 cores Intel Xeon X7550 2.00 GHz with 64 GB RAM and took approx. 1 week of computations. Approximately 95 % of the computational power was spent on solving the "Level of solid particles" and the "Level of fluid - solid particles interaction". Only 5 % of the computation power was spent on solving the "Level of fluid". The final orientation of fibres obtained from the simulation is presented in Figure 5.6.
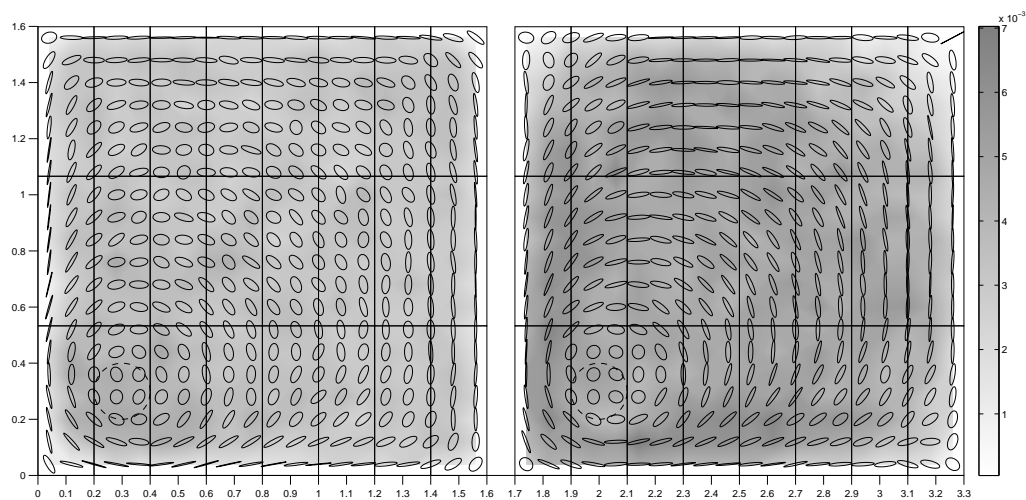
Figure 5.6: *Top view of the lower (left) and upper (right) third of the plate at the end of the simulation. The grey scale stands for an estimate of the fibre volume fraction.*

As mentioned in the previous section, an apparent slip occurred during the experiment. There are at least two ways to incorporate the apparent slip into the simulation model. The most obvious one is to include a thin layer of a fluid with reduced viscosity near the form-work. This approach creates troubles with the stability of the model due to high differences in the viscosities in the domain. A numerical time step would have to be significantly reduced leading to a high increase of the computational time. We have therefore decided to use a more "artifical" way of describing the apparent slip, i.e. the "molecular slip" as described in Lavallée et al. (1991). The advantage of such an approach is the stability of the model even for high values of the apparent slip. The disadvantage is that there is no direct relation between the real apparent slip and the "molecular slip" and, therefore, the value has to be fitted. We ran the simulation with a slip coefficient of 0.85, 0.9, 0.95 and

1.0, and observed the best correlation with the experiment with the values of 0.9 and 0.95. Figure 5.6 presents the results where a slip coefficient of 0.9 was used.

5.4 Comparison

Figure 5.7 presents a comparison of the orientation ellipses obtained from the simulation (solid red) with the orientation ellipses obtained from the experiment (dashed black) in the CT scanned regions. There seems to be a nice correlation between the experiment and the simulation in most places. Near to the inlet, the ellipses do not match perfectly which is probably caused by a slightly inaccurate positioning of the inlet in the simulation as compared to the experiment.
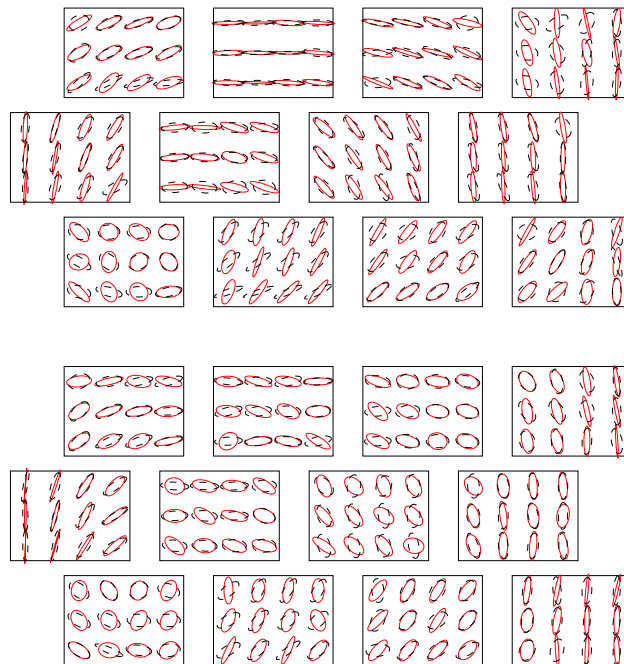
Figure 5.7: *Comparison of the CT scanned ellipses (dashed black) and ellipses obtained by the simulation (solid red). Top part shows the upper third of the plate whereas the bottom part present the lower third of the plate.*

5.5   Conclusions

A model capable of simulating the flow of fibre reinforced self-compacting concrete was presented. An experiment was conducted to show the abilities of the model to correctly describe the final orientation of fibres. A plate was filled with the fibre reinforced self-compacting concrete, left to harden, cut into standard sized beams and scanned by a CT scanner. Ellipses were then constructed to represent the fibre orientation in different regions. A simulation was run with the experimentally established parameters and the orientation ellipses were compared to the experiment.

The comparison showed capability of the model to simulate the flow of fibre reinforced self-compacting concrete with a sufficient accuracy and in a reasonable amount of time. It was also pointed out, how crucial a correct value of the apparent slip is, to obtain the correct orientation of fibres.

5.6   Acknowledgements

Chapter 6

Conference paper 2

Title:	Fibre reinforced self-compacting concrete flow simulations in comparison with L-Box experiments using Carbopol
Authors:	O. Švec, J. Skoček, J. F. Olesen, H. Stang
Conference:	Proceedings of 8th Rilem International Symposium on Fibre reinforced concrete: Challenges and Opportunities, Guimaraes, 2012, RILEM Publications.

Abstract

An evolution of distribution and orientation of fibres in the fibre reinforced self-compacting concrete during the casting process is an important matter as the final orientation and distribution of fibres can significantly influence mechanical properties of the structural elements. A two-way coupled model for flow of suspension of rigid solid particles in a non-Newtonian fluid with a free surface has been developed for such a purpose and is shortly presented in this paper. Several experiments using an apparent yield stress fluid, i.e. Carbopol Ultrez 21 Polymer transparent gel, were conducted and analysed by means of digital image analysis. Orientation tensor fields coming from the digital image analysis were compared with the simulation to verify the ability of the model to properly represent the flow of the fibre reinforced self-compacting concrete.

6.1   Introduction

Knowledge of the final orientation and distribution of fibres is an important component in a proper understanding of the behaviour of cast structural elements. Self-compacting concrete is unfortunately not transparent which makes the experimental determination of the fibre orientation and distribution difficult. One approach in the determination of the fibre orientation might be to cast the structural element and retrieve a 3D image of the fibres using a CT scanning device Švec et al. (2012c). Another approach might be to cast the element, cut it into sections and visually count the number of fibres at the cross-section Sarmiento (2011). In this paper, we present yet another approach where we, similarly to Boulekbache et al. (2010), substituted the self-compacting concrete by suspension of fibres in transparent Carbopol Ultrez 21 Polymer (from now on called Carbopol) allowing a direct observation of fibres.

Experimental determination of the orientation and dispersion of fibres in the self-compacting concrete is a time and resource consuming procedure. A model capable of properly simulating the given problem is therefore desired. We have developed such a model and briefly introduce it in this paper. Finally we compare the resulting fibre orientation fields coming from the experiment with the fibre orientation fields coming from the simulation model. The orientation fields of fibres are represented by second order orientation tensor fields Advani and Tucker (1987).

6.2   Methods

In this section, we present the two-ways coupled model for the flow of suspensions of rigid solid particles in non-Newtonian fluid. The model consists of the fluid dynamics part used to predict the free surface flow of a homogeneous fluid solved using the Lattice Boltzmann method Sukop and Thorne (2005); Wolf-Gladrow (2000). The other part of the model predicts the time and space evolution of the solid particle suspension where dynamics of the solid particles is solved using Newton's classical equations of motion. Mutual interactions between the fluid and the solid particles are represented by means of the Immersed Boundary Method with direct forcing Feng and Michaelides (2005).

Due to the diversity of the individual methods, the overall model is separated into three distinct levels (see Figure 6.1):

a) **Level of fluid:** Flow of a non-Newtonian free surface fluid is solved at this level. The Lattice Boltzmann method is used as the fluid dynamics

solver whereas the Mass Tracking Algorithm describes the free surface of the flow. The Lattice Boltzmann method is spatially discretized into a square / cubic grid of Eulerian nodes (see square marks in Figure 6.1a). This level is influenced by the interaction forces coming from the "Level of fluid - solid particles interaction".

b) **Level of fluid - solid particles interaction:** This intermediate level provides a communication channel between the "Level of fluid" and the "Level of solid particles". The communication takes place via force interactions. We have used the Immersed boundary method with direct forcing to accommodate the communication between the two levels. Solid particles are discretized by a set of Lagrangian nodes at this level (see black circle marks in Figure 6.1b). No-slip boundary condition between the fluid and the solid particles is enforced at those Lagrangian nodes. To satisfy this condition, an interaction force is created and sent back to the "Level of fluid" and the "Level of solid particles".

c) **Level of solid particles:** Solid particles with an exact analytical geometry are used at this level (see Figure 6.1c). The dynamics of the solid particles is solved using Newton's equations of motion. Interactions among the solid particles and between the solid particles and the boundaries (such as walls etc.) are also solved at this level. A coefficient of restitution has been incorporated to account for elastic to plastic collisions and a Coulomb friction scheme to approximate the friction. Another force, which is applied onto the solid particles, comes from the "Level of fluid - solid particles interaction" to account for the interaction between the fluid and the solid particles.
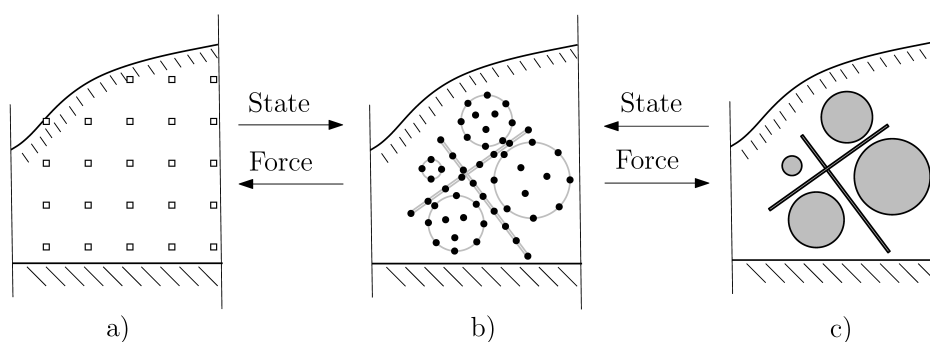
Figure 6.1: *Scheme of the model. a) Level of fluid. b) Level of fluid - solid particles interaction. c) Level of solid particles.*

6.3 Level of fluid

Level of fluid solves the flow of a homogeneous non-Newtonian free surface fluid, such as the self-compacting concrete and thus consists of the fluid dynamics and free surface solver.

6.3.1 Fluid Dynamics Solver

In contrast to the traditional computational fluid dynamics methods, where the problem is formulated by means of macroscopic quantities such as space and time dependent velocity and pressure fields, the Lattice Boltzmann method, with its roots in the kinetic theory of gases, treats the fluid as clouds of microscopic particles (e.g. molecules). Individual microscopic particles are assumed to be freely propagating through the space while instantaneously colliding among each other from time to time (see Lattice gas cellular automata Wolf-Gladrow (2000)). The clouds of particles are approximated by continuous particle distribution functions (i.e. probability of a particle occurrence). The particle distribution functions are further discretized by a set of discrete particle distributions to limit the number of unknowns. Lattice Boltzmann equation provides rules for mutual collisions and propagation of the particle distributions. The macroscopic quantities (density, velocity etc.) can then be computed as moments of the particle distributions.

The computational domain is typically discretized by a set of Eulerian cells of a uniform size (see Figure 6.1a). Continuous fields of macroscopic quantities (such as velocity fields) are then approximated by the mean values of the quantities in the discretized cells. Similarly, the time is discretized into uniform time steps.

In a given time step, the state of the fluid in a cell is fully described by the particle distributions in that cell. The particle distributions in the given time step at a certain position are computed from the particle distributions in neighbouring cells in the previous step. This accounts for the propagation of the particle distributions. Collisions of the particle distributions are in the simplest case approximated by a linear transformation of the particle distributions towards the local equilibrium state. Such a transformation is called Bhatnagar-Gross-Krook collision operator Chen and Doolen (1998). The local equilibrium state is based on the Maxwell-Boltzmann distribution, and is computed from the local macroscopic velocity and pressure (density) of the fluid. The difference between the current state of the particle distributions and the local equilibrium state allows for a simple approximation of the local shear rate and shear stress tensors Mei et al. (2002).

6.3.2 Free surface algorithm

A free surface has been implemented in the form of the Mass Tracking Algorithm Körner et al. (2005). The algorithm makes use of the same Eulerian discretized domain as the Lattice Boltzmann method where fluid, gas and interface cells are introduced. The Lattice Boltzmann equation is computed in the fluid and interface cells, only. Gas cells are empty cells where nothing is computed. Interface cells separate fluid phase and gas phase and are therefore responsible for a correct implementation of the free surface algorithm and for the correct mass conservation of the fluid. Interface cells are moreover the only place where the Mass Tracking Algorithm comes into play in the form of local mass tracking and reconstruction of missing information from the gas phase.

6.3.3 Level of fluid - solid particles interaction

The Immersed boundary method with direct forcing Feng and Michaelides (2005) provides a direct linkage between the "Level of fluid" and the "Level of solid particles". The fluid can "feel" the solid particles in the form of a force field. In the same manner, the solid particles can "feel" the fluid in the form of forces acting on the solid particles. At this level, the solid particles are discretized into a set of Lagrangian nodes. It is assumed that the velocity of a solid particle and the fluid at the same Lagrangian node are equal due to the no-slip boundary condition. Non-equal velocities are transformed into a force field acting on both the particle and the fluid. The force is in the simplest form computed based on Newton's second law of motion (i.e. such a force to accelerate a certain volume of the fluid that is surrounding the Lagrangian node to the velocity of the solid particle at that Lagrangian node). Since the Lagrangian nodes do not coincide with the Eulerian nodes coming from the "Level of fluid", the velocity of the fluid in the Lagrangian nodes is obtained by a volume averaging of the velocities at the Eulerian nodes. The volume averaging is conducted by means of a Dirac delta function Yang et al. (2009). The resulting forces are usually extrapolated from the Lagrangian nodes back to the Eulerian nodes (i.e. to the "Level of fluid") using the same Dirac delta function.

    The Immersed Boundary Method provides, contrary to other methods (e.g. bounce-back wall scheme Ladd (2006a,b)), smooth and stable time evolution of all the quantities (i.e. the position of the solid particles or forces acting on them). The most important feature of the Immersed Boundary Method, however, is its ability to simulate small objects of only a few lattice units or even sub-grid sized objects, see Švec et al. (2011). This results in a

significant reduction of the computational time needed.

6.3.4 Level of solid particles

At this level, the solid particles are assumed to be rigid bodies of a simple geometric shape (sphere, ellipsoid or cylinder) with the ability to move, rotate and interact among each other, with fluid, walls and other obstacles. The dynamics of those immersed solid particles is driven by Newton's second law of motion which is discretized with the explicit Runge-Kutta-Fehlberg time integration scheme with an adaptive time step. The numerical integration scheme that we adopted ensures the stability and accuracy of the simulation even for a highly non-linear behaviour. An accurate and robust treatment of interactions among the solid particles and between the solid particles and other obstacles such as walls or reinforcement plays an important role in a proper description of the relevant phenomena. The model includes two types of interactions, namely mutual instantaneous collisions of solid particles and continuous forcing of a general type. The instantaneous collisions were approximated by means of force impulses Švec et al. (2012b). An example of the continuous forcing could be a lubrication force correcting the fluid flow between two solid particles in the case when the two solid particles approach each other to a sub-grid distance Nguyen and Ladd (2002).

6.4   Applications

Verification of a newly developed model is a crucial part of its development phase. We presented a full description of our model and its basic verification in Švec et al. (2012b). A comparison of the model with a real-world casting of a fibre reinforced self-compacting concrete plate was given in Švec et al. (2012c). In this paper, we aim to compare the presented model with an L-Box experiment with the use of a transparent yield stress fluid, Carbopol.

6.4.1   Transparent L-Box experiment

In this experiment, we cast a suspension of stainless steel fibres in Carbopol into a form-work and visually study how the fibres orient and disperse due to the flow. We have chosen the L-Box form as a primary form-work of the study. Figure 6.2 shows the shape of the transparent plastic standard-sized L-Box both in the emptied and filled state.

As mentioned, we have used a gel-like fluid Carbopol which is a transparent shear thinning polymer with an apparent yield stress. It can further be
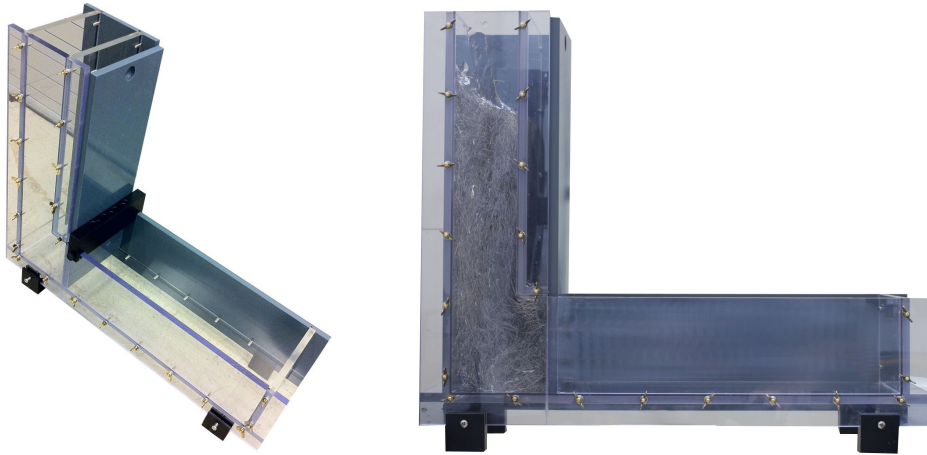
Figure 6.2: *Transparent L-Box form (see Section 6.4.2 for the dimensions and other parameters)*

assumed to follow a Bingham rheology model for shear rates between 0 and 5 s^{-1} Hvilsom and Rasmussen (2011). The two features, i.e. transparency and Bingham rheology, make Carbopol a suitable substitute for the fluid matrix in self-compacting concrete. Carbopol has, compared to the self-compacting concrete, a relatively low pH (ca 6.5). We have therefore used stainless steel fibres Dramix rl 80/30 sn produced by Bekaert Belgium to avoid any corrosion of the suspended fibres.

The Carbopol was produced according to the guidelines of the Lubrizol Company. We did not, however, succeed to avoid the creation of a large amount of air voids in the fluid. A desiccator was therefore used to produce a high under-pressure and thus to boil the air voids out of the fluid. We produced two different batches of the Carbopol fluid. One with the 0.125 volume percentage of Carbopol, the other one with double the amount of Carbopol in the fluid.

The resulting mean values of the plastic viscosity and the yield stress of the two batches were measured by Advanced Rheometer 2000 produced by TA Instruments, and read 5 Pa s, 8 Pa and 15 Pa s, 30 Pa, respectively. Although different values of the Bingham parameters were reached, the final shapes of the orientation ellipses of the fibres were very similar. We therefore present results of the first batch only. Each casting was done three times to account for the natural variance in results. Photographs of the final state of the three castings together with the orientation ellipses of the fibres are shown in Figure 6.3.

The orientation ellipses of the fibres serve as a visual representation of the
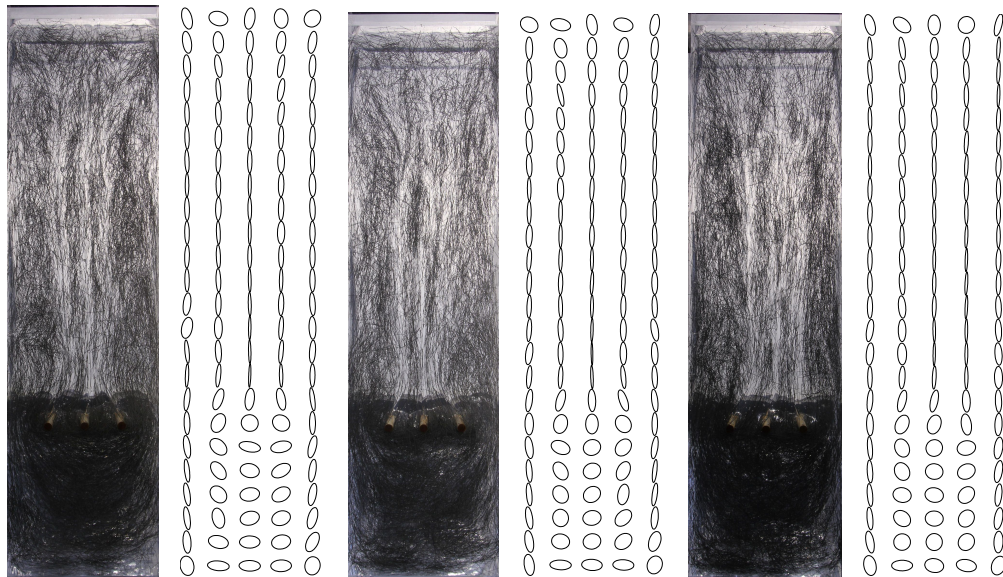
Figure 6.3*: Top view photographs of the final state of 3 experiments and their orientation ellipses.*

second order orientation tensors as described in Advani and Tucker (1987). The thinner the ellipses the more oriented fibres occur in the region. Vice versa, the circular ellipses stand for a random orientation of the fibres in the region.

To obtain the orientation ellipses, we took high resolution photographs of the final state of the flow (see Figure 6.3). The photographs were then transformed by Bradley local thresholding, adaptive smoothing and simple skeletonization technique to obtain a binary image (see AForge.NET framework). The binary image was then converted into the second order orientation tensors as described in Hvilsom and Rasmussen (2011) and visualized by orientation ellipses.

As can be seen in Figure 6.3, there are regions which are very complicated to analyse due to either spurious elements (e.g. horizontal bar in the upper part of the figure), decreased transparency of the form due to reinforcement mounting or due to high fibre volume concentrations. Resulting orientation ellipses should therefore be treated with caution, especially when compared to the ideal situation in the case of numerical simulations.

6.4.2   L-Box simulation

An L-Box simulation was run and the results of the simulation were compared to the experimental results. The initial and boundary conditions of

the simulation were as follows. The height, length and the width of the L-Box were 0.6 x 0.7 x 0.2 m. Three reinforcing bars of the diameter of 9 mm were placed into the L-Box. Spacing of the bars was 62 mm, 38 mm, 38 mm and 62 mm. The density, plastic viscosity and the yield stress of the fluid were set to 950 kg/m³, 5 Pa s and 8 Pa. A total amount of 0.5% volume fraction of the fibres was used in the simulation. Straight fibres of the length 6 cm, aspect ratio 80 and density 7500 kg/m³ were used. All the collisions of the fibres with the surrounding (fibres, walls, reinforcing bars) were assumed to be plastic, i.e. the coefficient of restitution was set to 0. Friction of the fibres was assumed to follow Coulomb friction model with the dynamic and static friction coefficient set to 0.3. The domain was spatially discretized by 1 cm = 3 lattice units. The fibre length was therefore 18 lattice units and the diameter was 0.225 lattice units. A correction term as described in Švec et al. (2011) was applied to adjust the force fields in the Immersed boundary method due to the sub-grid diameter of the fibres. A 3D view of the initial state, the top view of the final state and the top view of the orientation ellipses of the final state are presented in Figure 6.4.

Approximately 5 seconds of flow was simulated corresponding to ca 20 000 time steps. The number of fibres in the simulation was 21734. The simulation took ca 20 days on a single core 2 GHz CPU. Two thirds of the computation time was consumed by the "Level of solid particles" and the "Level of fluid -solid particles interaction". One third of the computation time was consumed by the "Level of fluid".

6.5   Results and discussion

We have developed a computational model capable of simulating a suspension of aggregates and fibres in the non-Newtonian free surface fluid. The model has recently been parallelized and is therefore presently capable of simulating ca 100 000 particles in a reasonable amount of time based on the computational power available. This makes the micro-, meso-up to macro-scale simulations possible. We have conducted an experimental work with a transparent yield stress fluid, Carbopol, and analysed the final states of the fibre orientation by means of orientation ellipses.

The comparison of the orientation ellipses coming from the experimental work and coming from the simulation indicates the ability of our model to correctly predict the final orientation of fibres in the fibre reinforced self-compacting concrete.
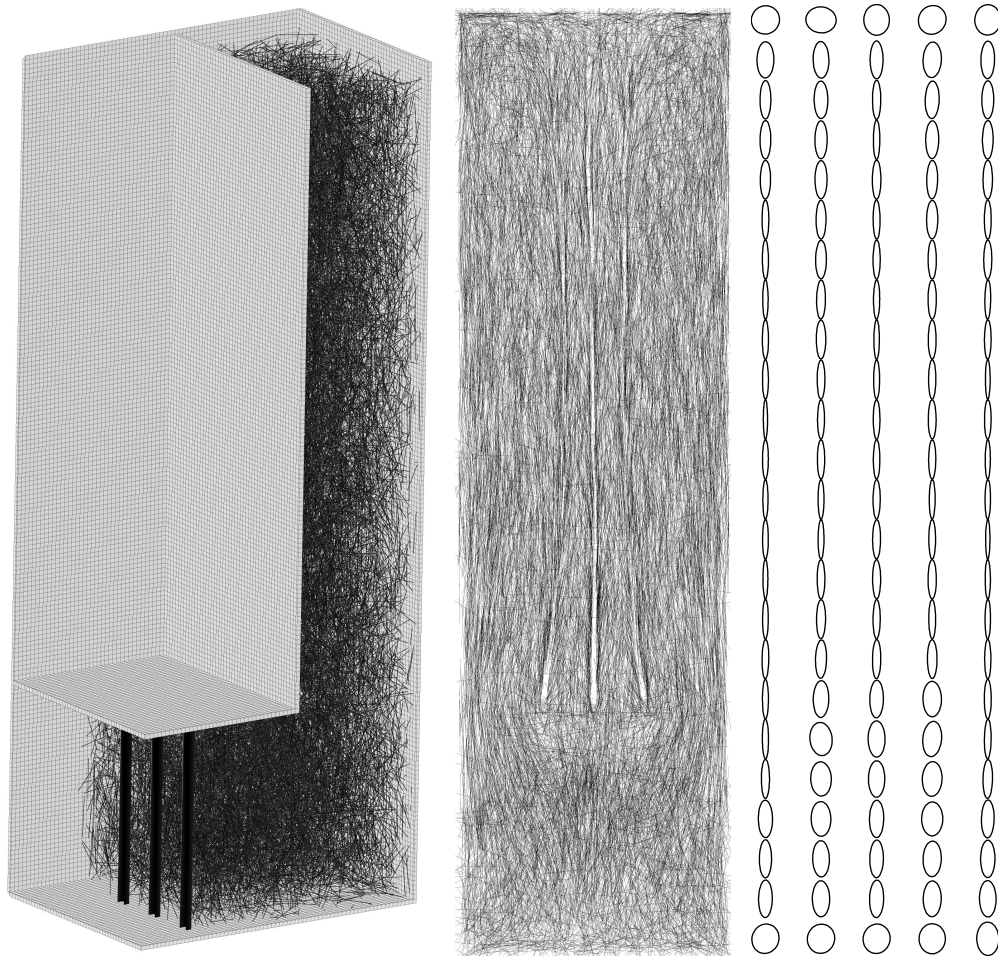
Figure 6.4: *3D section of the initial state of the simulation; Top view of the final state of the simulation and its orientation ellipses.*

6.6   Acknowledgements

Chapter 7

Journal paper 4

Title:	Influence of formwork surface on the orientation of steel fibres within self-compacting concrete and on the mechanical properties of cast structural elements
Authors:	Oldřich Švec, Giedrius Zirgulis, John E. Bolander, Henrik Stang
Published in:	Cement and Concrete Composites, Volume 50, July 2014, Pages 60-72, ISSN 0958-9465

Abstract

The influences of formwork surface on the final orientation of steel fibres immersed in self-compacting concrete and on the resulting mechanical response of the cast structural elements are investigated. Experimental observations of fibre orientation within cast slabs, obtained via computed tomography, indicate that fibres tend to orient according to the flow patterns during casting, but such tendencies are suppressed near rough formwork surfaces. Fibre orientation, in turn, affects the mechanical properties of the concrete as demonstrated by the load testing of beams extracted from the cast slabs. These processes and results are simulated using a computational fluid dynamics model of the casting process, in tandem with a lattice model of the fracture of the beam specimens. The computational fluid dynamics model determines the coordinates of each fibre within the concrete, which serve as input to the lattice model. Through comparisons with the experimental data, it is shown that these simulations correctly predict the phenomena of interest. We conclude the paper by highlighting a relationship between the

number and orientation of the immersed steel fibres crossing the fracture plane and the mechanical response of the structural elements.

7.1   Introduction

A growing portion of civil structures is nowadays constructed of self-compacting concrete. Contrary to ordinary concrete, self-compacting concrete flows and fills the formwork without any need of vibration or other type of agitation. Various forms of steel reinforcement, such as reinforcement bars, are typically used to improve the behaviour of concrete loaded in tension. It might be advantageous to replace the traditional reinforcement bars by steel fibres to achieve a simple execution of the structure, while improving tensile properties of the concrete. Orientation of immersed steel fibres evolve in response to the flow of the self-compacting concrete within the formwork (Stähli et al., 2007; Švec et al., 2012c). In particular, fibre orientations are affected by shear flow of the material and interactions with the formwork boundaries (Martinie and Roussel, 2011). The fibre orientation and thus properties of the structural elements can be then heavily dependent on the material rheology and the methods of element casting (Stähli et al., 2007; Ferrara et al., 2008).

Concrete is a multiphase material consisting of cement paste, fine and coarse aggregates, and possibly fibres. Due to the geometrical constraint imposed by a solid boundary on particle packing near the boundary, the distribution of immersed particles (aggregates, fibres, etc.) in that region becomes non-uniform, which results in the so-called wall effect (Figure 7.1a). The wall effect thus expresses the fact that the macroscopic properties of the fluid (density, viscosity, etc.) in the bulk of the material and at the boundary layers are different.
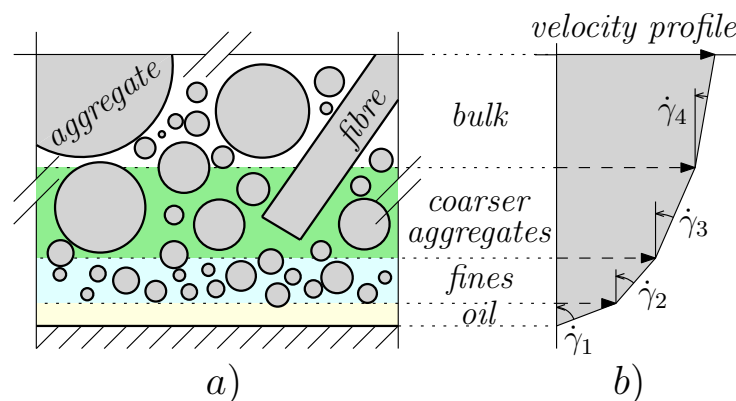
Figure 7.1: *a) Material composition of a typical cross-section of fibre reinforced concrete in the vicinity of formwork. b) Flow velocities and shear rates of the individual layers.*

Figure 7.1a, as an example, depicts composition of four different layers of flowing concrete near an oiled formwork surface. The four layers represent the oil layer, layer with fines, layer with coarser aggregates and the bulk layer. The existence of the layered structure is a consequence of the aforementioned wall effect. Figure 7.1b illustrates a velocity profile of the cross-section of the flowing concrete. The velocity profile depends on shear rates of the four individual layers, $\dot{\gamma}_{1-4}$. It is likely that the velocity profile in the vicinity of the formwork has a direct impact on the resulting orientation of the immersed steel fibres and consequently on the resulting mechanical response of the material.

The wall effect, together with various types of formwork characterized by different roughness and treatment, contribute to uncertainties in the behaviour of structures made of fibre reinforced self-compacting concrete. Especially for thin elements, the flow of the material and consequently the mechanical response of the elements is significantly influenced by the formwork - fluid interaction.

In the field of fibre reinforced self-compacting concrete, several authors discuss the influence of casting process on the orientation of steel fibres (Martinie and Roussel, 2011; Liu et al., 2012; Laranjeira et al., 2012; Kulasegaram and Karihaloo, 2013). Others study the impact of fibre orientation on the mechanical response of the structural elements (Stähli et al., 2007; Boulekbache et al., 2010; Ferrara et al., 2011; Zerbino et al., 2012). Jacobsen et al. (Jacobsen et al., 2009) addresses the impact of the formwork surface on the pumpability of an ordinary concrete.

The presented paper merges all the problems into one by studying the influence of the formwork surface on the flow pattern of steel fibre reinforced self-compacting concrete close to the formwork. The paper further studies the influence of the final orientation of steel fibres on the resulting mechanical properties of the material. The study is carried out through the combined use of physical experiments and numerical modelling. The experimental study was performed by means of tomographic imaging of slab specimens cast with fibre reinforced self-compacting concrete and by means of three-and four-point bending tests of specimens cut from the slabs. The numerical study was conducted by means of two distinct numerical simulations developed by the authors: 1) a computational fluid dynamics based procedure to simulate fibre movement during the casting process, including fluid-structure interactions at the formwork boundaries; and 2) a lattice model of material elasticity and fracture, including the explicit representation of individual fibres within the specimen volumes. Fibre coordinates determined through the computational fluid dynamics based simulation served as direct input to the lattice modelling of the flexural test specimens.

Materials and methods of the presented study are fully described in Section 7.2. The casting process and the data analysis process of the experimental study are explained in Section 7.2.1. The two distinct numerical simulations are introduced in Section 7.2.2. Section 7.3 presents all the experimentally and numerically obtained results related to the orientation of steel fibres and related to the mechanical properties of the material. The aforementioned results are linked together in Section 7.3.3. Discussion of the results is provided in Section 7.4. Section 7.5 concludes the article.

7.2 Materials and methods

The following subsections describe experiments that were conducted to verify the hypothesis that formwork surface can influence the orientation of fibres immersed in self-compacting concrete and, consequently, the mechanical response of the structure. The numerical simulations, which were used to strengthen and complement the experimental observations, are also briefly introduced.

7.2.1 Experiments

Six slabs of fibre reinforced self-compacting concrete were cast using formwork of three different surface types. The following subsections describe the casting process of the slabs, methods for quantifying the orientations of fibres immersed in the slabs, and the subsequent mechanical testing of beam specimens cut from the slabs. Further information about the experimental set-up can be found in Žirgulis et al. (2013b).

Mixture design and casting process

Six slabs of dimensions $1.2\,\text{m} \times 1.2\,\text{m} \times 0.15\,\text{m}$ were cast of fibre reinforced self-compacting concrete. The casting process was conducted from a rubber pipe inlet positioned near one of the corners of the slab (Figure 7.2). The point of discharge was located at $0.2\,\text{m}$ above the base of the slab.

Mixture design of the self-compacting concrete was: cement $= 388\,\text{kg/m}^3$, silica fume $= 19.4\,\text{kg/m}^3$, natural sand $(0-8\,\text{mm}) = 1182\,\text{kg/m}^3$, crushed stone $(8-16\,\text{mm}) = 570\,\text{kg/m}^3$, super plasticiser $= 4.66\,\text{kg/m}^3$ and air entrainer $(1{:}7) = 0.97\,\text{kg/m}^3$. The water cement ratio was 0.505. At the time of mixing, the fine and coarse aggregates were in the saturated-surface-dry condition.

Hooked end steel fibres (Bekaert Dramix RL 80/60 BN) were gradually added to the self-compacting concrete during the mixing process. The fibre
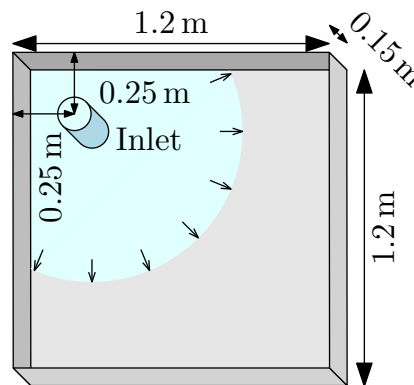
Figure 7.2: *Slab casting with fibre reinforced self-compacting concrete supplied by a rubber pipe inlet.*

volume ratio was 0.5%, corresponding to $40\,\text{kg/m}^3$. The fibre length and the fibre diameter were $60\,\text{mm}$ and $0.75\,\text{mm}$, respectively. Density of the steel fibres was $7850\,\text{kg/m}^3$.

Three different formwork surfaces were employed in the experiment, as shown in Figure 7.3. Two slabs were cast for each formwork surface, providing a total of six cast slabs. All the formwork surfaces were primed with a thin layer of a form oil to simplify the demolding process. Details of the casting process can be observed in the attached video[1], which shows the casting of the fibre reinforced self-compacting concrete into the glue-laminated plywood formwork, ordinary plywood formwork and into the glued-sand plywood formwork.
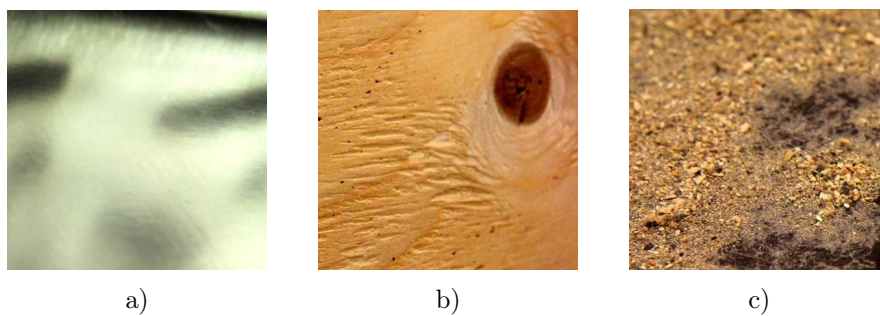
Figure 7.3: *Typical surface views of three different formwork types. a) Glue-laminated plywood. b) Ordinary plywood. c) Glued-sand plywood.*

Rheology of the fresh fibre reinforced self-compacting concrete was eval-

---

[1] Double-click here to view or save the video. Format of the video is MP4/H264.

uated during the casting process by means of the standardized slump flow test according to EN 12350-2. Spread of the slump was measured and read 620 mm. Rheological parameters, following a Bingham plastic rheological model, were obtained by means of 4C-Rheometer (Thrane et al., 2010). Yield stress and plastic viscosity of the fibre reinforced self-compacting concrete were estimated to be 22 Pa and 75 Pa s, respectively. The measured density and air content of the fresh concrete were 2318 kg/m³ and 3.5 %, respectively.

After casting, the slabs were covered with cloth saturated with water. The slabs were then sealed within a polyethylene film and left to harden for a period of 28 days at ambient temperatures. In total six beam specimens of dimensions 0.6 m × 0.15 m × 0.15 m were then cut out from each of the slabs, as indicated by the red and green prisms in Figure 7.4.
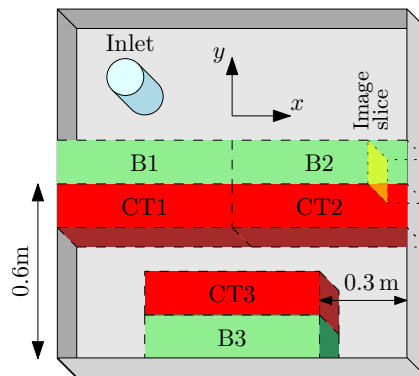
Figure 7.4: *Layout of the beam specimens cut out of the cast slabs.*

Orientation of the steel fibres present in the beams specimens was studied by means of the computed tomography and subsequent image analysis. The resulting mechanical response of the beam specimens was studied by means of the three-and four-point bending tests.

Computed tomography and image analysis

Computed Tomography (CT) is an advanced radiographic technique for obtaining 3D images of the internal structure of an element. The method has been among others widely used in the field of steel fibre reinforced concrete Stähli et al. (2007); Barnett et al. (2009); Oliveira (2010); Suuronen et al. (2012). The CT and subsequent image analyses were employed to obtain a 3D representation of the steel fibres located in the beam specimens. The 3D representation was subsequently approximated by a set of 3D orientation tensors (Advani and Tucker, 1987).

We used a former medical CT scanner, Siemens Somatom Sensation 4, to scan three beam specimens out of each slab. The three scanned beam specimens are depicted in Figure 7.4 as red prisms. Sequential spine routine of the medical CT scanner was employed to interpret approximately 600 successive slices normal to the x axis (Figure 7.4). A typical slice image produced by the CT scanner is presented in Figure 7.5. The red regions in Figure 7.5b are the voxels with maximum brightness. The red regions were obtained by thresholding the image. The zone marked by the green rectangle in Figure 7.5b reveals that not only fibres but also parts of aggregates are marked in red. This is caused by a relatively low tube voltage of the medical CT scanner and results in a more complicated image analysis.

a)   b)
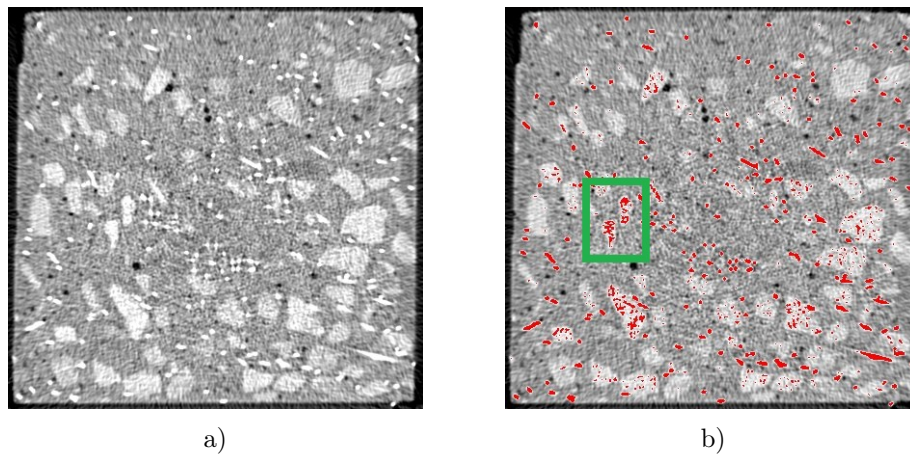
Figure 7.5: *a) A typical slice image of the scanned beam specimens. b) Regions with the maximum brightness.*

An open-source application Fiji[2] was used to crop, threshold and skeletonize the sequence of the approximately 600 successive slice images. The skeletonization technique of the Fiji application outputted a skeleton, i.e. a large set of 3D line segments located in space. Figure 7.6 as an example shows a small part of the skeleton.

Red region in Figure 7.6 shows 3D line segments that were probably created by skeletonizing aggregates depicted in Figure 7.5b. Figure 7.6 reveals that although the majority of the 3D line segments represent individual parts of steel fibres, some of the 3D line segments represent other concrete constituents such as aggregates. The primary interest of the paper is to study orientation of steel fibres. The 3D line segments were therefore converted into a set of second-order orientation tensors (Advani and Tucker, 1987). The sec-

---

[2]http://fiji.sc/
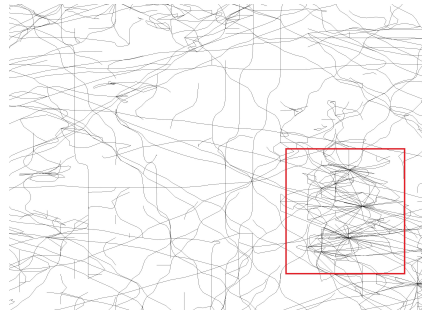
Figure 7.6: *Result of the skeletonization technique of the CT images. Black lines are the individual 3D line segments.*

ond-order tensors can be visualized by means of 3D ellipsoids in space or by means of 2D ellipses in plane.
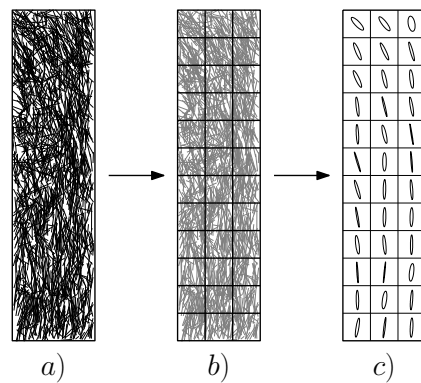
Figure 7.7: *Process for obtaining the second-order orientation tensors: a) skeleton image of fibres within beam specimen; b) volumetric discretization into cubic regions; and c) second-order tensor representation of fibre orientation within each cubic region.*

All the CT scanned beam specimens were volumetrically split into a series of cubic regions (see Figure 7.7b for a 2D projection). Second-order orientation tensors were computed for all the 3D line segments located in each of the cubic regions. Figure 7.7c illustrates the second-order tensors by projecting the 3D orientation ellipsoids into 2D orientation ellipses. The second-order orientation tensors can be computed as (Advani and Tucker, 1987):

$$a_{ij} = \frac{1}{L_t} \begin{bmatrix} \sum L \, p_x \, p_x & \sum L \, p_x \, p_y & \sum L \, p_x \, p_z \\ & \sum L \, p_y \, p_y & \sum L \, p_y \, p_z \\ \text{sym.} & & \sum L \, p_z \, p_z \end{bmatrix} , \qquad (7.1)$$

where the summation is taken through all the line segments located in the cubic region of interest. Values of p_x, p_y and p_z are components of the normalized vector pointing in the direction of the individual line segments located in the cubic region of interest. Value of L is the length of the individual line segments whereas L_t is the total length of the line segments located in the cubic region of interest, $L_t = \sum L$.

The summation of the main diagonal of the orientation tensor must be equal to unity, i.e., $a_{1,1} + a_{2,2} + a_{3,3} = 1$. Half lengths and directions of the axes of the orientation ellipsoids are defined as eigenvalues and eigenvectors of the second-order orientation tensors, respectively. Results of the computed tomography analysis are presented in Section 7.3.1.

Three- and four-point bending tests

All the six beam specimens indicated in Figure 7.4 were tested to obtain their mechanical response in flexure. The beam specimens depicted by green prisms in Figure 7.4 were tested in four-point bending according to the *Norwegian sawn beam test* (NSBT) (Sandbakk, 2011). After the CT scanning, as presented in Section 7.2.1, the beam specimens depicted as red prisms in Figure 7.4 were saw cut to provide a notch at mid-span and tested in three-point bending according to EN 14651. During the test, the beam specimens were oriented in the casting direction, such that the tensile face was the bottom cast surface of the beam which deviates from the EN 14651. Figure 7.8 depicts a typical fracture pattern for each type of bending test.
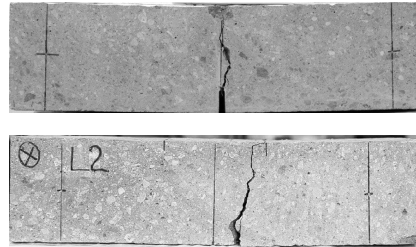
Figure 7.8: *A typical frontal view of the fractured beam specimens. Top: three-point bending test. Bottom: four-point bending test.*

The three-point bending test results were recorded in terms of load, F, and corresponding crack mouth opening displacement, $CMOD$. For the four-point bending tests, load and respective midspan deflections of the beam specimens, δ_m, were recorded. For the purpose of comparing results of the different types of beam tests, an effective $CMOD$ for the case of four-point bending was computed based on Sandbakk (2011) as

$$cmod_{4pt} = \frac{4\,h\,\delta_m}{l_{4pt}} \; ,$$ (7.2)

where h ($= 0.15\,\mathrm{m}$) is the height of the beam specimen and l_{4pt} ($= 0.45\,\mathrm{m}$) is the distance between the beam supports.

In the case of the three-point bending tests, the flexural stresses of beam specimens were computed as Kanstad et al. (2011)

$$\sigma_{3pt} = \frac{3\,F\,l_{3pt}}{2\,b\,h_{sp}^2} \; ,$$ (7.3)

where b ($= 0.15\,\mathrm{m}$) is the width of the beam specimen and h_{sp} ($= 0.125\,\mathrm{m}$) is the distance between tip of the notch and top of cross section (Vandewalle, 2000). Value of l_{3pt} ($= 0.5\,\mathrm{m}$) stands for the span between the beam supports.

In the case of the four-point bending tests, the flexural stress of a beam specimen was computed as

$$\sigma_{4pt} = \frac{F\,l_{4pt}}{b\,h^2} \; .$$ (7.4)

Results of the three-and four-point bending tests are presented in Section 7.3.2.

Fibre count local to the fracture plane

Section 7.2.1 described the process of scanning of the beam specimens depicted by red prisms in Figure 7.4. For each 3D image of the beam specimens produced by CT scanning, we selected the image slice located closest to the fracture plane. The number of steel fibres crossing the fracture plane was estimated by manually counting the fibres visible on the slice images similarly to Zerbino et al. (2012); Žirgulis et al. (2013b); Wuest and Denarié (2009); Liu et al. (2011).

In addition, all the beam specimens tested by the three-and four-point bending tests were cut in the vicinity of the main crack. The cut plane was polished and the number of steel fibres visible at the cut plane was manually counted. The number of steel fibres crossing the fracture plane or the cut

plane was related to the flexural stresses of the individual beam specimens at an arbitrarily chosen crack mouth opening displacement, as will be presented in Section 7.3.3.

7.2.2 Numerical simulations

Two distinct types of numerical simulation were run to strengthen the experimental observations and to shed light on the phenomenological processes observed in the experiments. The first type simulates the flow of the fibre reinforced self-compacting concrete. Using fibre coordinate data from the flow simulations, the second type simulates the fracture behaviour of the hardened fibre reinforced self-compacting concrete.

Numerical simulation of flow

In recent years there have been growing fundamental and practical interests in numerically simulating the flow of concrete materials, including fibre reinforced concrete (Kang and Kim, 2012). Roussel et al. (Roussel et al., 2007) review the advantages and disadvantages of several strategies for simulating concrete flow. We have developed a numerical framework capable of predicting flow of explicitly represented rigid particles immersed in the free surface flow of a homogeneous non-Newtonian fluid, such as fresh concrete. One of the primary goals of the numerical framework has been to quantitatively predict the distribution and orientation of the steel fibres immersed in the self-compacting concrete during casting. The numerical framework is explained in detail in Švec et al. (2012b). We discussed the implementation of the immersed rigid fibres into the framework in Švec and Skoček (2013a). The ability of the numerical framework to properly simulate various formwork surfaces was introduced in Švec and Skoček (2013b).

Figure 7.9 presents a 3D view of the numerical simulation of slab casting at an intermediate step. The numerical simulation was run with the same physical input parameters (fluid density, yield stress plastic viscosity, fibre type etc.) as presented in Section 7.2.1. The numerical framework is devoid of any non-physical input parameters. The self-compacting concrete was modelled as a free surface flow of a homogeneous Bingham plastic fluid. The steel fibres were modelled as thin rigid cylinders immersed in the homogeneous fluid. The steel fibres were modelled explicitly, one by one, including various features of the numerical framework such as the two-way coupled interaction between the fluid and the fibres, plastic collisions among the fibres or plastic collisions of the fibres with the formwork. The formwork was modelled as Navier's slip boundary condition of a specific Navier's slip

length (Švec and Skoček, 2013b). The fluid domain was discretized as $1\,\mathrm{cm}$ = 1 discrete unit.
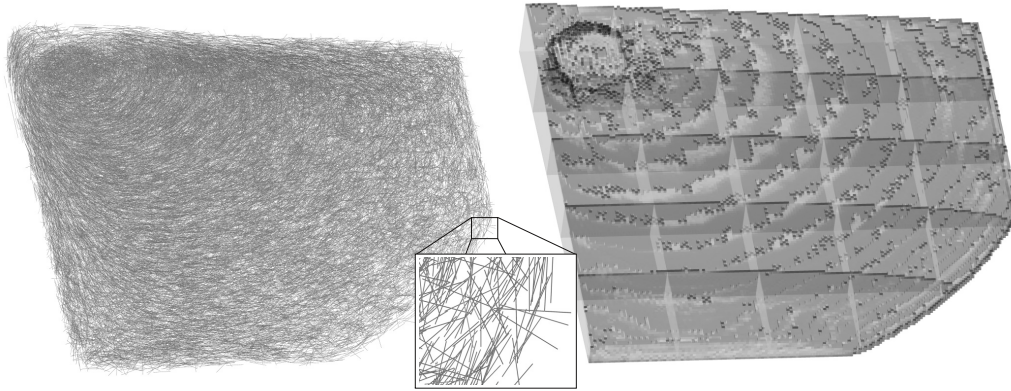
Figure 7.9: *3D view of the simulated slab casting at an intermediate step. Left: immersed steel fibres; Right: Bingham plastic fluid.*

In total three different numerical simulations were run differentiated by the type of the formwork surface used in the numerical simulation. The three different Navier's slip lengths were then equal to $0\,\mathrm{cm}$, $8\,\mathrm{cm}$ and ∞.

Each numerical simulation was run in parallel on 25 computer cores and lasted approximately 4 days. The peak number of explicitly simulated steel fibres was approximately 41 000.

Results of the numerical simulation of flow are presented in Section 7.3.1.

Numerical simulation of fracture behaviour

A lattice-type model is used to simulate the fracture behaviour of the fibre-reinforced concrete. Both the matrix and fibre element formulations are based on the concept of a rigid-body-spring model, as described in previous publications (Li et al., 2006; Bolander et al., 2008; Asahina et al., 2011). The concrete matrix is assumed to be homogeneous and exhibit bilinear softening after fracture. Material disorder is solely due to the presence of the short-fibre reinforcement, which is explicitly represented within the model framework. Domain discretization is based on the Delaunay/Voronoi tessellation of a set of nodes (Okabe et al., 2000). Discretization of the fibre-reinforced concrete specimens is presented in Figure 7.10a.

Stiffness contributions of the fibres before concrete cracking are derived from elastic shear lag theory. After concrete cracking, fibre contributions to strength and stiffness across the open crack account for debonding and

slip at the fibre-matrix interface. The effect of the hooked end of the fibres
was approximated as a frictional force, distributed uniformly over the fibre
embedded length. The pullout behaviour of individual fibres was modified to
account for snubbing effect and the potential for matrix spalling when fibres
are lowly inclined to the fracture plane (Lee et al., 2010).
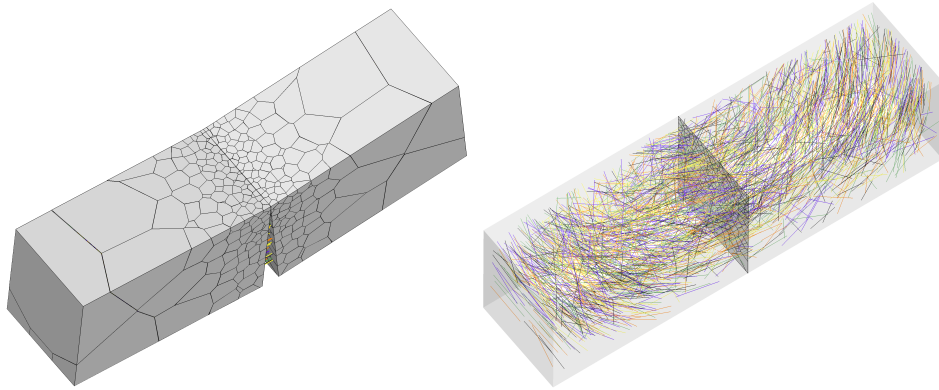
Figure 7.10: *a) Discretization of four-point bend specimen under loading;
and b) fibres within the computational domain for specimen B1a (for the case
of glue-laminated plywood as formwork)*

The lattice model was used to simulate fracture behaviour of each of the
four-point bend tests (B1a, B2a, and B3a) for the case of glue-laminated
plywood as formwork. This case exhibited the largest variation in load-
displacement behaviour with respect to beam position in the slab.

The final positions of the steel fibres within the cast slab specimens were
supplied by the aforementioned numerical simulations of flow. Thereafter,
the slabs were sectioned to produce models of the beam specimens, as shown
in Figure 7.4, in a way that mimicked the physical cutting process. Fibres
intersecting the cut planes were cut at the point of intersection, retaining the
portion inside the beam volume. Figure 7.10b as an example illustrates steel
fibres present in one of the tested beam specimens.

Fracture of the beam specimens was restricted to occur along the central
plane within the beam span (see Figure 7.10). This simplification allows for
the grading of nodal point density in the vicinity of the crack plane to reduce
computational expense. As discussed later, however, restricting the location
of cracking can affect the mechanical response of the beams.

Tensile strength of the matrix and the pullout resistance of individual
fibres were adjusted to achieve rough agreement between the load-displace-
ment curve of the model and that of the B1a specimen. The following settings
were used as a result of the calibration process: uniaxial tensile strength $\sigma_t =$

2 MPa; $\sigma_1 = \sigma_t/4$; $w_1 = 0.05$ mm; traction-free crack opening displacement $w_c = 0.3$ mm; and frictional resistance $\tau_f = 4$ MPa Bolander et al. (2008). The same parameter set was then used for the simulations of specimens B2a and B3a. The results for specimens B2a and B3a can be therefore viewed as predictive simulations.

The assumptions made herein, including the fitting of parameter values for the B1a specimen, were deemed reasonable for achieving the primary goal of the fracture simulations, which is to demonstrate the effects of fibre distribution on the fracture behaviour of the flexural specimens. Results of the numerical simulation of fracture behaviour are presented in Section 7.3.2.

7.3 Results

This section presents results obtained by CT scanning and by the three-and four-point bending tests. These experimental results are then compared to results obtained from their respective numerical simulations.

7.3.1 Fibre orientation

The following two subsections study the average planar (x-y) orientation of the steel fibres by means of the second-order orientation tensors. Comparisons are made between the orientation of the steel fibres obtained by experiments and the results obtained by the numerical simulations that we developed.

Computed tomography and image analysis

Figure 7.11 presents projected top views of the orientation ellipsoids for the bottom half of the CT scanned beam specimens for the different formwork surfaces. The positions of the beam specimens (CT1, CT2, CT3) within the cast slabs are indicated in Figure 7.4.

Figures 7.11a and 7.11b indicate that the ordinary plywood formwork and the glued-sand plywood formwork provide similar orientations of the immersed steel fibres in the bottom half of the slabs. Steel fibres in the bulk of beam specimens CT1 and CT2 seem to be more or less randomly oriented as there is no prevailing pattern of the orientation ellipses. The steel fibres become fairly oriented along the y coordinate at the bottom and top edges of the beam specimens CT1 and CT2, respectively. This is caused by the wall-effect induced by the vertical parts of the formwork. Beam specimens CT3 of Figures 7.11a and 7.11b reveal a slight degree of orientation of the steel fibres along the x coordinate.
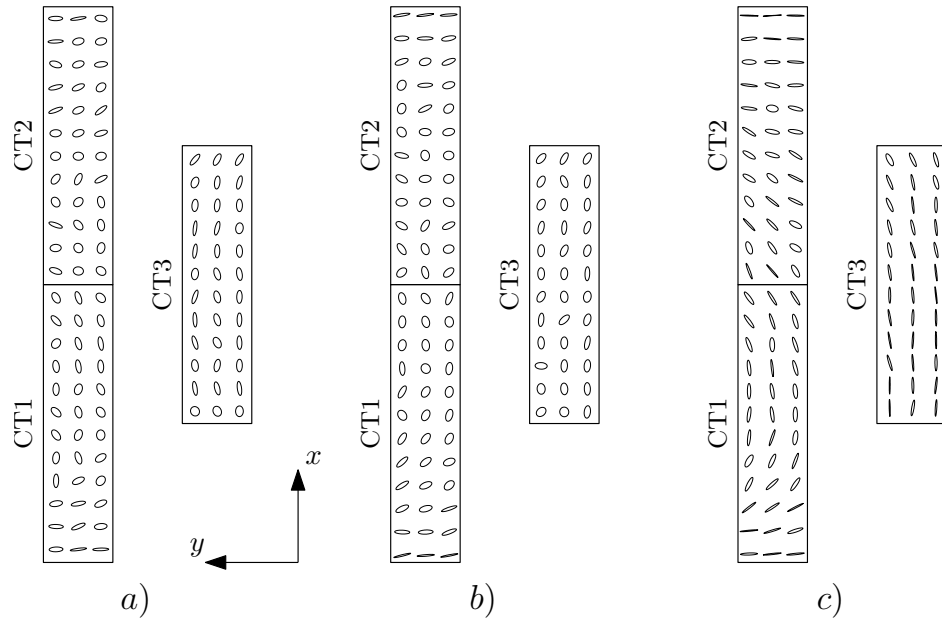
Figure 7.11: *Top view projection of the CT-based orientation ellipsoids for the bottom half of the slabs. a) Ordinary plywood formwork. b) Glued-sand plywood formwork. c) Glue-laminated plywood formwork*

By observing Figures 7.11a and 7.11b, we can conclude that the ordinary plywood formwork and the glued-sand plywood formwork possess similar apparent slip characteristics. At the bottom half of the slabs, the rough surface of the formwork seems to result in fibre orientations that are more or less independent of the flow pattern.

Figure 7.11c on the other hand shows a completely different pattern of the orientation of the steel fibres. The observation suggests that, within the bottom half of the slab, the fibres tend to orient under the flow of the self-compacting concrete when a smooth-surface formwork such as glue-laminated plywood is applied.

Figure 7.12 presents the experimentally obtained orientation of the steel fibres for the upper half of the slabs for the three formwork surfaces. Contrary to Figure 7.11, all results indicate a similar pattern in which fibres seem to be oriented according to the flow of the self-compacting concrete. Figure 7.12c indicates a slightly higher degree of the orientation of the steel fibres compared to those of Figures 7.12a and 7.12b but the difference is much less pronounced than for the case of the bottom half of the slabs.
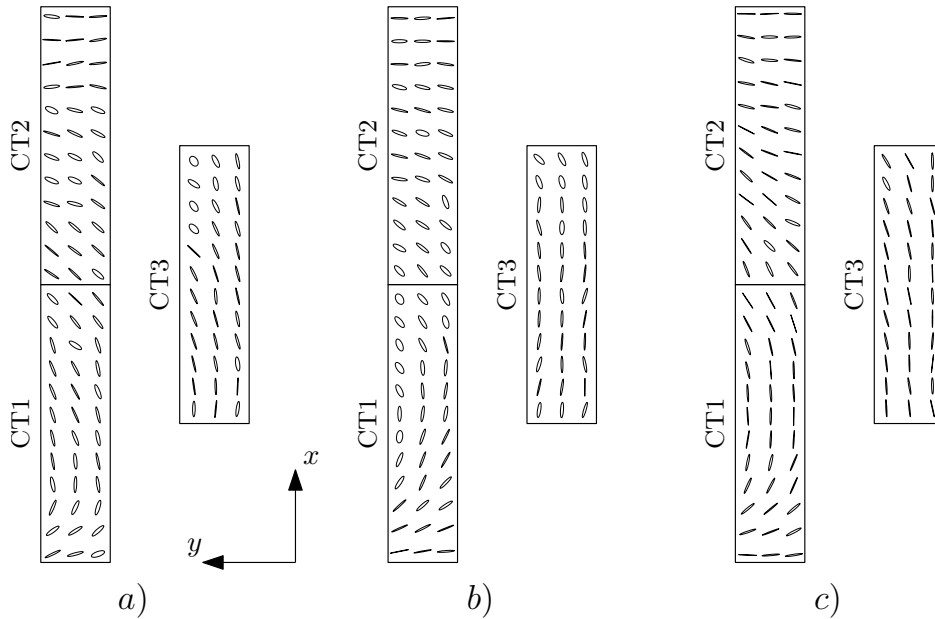
Figure 7.12: *Top view projection of the CT-based orientation ellipsoids for the upper half of the slabs. a) Ordinary plywood formwork. b) Glued-sand plywood formwork. c) Glue-laminated plywood formwork*

Numerical simulation of flow

The casting process of the slabs of the three formwork surfaces was simulated by means of the numerical framework that we developed and have described in Švec et al. (2012b); Švec and Skoček (2013a,b). The formwork of the cast slabs was modelled using Navier's slip boundary condition. Numerical simulations were run for Navier's slip lengths of $0\,\mathrm{cm}$, $8\,\mathrm{cm}$ and ∞. The numerically obtained orientation of the steel fibres was subsequently compared to the experimental results presented in Section 7.3.1.

Figure 7.13 shows the resulting orientation of the steel fibres for the slab with Navier's slip length equal to $0\,\mathrm{cm}$. The orientation of the steel fibres is depicted as the top view projection of the orientation ellipsoids (marked with black stroke). Within the bottom half of the slab (Figure 7.13a), the steel fibres tend to orient in the regions close to the vertical walls of the formwork, which is primarily caused by the wall effect. In the bulk of the slab, the steel fibres remain in a more or less random orientation state. In the upper half of the slab (Figure 7.13b), the steel fibres exhibit a relatively high degree of orientation following the flow pattern of the self-compacting concrete.

Figure 7.13 also compares the simulated fibre orientations with the exper-

a)   b)
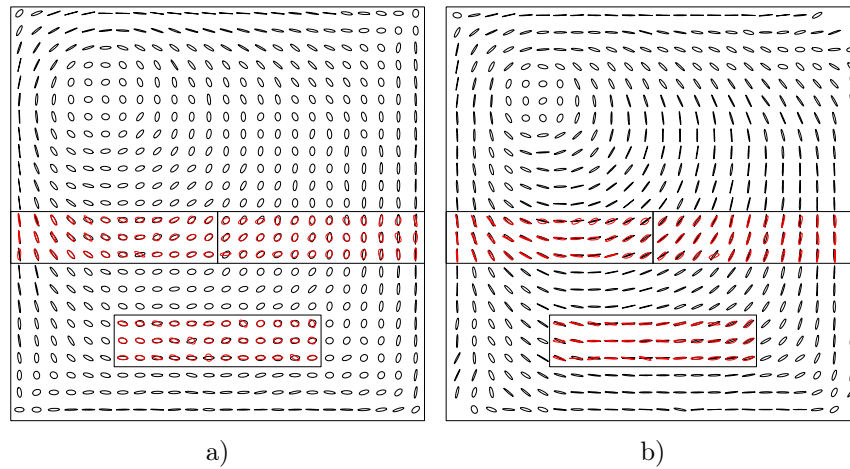
Figure 7.13: *Comparison of the simulated fibre orientations (black stroke) for slip length* 0 cm *with the CT-based results (red stroke) for the case of glued-sand plywood formwork. (a) bottom half. (b) upper half of slab.*

imentally measured orientations for the bottom and upper halfs of the slab. The comparison indicates a relatively high degree of agreement between the experimentally and numerically obtained results. The comparison indicates that glued-sand plywood formwork or formworks of similar roughness can be successfully modelled using the Navier's slip boundary condition with a slip length of 0 cm.

Figure 7.14 presents the simulated fibre orientations for the slab with Navier's slip length equal to 8 cm. In the bulk of the bottom half of the slab (Figure 7.14a), the steel fibres seem to orient to a higher degree compared to the slab with slip length equal to 0 cm (see Figure 7.13a). The steel fibres of the upper half of the slab exhibit a high degree of orientation, following the flow pattern of the self-compacting concrete. The results of the numerical simulation agree well with the experimental (CT) results for the slab having the glue-laminated plywood as the formwork (Figure 7.14).

Figure 7.15 presents the orientation of the steel fibres for the extreme case of the Navier's slip length equal to ∞. In such a case the steel fibres exhibit a high degree of orientation in all the parts of the slab, except for immediately under the inlet pipe. There were no respective experimental results for comparison with these numerical results.
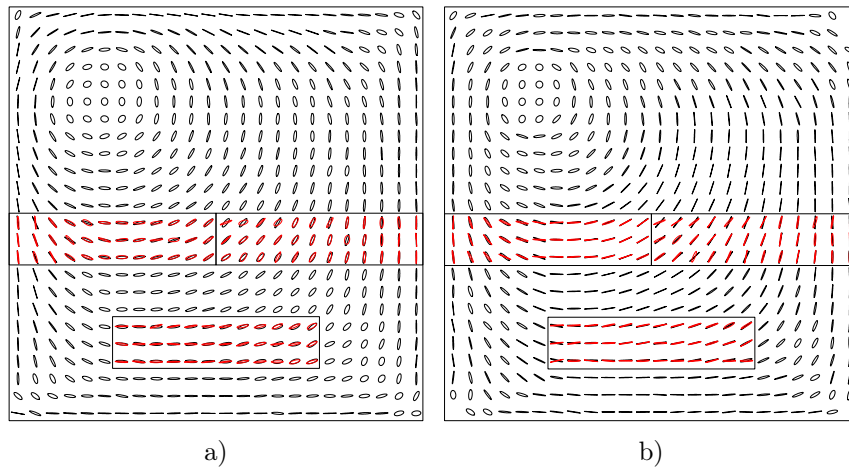
Figure 7.14: *Comparison of the simulated fibre orientations (black stroke) for slip length* 8 cm *with the CT-based results (red stroke) for the case of glue-laminated plywood formwork. (a) bottom half. (b) upper half of slab.*

7.3.2 Mechanical properties

This subsection illustrates the influence of the formwork surface on the mechanical properties of the fibre reinforced self-compacting concrete material. Results of the three-and four-point bending tests are presented. For the case of glue-laminated plywood formwork, tested under four-point bending, the experimental results are compared to those of the lattice model simulations.

Three- and four-point bending tests

Figures 7.16, 7.17 and 7.18 present mechanical responses of the beam specimens for the three different formwork surfaces in terms of load-displacement curves. Two nominally identical slabs were cast for each formwork surface type and, therefore, two flexural test results are provided for each case. Individual plots thus contain results of two beam specimens of the same origin, e.g. B1,a and B1,b.

    Figure 7.16 indicates a substantial difference in the flexural behaviour of the individual beam specimens, ranging from deflection hardening to almost complete loss of residual strength after first cracking. For example, beam specimens marked CT3 and B3 experience more than $5\times$ and $10\times$ higher post-cracking strengths compared to beam specimens CT1 and B1, respectively. The observations suggest that, when using a smooth-surface formwork, structural elements extracted from different locations can possess considerably diverse mechanical properties.
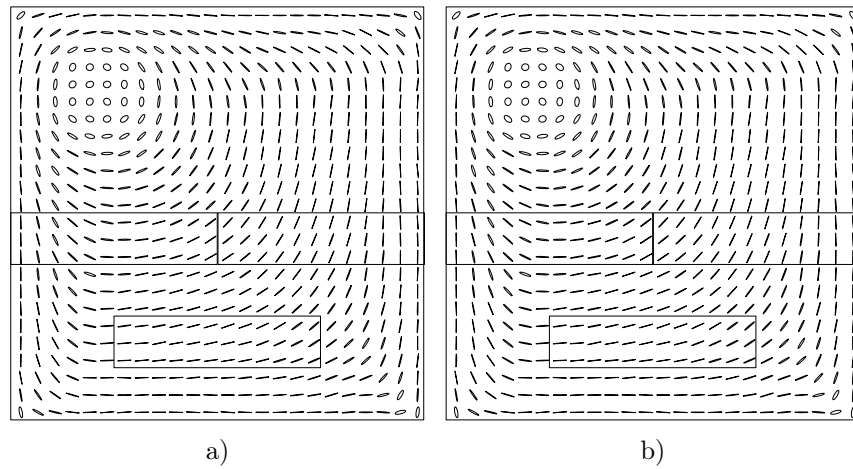
Figure 7.15: Results of the simulated fibre orientations for slip length ∞. (a) bottom half. (b) upper half of slab.

a) three-point bending test   b) four-point bending test
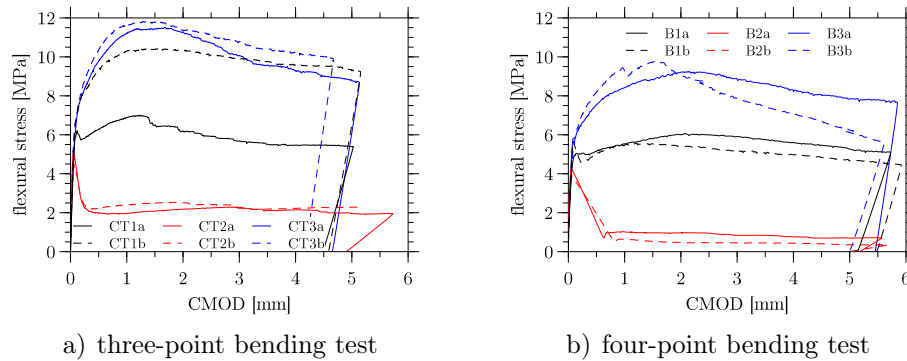
Figure 7.16: Response of the beam specimens extracted from slabs having glue-laminated plywood as the formwork.

Figures 7.17 and 7.18 on the other hand indicate a significantly lower spread of the flexural stresses of the individual beam specimens. The highest post-cracking strength of the beam specimens is approximately $2\times$ higher compared to the lowest mechanical response of the beam specimens. Structural elements cast into formwork with a rough surface generally seem to result in considerably less diverse mechanical properties compared to the structural elements cast into a formwork with a smooth surface.

Relative to the four-point bending tests, the three-point bending tests exhibit higher peak strengths and somewhat larger variations of the load-displacement curves. The higher strengths are likely caused by restricting fracture to occur from the notch at midspan. The four-point loading config-

a) three-point bending test   b) four-point bending test
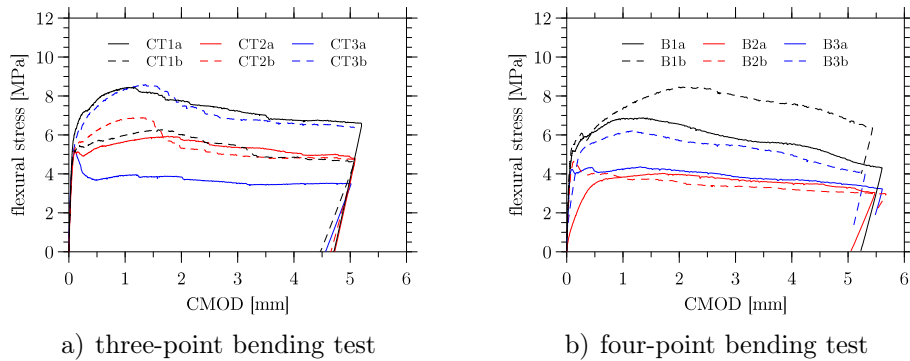
Figure 7.17: *Response of the beam specimens extracted from slabs having ordinary plywood as the formwork.*

a) three-point bending test   b) four-point bending test
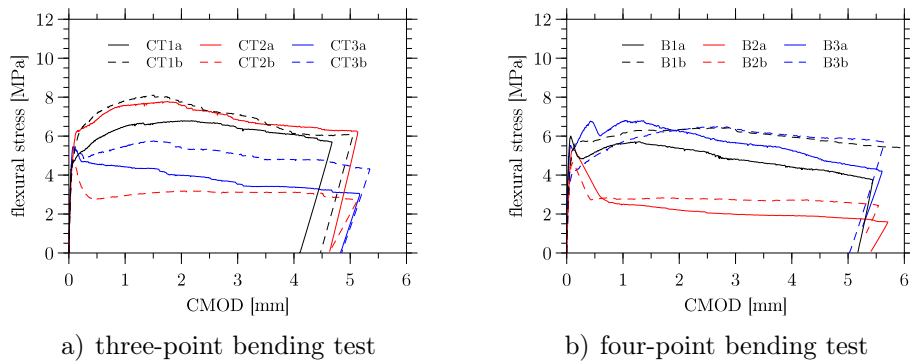
Figure 7.18: *Response of the beam specimens extracted from slabs having glued-sand plywood as the formwork.*

uration produces a larger volume of highly stressed material and allows for failure to occur at potentially weaker locations. Markovic (Markovic, 2006) observed less engagement of the hooked end of steel fibres during fracture of unnotched specimens, compared to notched specimens. The unnotched case facilitates fracture along paths of least resistance that, to some degree, avoid full deformation of the fibre hooks during pullout. Such behaviour contributes to lower strength and toughness of unnotched specimens. The larger variation in the load-displacement curves of the three-point bending tests is likely due to variations in fibre count and fibre orientation in the ligament zone above the notch tip. However, additional data points are needed to make statistically significant conclusions regarding differences between the three-and four-point bending test results.

Numerical simulation of fracture behaviour

Fracture behaviour of the four-point bend specimens, taken from the slab having glue-laminated plywood as the formwork, was numerically simulated by means of the lattice model. Figure 7.19 presents both the numerically and experimentally obtained load-displacement curves for beams B1a, B2a and B3a. As explained in Section 7.2.2, model parameters were adjusted to achieve close agreement with the load-displacement curve of beam B1a. The same parameter set was used for beams B2a and B3a, so the corresponding simulations may be viewed as predictions. The trends with respect to first cracking strength, peak strength, and evolution of post-cracking residual strength are in good qualitative agreement with the experimental results.
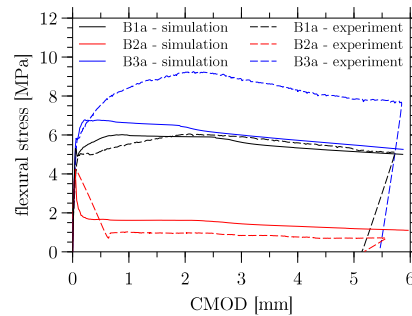
Figure 7.19*: Dependence of fracture behaviour on fibre distribution: comparison of experimental and lattice model results.*

7.3.3   Fibre count local to the fracture plane

This subsection relates the number and orientation of the immersed steel fibres to the fracture behaviour of the beam specimens in a quantitative manner. Figure 7.20 presents flexural stresses of the beam specimens as a function of the number of the steel fibres crossing the cut plane. The flexural stresses correspond to *cmod* = 2.5 mm. The number of fibres crossing the cut planes were manually counted from the prism slices cut from the beam specimens. The cut planes were located approximately 1 - 3 cm from the main fracture plane. The trend lines shown in each plot were determined through linear regression analysis.

To investigate the low value of the coefficient of determination for the three-point bending tests ($R^2 = 0.69$ in Figure 7.20a), the numbers of fibres at the fracture planes were determined by an alternative method. This was done by counting the number of fibres visible on the CT slice images located at the fracture planes. Figure 7.21 presents results of this alternative counting

a) three-point bending test   b) four-point bending test
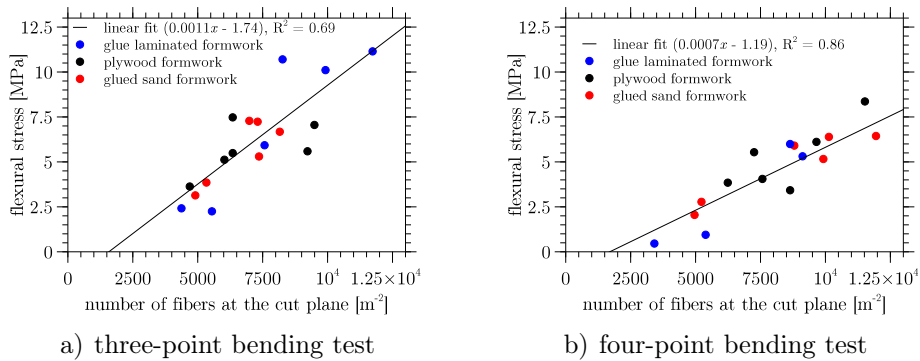
Figure 7.20: *Relation linking flexural stresses of the beam specimens to the number of fibres crossing the cut planes. Manual counting of cut and polished planes.*

approach for two *cmod* values. Comparing the results in Figures 7.20a and 7.21b, it is evident that counting fibres at the CT slice images improved the linear correlation between flexural stress and fibre count.

a) cmod = 1.5 mm   b) cmod = 2.5 mm
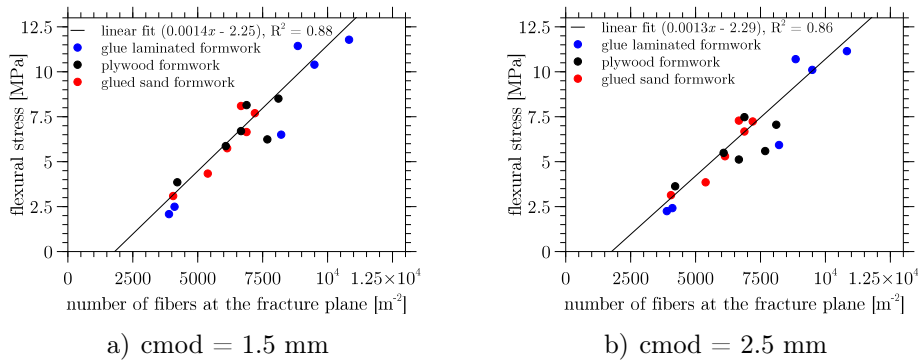
Figure 7.21: *Relation linking flexural stresses of the three-point bending tests to the number of fibres crossing the fracture planes. Manual counting of CT images.*

7.4   Discussion

7.4.1   Fibre orientation

Section 7.3.1 presented the orientation of steel fibres both for the case of the experimental casting and for the case of the numerical simulation. The experimental results indicate that the formwork surface dictates the final

orientation of steel fibres in the region close to the formwork. The influence of the formwork and thus the significance of the formwork surface diminishes with an increasing distance of the steel fibres from the formwork. A rough formwork surface results in a more or less random fibre orientation in the vicinity of the formwork. A smooth surface on the other hand results in a higher degree of fibre orientation in the vicinity of the formwork. The fibre orientations predicted by the simulations and those measured through the experiments are quite similar. Comparison of the results suggests that the Navier's slip model employed in the numerical framework properly models the experimentally observed phenomena.

Numerical simulations were conducted for the two extreme cases of the formwork surface types. Formwork with high surface roughness can be modelled using Navier's slip boundary condition with a slip length of zero, which is equivalent to the no-slip boundary condition. The no-slip boundary condition for viscous fluids states that, at a solid boundary, the fluid has zero velocity relative to the boundary. The shear rates in the xy plane therefore diminish to zero when approaching the boundary, $\dot{\gamma}_{xy} \to 0$. Changes in fibre orientation depend on shearing of the fluid and therefore will not be prominent in the xy plane near no-slip boundaries.

Formwork with highly smooth surfaces can be modelled using the Navier's slip boundary condition of an infinite slip length. The relative velocity of the fluid at the boundary and tangent to the boundary is then not restricted by the boundary. Fully developed shear rates in the xy plane, driven in accordance with the flow pattern, are present at the solid boundary, where $|\dot{\gamma}_{xy}| \gg 0$ is possible. The steel fibres located close to the formwork then orient in the xy plane according to the flow pattern.

Any other type of formwork surface can be seen as a combination of the two aforementioned extreme cases. Qualitative evidence of the zero and non-zero relative velocities of the flow of the fibre reinforced self-compacting concrete at the formwork can be observed in the attached video (footnote on Page 122).

7.4.2 Mechanical properties

The beam specimens extracted from the slabs exhibited varying degrees of scatter when subjected to flexural loading. The largest amount of scatter was observed for fibre-reinforced concrete cast on the glue-laminated plywood formwork. The load-displacement behaviour of this set of beams was simulated using the lattice model. The positions and orientations of the steel fibres, which are required as input to the lattice model, were obtained from the numerical simulation of flow.

The overall trends in first cracking strength, peak load, and residual (post-peak) strength have been predicted by the lattice model. Since the model specimens were nominally identical, except for differences in the statistical distribution of immersed fibres, the simulation results support the observations made in Section 7.3.3, i.e., that fibre count and orientation local to the fracture plane are decisive factors in determining fracture behaviour. We believe that the underestimation of strength and toughness of beam B3 in Figure 7.19 was caused by the lower number of fibres obtained from the numerical simulation of the casting process. Beam B3 is adjacent to the vertical part of the formwork at a large distance from the inlet position (see Figure 7.4). An examination of this region found that, although the orientation distribution of fibres was accurately represented, the simulated flow carried a smaller number of fibres to the vicinity of the formwork wall. The lower fibre count in this boundary region contributed to the lower strength prediction of the lattice model, relative to that measured in the four-point bend test.

The spatial distribution and orientations of the steel fibres are influenced by the formwork surface. The formwork surface can therefore play a significant role in the mechanical response of structural elements, especially when the depth of the element is not large relative to the depth of the affected zone near the formwork surface. Although not studied herein, similar concerns would be present when casting fibre-reinforced self compacting concrete over a concrete substrate (e.g., as a repair layer).

7.4.3   Fibre count local to the fracture plane

Section 7.3.3 presented relations between the flexural stresses at specified CMOD values and the number of fibres at the fracture plane. The relations exhibited a strong linear trends similarly to (Zerbino et al., 2012). Contrarily to (Zerbino et al., 2012), the linear relation intercepted the x axis (representing the number of fibres intersecting a unit area of the fracture plane) at approximately $1700\,\mathrm{m}^{-2}$. The apparent non-zero intercepts indicate that, for the specimens examined herein, there is an apparent critical threshold below which the effect of the steel fibres is negligible.

Based on the experimental observations and the numerical simulations of fracture behaviour, we believe that the linear trend, and its apparent non-zero intercept, is caused by two main factors: a) the number of fibres intersecting the fracture plane; and b) the inclination of intersecting fibres to the fracture plane. For the CT2 set of beam specimens, not only are the numbers of fibres intersecting the fracture plane smaller, but a greater fraction of those fibres are lowly inclined to the fracture plane. Inclination of fibres to the

fracture plane can strongly affect the pullout behaviour of individual fibres (Li et al., 1990; Ouyang et al., 1994; Laranjeira et al., 2010). In particular, for small entry angles the pullout resistance is greatly diminished due to spalling of the matrix local to the entry points of the fibres (Lee et al., 2010). We believe that the combined effects of fibre count and such variations in pullout behaviour contribute to the shift in the x-intercept from 0 to about $1700\,\mathrm{m}^{-2}$. Other recent study of beams extracted from fibre reinforced self-compacting concrete slabs has produced similar linear trends between fibre count at the fracture surface and residual stress (Zerbino et al., 2012). With reducing fibre count, however, their trend lines head toward the origin, exhibiting a different trend than found herein.

Results obtained from the manual counting of the CT slice images show a linear dependence of residual stress on fibre count with high coefficient of determination, $R^2 \approx 0.86$. Results obtained from the manual counting of fibres on slices cut from the same beam specimens indicate a similar trend, but with a lower coefficient of determination, $R^2 \approx 0.69$. The difference between the two coefficients of determination suggests that the accuracy of the results is sensitive to the measurement technique. Implicit within this discussion is the assumption that the distribution of fibres is reasonably uniform over the depth of the specimen.

7.5 Conclusions

The work presented in this paper involves the combined use of experiments and numerical modelling techniques to investigate several important aspects of the fibre reinforced self-compacting concrete. We demonstrated that the orientations of immersed steel fibres evolve in response to the flow of the self-compacting concrete within the formwork. We further showed that the formwork surface, among other factors, plays a significant role in the final orientation of the immersed steel fibres. Within the casting simulations, roughness of the formwork surfaces was effectively modelled using Navier's slip boundary condition with appropriate slip lengths. Rough surfaces reduce the rate of fluid shearing and thus the tendency for fibres to orient according to the flow direction. Fibre orientation exhibits a greater degree of randomness near such rough surfaces. Furthermore, flexural tests of elements extracted from the cast slabs indicated that the final orientation of the steel fibres can have a strong influence on the resulting mechanical properties of the fibre reinforced self-compacting concrete. Consequently the formwork surface also can have a strong influence on the resulting mechanical response of the structure, particularly if the depth of the elements is not large relative

to the size of the affected zone.

The proposed use of computational fluid dynamics simulations to determine fibre coordinates within cast self-compacting concrete, in tandem with fracture modelling that makes direct use of that information, is a novel means for connecting methods of processing to the mechanical performance of fibre-reinforced cement composites. This simulation pathway provided accurate estimates of first cracking strength, peak strength, and residual strength of the beam specimens testing in four-point bending. The experimental measurements and model results confirm that there is a linear relationship between the residual stress carried by beam specimens and the number of the immersed steel fibres, and their orientation, local to the main fracture plane. Furthermore, the sample set considered herein included beams in which there were few fibres intersecting the fracture plane. A relatively larger fraction of these same fibres were lowly inclined to the fracture plane, which likely reduced their pullout resistance. The combination of fewer fibres intersecting the fracture plane and the relatively lower pullout resistance of those fibres contributed the non-zero x-intercept of the trend lines.

The ability to simulate the casting process of fibre reinforced self-compacting concrete, including the movement of individual immersed fibres in response to such factors as formwork geometry and surface roughness, has profound implications toward the effective use of these materials within the civil infrastructure. As demonstrated herein, the results of such flow simulations can serve as input to mechanical models of material behaviour. Together with physical experimentation, this coupled simulation of concrete casting and its load resistance in the hardened state presents opportunities for improving material performance for both ordinary and high-performance applications.

7.6   Acknowledgments

Chapter 8

A collection of videos

This section presents a collection of videos of experiments and a collection of animations of numerical simulations created during the research project. Each figure or sub-figure contains one video or animation. The video or animation can be accessed by double-clicking on the the figure or on the sub-figure. Alternatively, all the videos and animations can be in the case of Adobe Acrobat Reader accessed from the "Attachments" menu (Figure 8.1). All the videos and animations are encoded in the standardized MP4/H264 format.
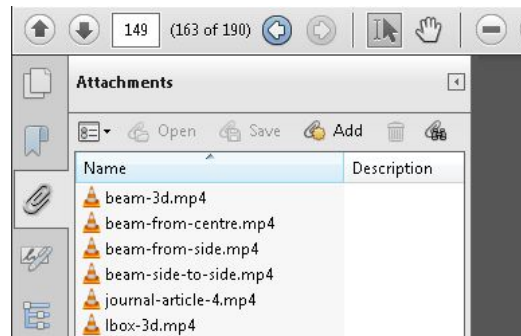
Figure 8.1: *Screen-shot of Adobe Acrobat Reader showing the Attachments menu with the attached videos.*

8.1 Slump flow

Section 2.3.1 studied the accuracy of the developed numerical framework on an example of homogeneous and heterogeneous slump flow experiment. In this section, animation of one of the numerical simulations is presented. The

presented numerical simulation contains explicitly represented rigid spheres (i.e. aggregates) and cylinders (i.e. steel fibres) immersed in the free surface flow of homogeneous Bingham plastic fluid (i.e. self-compacting concrete).

a)   b)
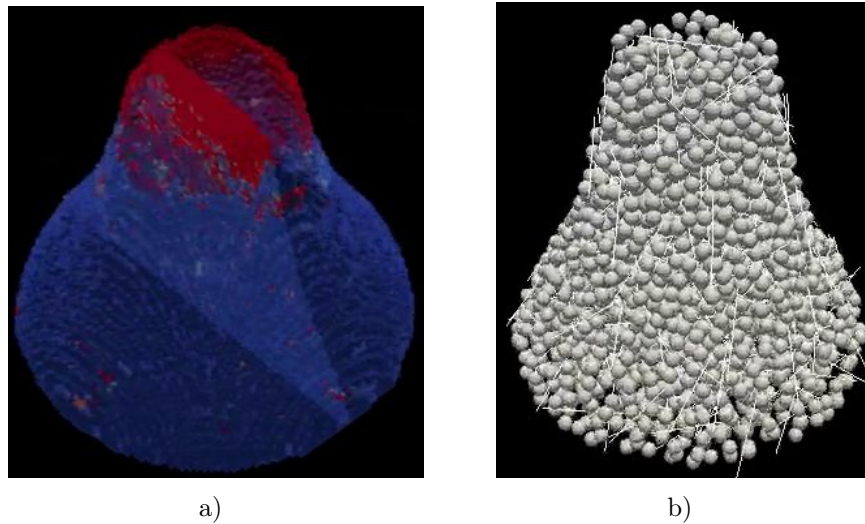
Figure 8.2: *Numerical simulation of slump flow of fibre reinforced self-compacting concrete. a) Fluid part (colour by viscosity, red = high, blue = low). b) Immersed particles.*

Plastic viscosity, yield stress and density of the fluid were in the simulation set to 30 Pas, 50 Pa and 2500 kg/m³, respectively. Fibre density, length, aspect ratio and volume fraction were 7850 kg/m³, 6 cm, 80 and 0.2 %, respectively. Aggregate density, diameter and volume fraction was set to 2600 kg/m³, 1 cm and 25 %, respectively. The overall spatial domain of the numerical simulations was parallelized into 9 sub-domains. The numerical simulation took almost one month to finish.

Figure 8.2 presents an animation of the slump flow. The animation was for convenience split into the fluid part (Figure 8.2a) and into the corresponding immersed steel fibres and aggregates (Figure 8.2b). The fluid part is coloured by the apparent viscosity of the homogeneous Bingham plastic fluid. Blue colour denotes liquid regions of low apparent viscosity (≈ 50 Pas) whereas red colour denotes stiff regions of high apparent viscosity (≈ 200 Pas).

The presented numerical simulation highlights the core features of the developed numerical framework; namely the free surface, non-Newtonian rheology, explicitly represented fibres and aggregates, two-way interaction between the fluid and the immersed particles, interaction among the particles, interaction between the particles and formwork, coefficient of restitution

and Coulomb friction coefficient for the collisions and parallelization of the computational domain.

8.2 L-Box flow

Several numerical simulations of L-Box flow were carried out as part of the work described in Chapter 6 and compared to experimental results of transparent gel Carbopol. The Carbopol gel was modelled as a free surface flow of homogeneous Bingham plastic fluid. Various number of reinforcement bars was placed into the L-Box during the experiments. In this section, one of the experiments is presented both in the form of experimental videos and numerical animations.

Plastic viscosity, yield stress and density of the Carbopol gel were in the simulation set to $15\,\mathrm{Pas}$, $30\,\mathrm{Pa}$ and $950\,\mathrm{kg/m^3}$, respectively. Fibre density, length, aspect ratio and volume fraction were $7500\,\mathrm{kg/m^3}$, $3\,\mathrm{cm}$, 80 and $0.5\,\%$, respectively. Three reinforcement bars were used in the L-Box experiment and in the numerical simulation. The spatial domain was not parallelized. The numerical simulation took approximately two months to finish.

a)   b)   c)
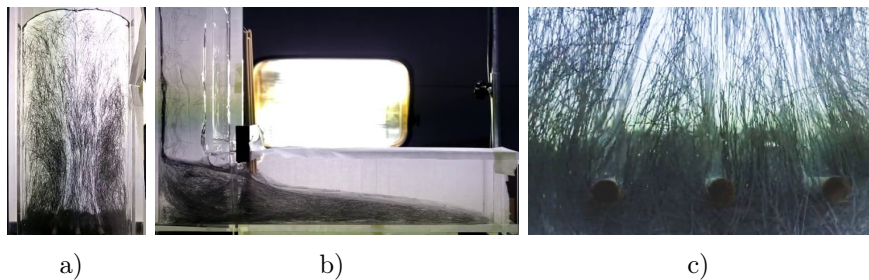
Figure 8.3: *Experimental L-Box casting using transparent gel Carbopol. a) Bottom view. b) Side view. c) Detailed view.*

Figure 8.3 shows three videos of the casting process of the Carbopol gel suspension. Figure 8.3a presents a bottom view of the casting process and highlights the effect of the three reinforcement bars on the global flow pattern of the immersed fibres. Figure 8.3b presents a side view of the casting process whereas Figure 8.3c shows a detail view of the casting process with focus on the region in the vicinity of the reinforcement bars. The detail view reveals a strong influence of the bars on the local orientation of the steel fibres.

Figure 8.4 presents animation of the corresponding numerical simulation. Similarly to Section 8.1, the animation was for convenience split into the fluid part (Figure 8.4a) and fibre part (Figure 8.4b,c). The fluid part is coloured

a)   b)   c)
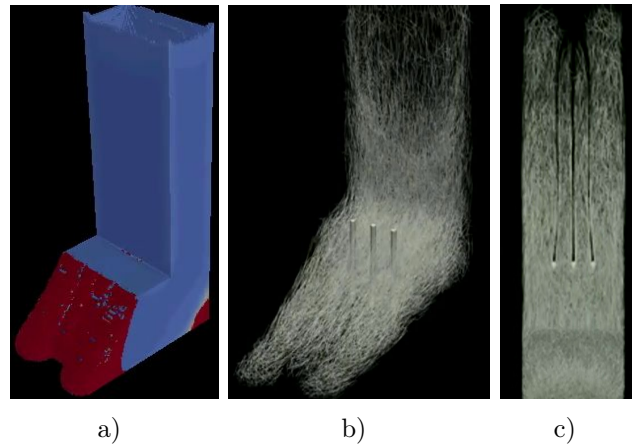
Figure 8.4: *Numerical simulation of the respective L-Box casting. a) Fluid (colour by viscosity, red = high, blue = low). b) 3D view of fibres. c) Top view of fibres.*

by the apparent viscosity of the homogeneous Bingham plastic fluid. Blue colour denotes liquid regions of low apparent viscosity ($\approx 20\,\mathrm{Pas}$) whereas red colour denotes stiff regions of high apparent viscosity ($\approx 100\,\mathrm{Pas}$). Similarly to experimental observations in Figure 8.3a, the top view animation in Figure 8.4c reveals a strong influence of the three reinforcement bars on the flow pattern of the immersed steel fibres. The reinforcement bars seem to create thin and long stream shaped regions with almost no fibres. The presented videos therefore among others highlight the capability of the numerical framework to properly include reinforcement bars into the numerical simulation.

Both experimental videos and numerical animations indicate significant and quick orientation of the immersed steel fibres. The orientation is primarily driven by the wall effect and by the shear induced orientation (see Section 1.1).

8.3   Standard size beam casting

Three numerical simulations of standard size beam (RILEM TC 162-TDF) casting were run to study the impact of the casting process on the resulting orientation and distribution of steel fibres immersed in the fibre reinforced self-compacting concrete and consequently on the mechanical response of the beams in the hardened state.

Plastic viscosity, yield stress and density of the fluid were in the simula-

tion set to $20\,\mathrm{Pas}$, $20\,\mathrm{Pa}$ and $2300\,\mathrm{kg/m^3}$, respectively. Fibre density, length, aspect ratio and volume fraction were $7850\,\mathrm{kg/m^3}$, $6\,\mathrm{cm}$, 80 and $0.2\,\%$, respectively. In the case of Figure 8.5c, the translational speed of the inlet was $1\,\mathrm{m/s}$.
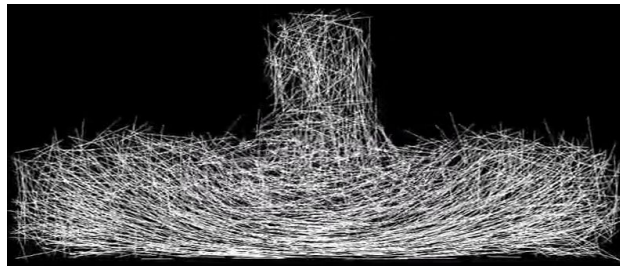
a) Casting from centre
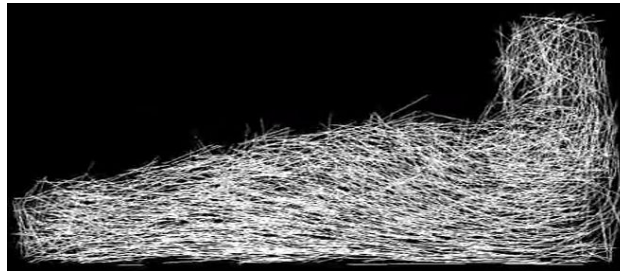
b) Casting from one side
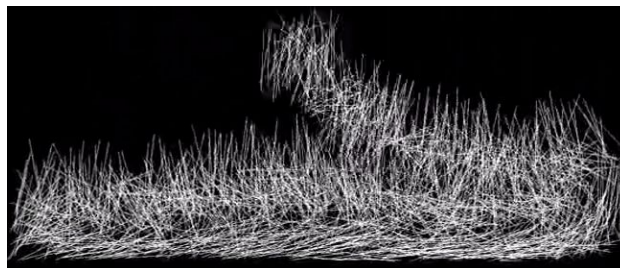
c) Casting movable from side to side

Figure 8.5: *Numerical simulation of beam casting with fibre reinforced self-compacting concrete. Side view of three different casting types.*

Figure 8.5 shows side view animations of fibre part of the three numerical simulations. The fluid part was for convenience removed. The three beam specimens were cast from a circular inlet positioned in the centre of the beam, at the right side of the beam and from an inlet movable from side to side. Te individual animations indicate clearly mutually different fibre orientation patterns.

The presented videos highlight the significance of the type of casting on

the resulting fibre orientation and distribution. The three simulations indicate that the casting process of standard size beams might have an influence on the mechanical behaviour of the hardened beam specimens. The three numerical simulations therefore accentuate the need to specify the casting process and have information about the resulting fibre orientation.

8.4   Slab casting

Three numerical simulations of slab casting were carried out as part of the work described in Chapter 7 and compared to the corresponding experimental observations. The three slabs were differentiated by the type of the formwork surface roughness, ranging from smooth glue laminated plywood to rough glued sand formwork. Videos of the experiments together with animations of the numerical simulations are presented in this section.

Dimensions of the slabs were $1.2\,\text{m} \times 1.2\,\text{m} \times 0.15\,\text{m}$. Plastic viscosity, yield stress and density of the fluid were in the simulation set to $75\,\text{Pas}$, $22\,\text{Pa}$ and $2318\,\text{kg/m}^3$, respectively. Fibre density, length, aspect ratio and volume fraction were $7850\,\text{kg/m}^3$, $6\,\text{cm}$, 80 and $0.5\,\%$, respectively. Navier's slip lengths of the three formwork surfaces were $0\,\text{cm}$, $8\,\text{cm}$ and ∞. Spatial domain of the presented numerical simulation was parallelized into 16 subdomains. The numerical simulation took approximately one week to finish.

a)   b)   c)
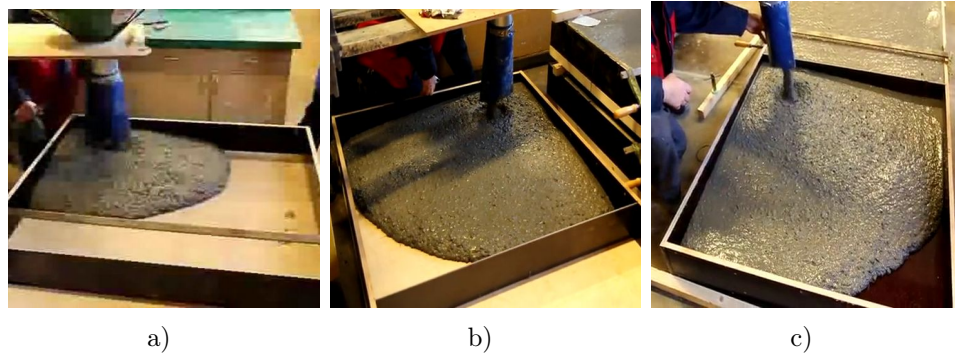
Figure 8.6: *Experimental slab casting of fibre reinforced self-compacting concrete for three different formwork surface types. a) Glued sand plywood. b) Ordinary plywood. c) Glue laminated plywood.*

Figure 8.6 presents videos of the three experimental castings of the slabs having the various types of the formwork surface. Figure 8.7 shows an animation of the slab casting having the smooth glue laminated plywood as the formwork. Figure 8.8 presents a top view animation of the fibre orientation

within the bottom half of the three different slabs. The fibre orientation is illustrated in the form of 3D orientation ellipsoids. Figure 8.8 reveals that smooth surface results in a considerably higher degree of fibre orientation compared to rough surface.
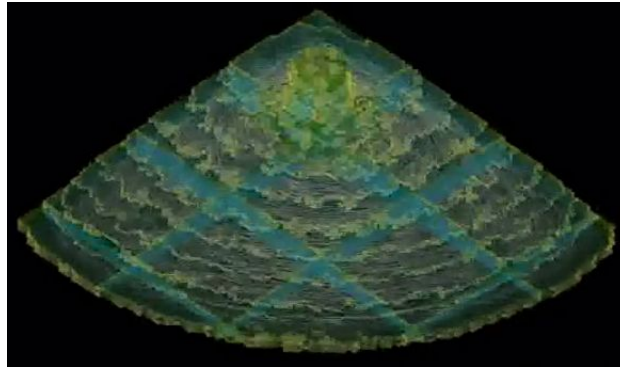
Figure 8.7: *Numerical simulation of slab casting with boundary condition corresponding to glue laminated plywood.*

The presented animations of numerical simulations highlight the influence of formwork surface on the fibre orientation in the vicinity of the formwork. Rough formwork surface generally results in close to random fibre orientation whereas smooth formwork surface generally results in fairly orientated fibres in the vicinity of the formwork. The presented animations and especially the animation in Figure 8.8c clearly indicates the extensional stresses induced fibre orientation, as defined in Section 1.1.

a)   b)   c)
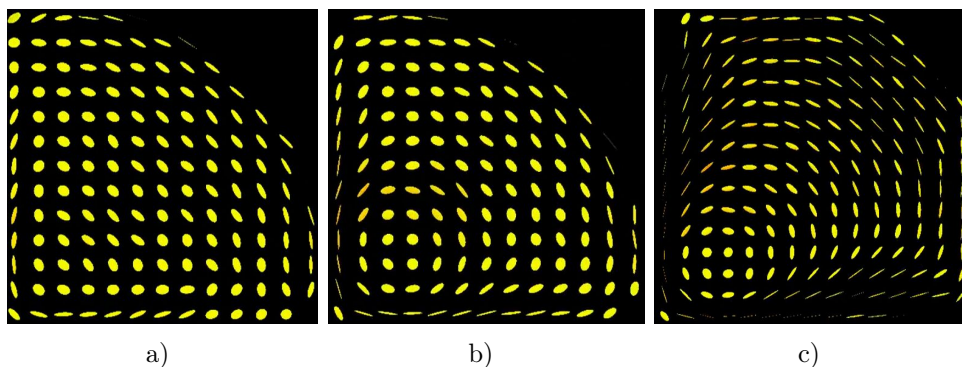
Figure 8.8: *Top view on orientation ellipsoids within the bottom half of the slab. a) Slip length $= 0$ cm. b) Slip length $= 8$ cm. c) Slip length $= \infty$*

8.5 Wall casting

Several numerical simulations of wall casting were carried out in collaboration with Norwegian University of Science and Technology to study the effect of formwork surface roughness and wall stiffeners on the resulting fibre orientation. This section shows the effect of formwork stiffeners on the fibre orientation.

Dimensions of the wall were $1.5\,\text{m} \times 1\,\text{m} \times 0.15\,\text{m}$. The wall was cast from circular inlet positioned at the left part of the wall. The circular inlet was kept 10 cm above the level of concrete. Plastic viscosity, yield stress and density of the fluid were in the simulation set to 60 Pas, 25 Pa and $2500\,\text{kg/m}^3$, respectively. Fibre density, length, aspect ratio and volume fraction were $7850\,\text{kg/m}^3$, 6 cm, 80 and 0.5 %, respectively. Diameter of the wall stiffeners was set to 20 mm. Navier's slip lengths of the formwork surface was 8 cm. Spatial domain of the presented numerical simulation was parallelized into 10 sub-domains. The numerical simulation took approximately 20 days to finish.

a)   b)
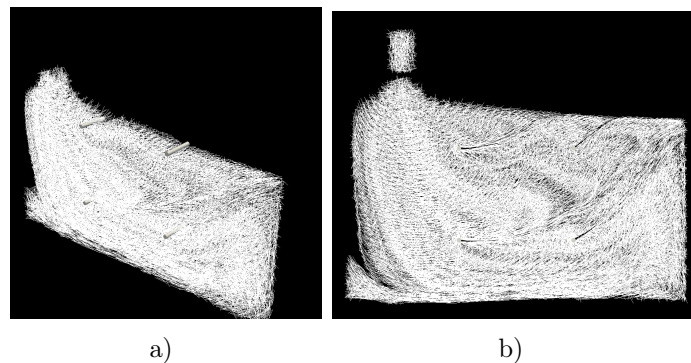
Figure 8.9: *Numerical simulation of wall casting with fibre reinforced self-compacting concrete. a) 3d view. b) Side view.*

Figure 8.9 presents 3D view and side view animations of the numerical simulation. Figure 8.9a together with Figure 8.10 reveal a clear influence of the wall stiffeners on the fibre orientation. Similarly to Section 8.2, each of the stiffeners creates long stream shaped region with almost no fibres. Figure 8.10 also indicates the global pattern of fibre orientation in the wall. Orientation of the steel fibres immersed in the wall is primarily driven by the wall effect and shear induced orientation, as defined in Section 1.1.
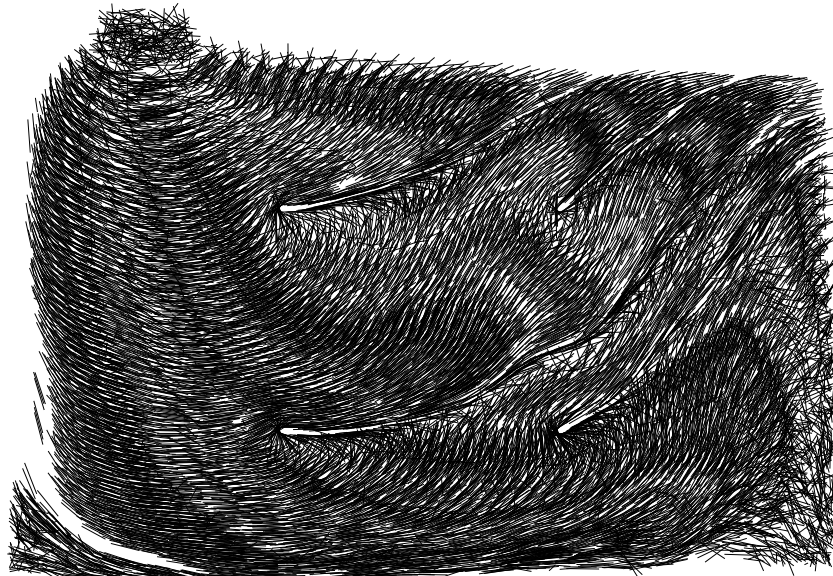
Figure 8.10: *Side view of the final state of steel fibres immersed in the wall.*

Chapter 9

Conclusions and future perspectives

9.1 Conclusions

One of the most important parts of a design process of fibre reinforced self-compacting concrete structures is the ability to reliably predict the orientation and distribution of steel fibres immersed in the concrete. Development of a numerical framework capable of predicting the fibre orientation and distribution was therefore the primary aim of the presented research project.

The developed numerical framework allows for simulations of tens of thousands of explicitly represented rigid particles immersed in the free surface flow of homogeneous non-Newtonian fluid. The non-Newtonian fluid was simulated by the Lattice Boltzmann fluid dynamics solver. The immersed rigid particles were two-way coupled with the surrounding fluid by means of the Immersed boundary method with direct forcing. The rigid particles were allowed to have an arbitrary shape and surface type. The varying surface type was simulated by coefficient of restitution and by Coulomb friction coefficient. We observed that the Immersed boundary method was not able to correctly predict drag forces acting on fibres of a sub-grid diameter. A correction function was therefore developed. Boundary conditions such as formwork are commonly simulated as a no-slip boundary condition. A method incorporating a variable Navier's slip boundary condition into the lattice Boltzmann fluid dynamics solver was proposed. A range of experiments was conducted to validate the ability of the numerical framework to properly predict fibre orientation and distribution in the fibre reinforced self-compacting concrete. All the experimental results favourably matched the corresponding numerical simulations.

155

Several other important conclusions were drawn from the experiments and from the respective numerical simulations:

Fibres orient: Both numerically and experimentally, it was confirmed that the immersed steel fibres very quickly orient under the flow of fibre reinforced self-compacting concrete following a combination of all the basic phenomena described in Section 1.1.

Obstacles affect fibre orientation: Obstacles such as steel reinforcement bars seem to have a significant effect on the orientation and distribution of fibres immersed in the fibre reinforced self-compacting concrete. Reinforcement bars as an example create stream shaped regions in which no fibres are present, as shown in the previous section.

Aggregates can be replaced by yield stress: In the majority of the performed numerical simulations, the fibre reinforced self-compacting concrete was modelled as explicitly represented steel fibres immersed in the homogeneous Bingham plastic fluid. The effect of aggregates present in the concrete was modelled by the yield stress of the fluid. In all the studied cases, the resulting fibre orientations favourably matched corresponding experimental observations. These results suggest that such a simplified representation of the immersed aggregates is often a reasonable and efficient assumption.

Formwork surface type matters: Both numerically and experimentally, it was observed that the formwork surface type (such as smooth glue laminated plywood or rough ordinary plywood) has a strong influence on the orientation of fibres located near the formwork. It was further observed that the effect of formwork surface diminished with an increasing distance of the fibres from the formwork.

Fibre orientation influences mechanical behaviour: It was both numerically and experimentally observed that the local fibre orientation has an influence on the mechanical response of structural elements made of fibre reinforced self-compacting concrete. By two distinct sets of slab casting experiments we observed that there is a prevailing linear dependence between the mechanical response of a structure (i.e. flexural stresses) and the respective fibre orientation factor. It was also experimentally observed that the linear relation does not intersect origin (i.e. $[x = 0, y = 0]$). Instead there is an apparent intersection point $[x > 0, y = 0]$ which suggests that for low but non-zero orientation factor the mechanical response of the element diminishes.

The ability to simulate the casting process of fibre reinforced self-compacting concrete, including the orientation of individual immersed fibres in response to such factors as casting method, formwork geometry and surface roughness, has profound implications regarding the effective use of these materials. Together with physical experimentation, coupled simulation of concrete casting and its load resistance in the hardened state presents opportunities for improving material performance for both ordinary and high-performance applications.

9.2 Future perspectives

Although the developed numerical framework is capable of predicting the flow of fibres and aggregates immersed in the fibre reinforced self-compacting concrete, there is still a range of potential places for improvements.

The number of explicitly represented immersed fibres and aggregates is limited by the computational power available. As an example, we have so far simulated up to one hundred thousand immersed particles, which corresponds to relatively small scale structures. A further investigation allowing for at least millions of simulated immersed particles is therefore of a high interest.

Most of the computation power is currently taken by the Runge-Kutta integration scheme. Investigation of alternative lightweight integration schemes could potentially increase the computational efficiency of the numerical framework.

Extremely fast single purpose coprocessors such as graphic cards are a promising alternative to the relatively slow multi-purpose computational processors (CPU). The significant increase in the computational power comes however at the cost of a very restricted programming environment. The possibility to modify the presented numerical framework to be run on the coprocessors could be investigated.

The limited computation resources could be alternatively overcome by simulating the immersed fibres and aggregates on multiple physical scales. As an example, the general flow of the fibres could be potentially simulated by their statistical representation, e.g. by fibre orientation tensors. The local effects such as collisions with the reinforcement, collisions with the formwork or collisions among the fibres could be then simulated explicitly by the presented numerical framework.

The presented numerical framework contains a very limited set of features, implemented with a primary focus on fibre reinforced self-compacting concrete. The inclusion and study of phenomena such as deformable fibres, non-spherical aggregates, arbitrary shaped fibres, concrete thixotropy, con-

crete hardening, thermal flow, multi-component and multi-phase flow could be of interest for further investigation.

Bibliography

Suresh G. Advani and Charles L. Tucker. The Use of Tensors to Describe and Predict Fiber Orientation in Short Fiber Composites. *Journal of Rheology*, 31(8):751, 1987. ISSN 01486055. doi: 10.1122/1.549945. URL `http://link.aip.org/link/?JOR/31/751/1&Agg=doi`.

NK Ahmed and Martin Hecht. A boundary condition with adjustable slip length for lattice Boltzmann simulations. *Journal of Statistical Mechanics: Theory and Experiment*, 2009(09):1–14, 2009. URL `http://iopscience.iop.org/1742-5468/2009/09/P09017`.

Cyrus K. Aidun and Jonathan R. Clausen. Lattice-Boltzmann Method for Complex Flows. *Annual Review of Fluid Mechanics*, 42(1):439–472, January 2010. ISSN 0066-4189. doi: 10.1146/annurev-fluid-121108-145519. URL `http://arjournals.annualreviews.org/doi/abs/10.1146/annurev-fluid-121108-145519http://www.annualreviews.org/doi/abs/10.1146/annurev-fluid-121108-145519`.

Cyrus K. Aidun and Yannan Lu. Lattice Boltzmann simulation of solid particles suspended in fluid. *Journal of Statistical Physics*, 81(1-2):49–61, October 1995. ISSN 0022-4715. doi: 10.1007/BF02179967. URL `http://www.springerlink.com/content/3357q5686858p414/http://www.springerlink.com/index/10.1007/BF02179967`.

D. Asahina, E.N. N Landis, and J.E. E Bolander. Modeling of phase interfaces during pre-critical crack growth in concrete. *Cement and Concrete Composites*, 33(9):966–977, October 2011. ISSN 09589465. doi: 10.1016/j.cemconcomp.2011.01.007. URL `http://linkinghub.elsevier.com/retrieve/pii/S0958946511000138`.

David Baraff. An Introduction to Physically Based Modeling : Rigid Body Simulation I - Unconstrained Rigid Body Dynamics, 1997a. URL `http://excelsior.cs.ucsb.edu/courses/cs290n_cg_modeling/notes/cmu_notes/rigid1.pdf`.

David Baraff. An Introduction to Physically Based Modeling : Rigid Body Simulation II - Nonpenetration Constraints, 1997b. URL `http://www.cs.cmu.edu/afs/cs.cmu.edu/user/baraff/www/sigcourse/notesd2.pdf`.

Stephanie J. Barnett, Jean-Francois Lataste, Tony Parry, Steve G. Millard, and Marios N. Soutsos. Assessment of fibre orientation in ultra high performance fibre reinforced concrete and its effect on flexural strength. *Materials and Structures*, 43(7):1009–1023, October 2009. ISSN 1359-5997. doi: 10.1617/s11527-009-9562-3. URL `http://www.springerlink.com/index/10.1617/s11527-009-9562-3`.

G. K. Batchelor and J. T. Green. The determination of the bulk stress in a suspension of spherical particles to order c 2. *Journal of Fluid Mechanics*, 56(03):401, March 2006. ISSN 0022-1120. doi: 10.1017/S0022112072002435. URL `http://www.journals.cambridge.org/abstract_S0022112072002435`.

A Ben Richou, A Ambari, and J.K Naciri. Drag force on a circular cylinder midway between two parallel plates at very low Reynolds numbers—Part 1: Poiseuille flow (numerical). *Chemical Engineering Science*, 59(15):3215–3222, August 2004. ISSN 00092509. doi: 10.1016/j.ces.2003.10.031. URL `http://linkinghub.elsevier.com/retrieve/pii/S0009250904001587`.

R. Blanc, Ch. Germain, J.P. Da Costa, P. Baylou, and M. Cataldi. Fiber orientation measurements in composite materials. *Composites Part A: Applied Science and Manufacturing*, 37(2):197–206, February 2006. ISSN 1359835X. doi: 10.1016/j.compositesa.2005.04.021. URL `http://linkinghub.elsevier.com/retrieve/pii/S1359835X05002472`.

John E. Bolander, Sokhwan Choi, and Sri Ramya Duddukuri. Fracture of fiber-reinforced cement composites: effects of fiber dispersion. *International Journal of Fracture*, 154(1-2):73–86, February 2008. ISSN 0376-9429. doi: 10.1007/s10704-008-9269-4. URL `http://www.springerlink.com/index/10.1007/s10704-008-9269-4`.

Bensaid Boulekbache, Mostefa Hamrat, Mohamed Chemrouk, and Sofiane Amziane. Flowability of fibre-reinforced concrete and its effect on the mechanical properties of the material. *Construction and Building Materials*, 24(9):1664–1671, September 2010. ISSN 09500618. doi: 10.1016/j.conbuildmat.2010.02.025. URL `http://linkinghub.elsevier.com/retrieve/pii/S0950061810000681`.

J Boyd, J Buick, and S Green. A second-order accurate lattice Boltzmann non-Newtonian flow model. *Journal of Physics A: Mathematical and General*, 39(46):14241–14247, November 2006. ISSN 0305-4470. doi: 10.1088/ 0305-4470/39/46/001. URL `http://stacks.iop.org/0305-4470/39/i= 46/a=001?key=crossref.0095c759956958c752fdac1c62479fc6`.

Shqiponja Bytyci. *Design and optimization of "Combi-Slab"*. Master thesis, Technical University of Denmark, 2012.

Zhenhua Chai, Baochang Shi, Zhaoli Guo, and Fumei Rong. Multiple-relaxation-time lattice Boltzmann model for generalized Newtonian fluid flows. *Journal of Non-Newtonian Fluid Mechanics*, 166(5-6): 332–342, March 2011. ISSN 03770257. doi: 10.1016/j.jnnfm. 2011.01.002. URL `http://linkinghub.elsevier.com/retrieve/pii/ S0377025711000073`.

Shiyi Chen and Gary D. Doolen. LATTICE BOLTZMANN METHOD FOR FLUID FLOWS. *Annual Review of Fluid Mechanics*, 30(1): 329–364, January 1998. ISSN 0066-4189. doi: 10.1146/annurev.fluid. 30.1.329. URL `http://www.annualreviews.org/doi/abs/10.1146/ annurev.fluid.30.1.329`.

D D L Chung. Monitoring fiber dispersion in fiber-reinforced cementitious materials: Comparison of AC-impedance spectroscopy and image analysis. Paper by Nilufer Ozyurt, Leta Y. Woo, Thomas O. Mason, and Surendra P. Shah - Discussion. *ACI MATERIALS JOURNAL*, 104(4):434–435, 2007. ISSN 0889325X.

Stephan Van Damme. Nondestructive determination of the steel fiber content in concrete slabs with an open-ended coaxial probe. *Geoscience and Remote Sensing*, 42(11):2511–2521, 2004. URL `http://ieeexplore.ieee. org/xpls/abs_all.jsp?arnumber=1356064`.

P. G. de Gennes. On Fluid/Wall Slippage. *Langmuir*, 18(9):3413–3414, April 2002. ISSN 0743-7463. doi: 10.1021/la0116342. URL `http://pubs.acs. org/doi/abs/10.1021/la0116342`.

F Dufour and G Pijaudier-Cabot. Numerical modelling of concrete flow: homogeneous approach. *International Journal for Numerical and Analytical Methods in Geomechanics*, 29, 2005.

P.J.J. Dumont, S. Le Corre, L. Orgéas, and D. Favier. A numerical analysis of the evolution of bundle orientation in concentrated fibre-bundle suspen-

sions. *Journal of Non-Newtonian Fluid Mechanics*, 160(2-3):76–92, August 2009. ISSN 03770257. doi: 10.1016/j.jnnfm.2009.03.001. URL `http://linkinghub.elsevier.com/retrieve/pii/S0377025709000627`.

David Dupont and Lucie Vandewalle. Distribution of steel fibres in rectangular sections. *Cement and Concrete Composites*, 27(3):391–398, March 2005. ISSN 09589465. doi: 10.1016/j.cemconcomp.2004.03.005. URL `http://linkinghub.elsevier.com/retrieve/pii/S0958946504001295`.

F Dupret and V Verleye. Modelling the flow of fiber suspensions in narrow gaps. *Rheology Series*, 8:1347–1398, 1999. doi: 10.1016/S0169-3107(99)80020-3. URL `http://www.sciencedirect.com/science/article/pii/S0169310799800203`.

M Faifer and R Ottoboni. A multi-electrode measurement system for steel fiber reinforced concrete materials monitoring. *Instrumentation and Measurement Technology*, (May):5–7, 2009. URL `http://ieeexplore.ieee.org/xpls/abs_all.jsp?arnumber=5168466`.

Marco Faifer and Roberto Ottoboni. Nondestructive testing of steel-fiber-reinforced concrete using a magnetic approach. *Instrumentation and Measurement Technology*, 60(5):1709–1717, 2011. URL `http://ieeexplore.ieee.org/xpls/abs_all.jsp?arnumber=5658147`.

Olov Hilding Faxén. Forces exerted on a rigid cylinder in a viscous fluid between two parallel fixed planes. In *Proceedings of the Royal Swedish Academy of Engineering Sciences 187*, pages 1–13, 1946.

Zhi-Gang Feng and Efstathios E. Michaelides. Proteus: a direct forcing method in the simulations of particulate flows. *Journal of Computational Physics*, 202(1):20–51, January 2005. ISSN 00219991. doi: 10.1016/j.jcp.2004.06.020. URL `http://linkinghub.elsevier.com/retrieve/pii/S0021999104002669`.

Zhi-Gang Feng and Efstathios E. Michaelides. Robust treatment of no-slip boundary condition and velocity updating for the lattice-Boltzmann simulation of particulate flows. *Computers & Fluids*, 38(2):370–381, February 2009. ISSN 00457930. doi: 10.1016/j.compfluid.2008.04.013. URL `http://linkinghub.elsevier.com/retrieve/pii/S0045793008001060`.

L Ferrara, Y.-D. Park, and S P Shah. Correlation among fresh state behavior, fiber dispersion, and toughness properties of SFRCs. *J. Mat. Civil Eng.*, 20(7):493–501, 2008.

L Ferrara, N Ozyurt, and M di Prisco. High mechanical performance of fibre reinforced cementitious composites: the role of casting-flow induced fibre orientation. *Mat. Struct.*, 44:109–128, 2011.

Fransisco Folgar and Charles L Tucker. Orientation behavior of fibers in concentrated suspensions. *Journal of Reinforced Plastics and Composites*, 3(2):98–119, 1984.

R. Gettu. Study of the distribution and orientation of fibers in SFRC specimens. *Materials and Structures*, 38(275):31–37, December 2004. ISSN 1359-5997. doi: 10.1617/14021. URL `https://www.rilem.net/boutique/fiche.php?cat=journal&reference=1521`.

Akbar Ghanbari and Bhushan L. Karihaloo. Prediction of the plastic viscosity of self-compacting steel fibre reinforced concrete. *Cement and Concrete Research*, 39(12):1209–1216, December 2009. ISSN 00088846. doi: 10.1016/j.cemconres.2009.08.018. URL `http://linkinghub.elsevier.com/retrieve/pii/S0008884609002312`.

Boyce E. Griffith and Charles S. Peskin. On the order of accuracy of the immersed boundary method: Higher order convergence rates for sufficiently smooth problems. *Journal of Computational Physics*, 208(1):75–105, September 2005. ISSN 00219991. doi: 10.1016/j.jcp.2005.02.011. URL `http://linkinghub.elsevier.com/retrieve/pii/S0021999105000835`.

S. Grunewald. *Performance-based design of self-compacting fibre reinforced concrete*. PhD thesis, 2004. URL `http://repository.tudelft.nl/view/ir/uuid:07a817aa-cba1-4c93-bbed-40a5645cf0f1/`.

A. K Gunstensen and D. H Rothman. Microscopic Modeling of Immiscible Fluids in Three Dimensions by a Lattice Boltzmann Method. *Europhysics Letters (EPL)*, 18(2):157–161, February 1992. ISSN 0295-5075. doi: 10.1209/0295-5075/18/2/012. URL `http://stacks.iop.org/0295-5075/18/i=2/a=012?key=crossref.b2bfa72b3614397ed53b35c8b589a264`.

Zhaoli Guo, Chuguang Zheng, and Baochang Shi. Discrete lattice effects on the forcing term in the lattice Boltzmann method. *Physical Review E*, 65 (4):1–6, April 2002. ISSN 1063-651X. doi: 10.1103/PhysRevE.65.046308. URL `http://link.aps.org/doi/10.1103/PhysRevE.65.046308`.

Zhaoli Guo, T. S. Zhao, and Yong Shi. Physical symmetry, spatial accuracy, and relaxation time of the lattice Boltzmann equation for microgas

flows. *Journal of Applied Physics*, 99(7):074903, 2006. ISSN 00218979. doi: 10.1063/1.2185839. URL `http://link.aip.org/link/JAPIAU/v99/i7/p074903/s1&Agg=doi`.

Xiaoyi He, Qisu Zou, Li-Shi Luo, and Micah Dembo. Analytic solutions of simple flows and analysis of nonslip boundary conditions for the lattice Boltzmann BGK model. *Journal of Statistical Physics*, 87(1-2):115–136, April 1997. ISSN 0022-4715. doi: 10.1007/BF02181482. URL `http://www.springerlink.com/index/10.1007/BF02181482`.

Emil Midtgaard Hvilsom and Gitte Dreyer Rasmussen. *Fibre Orientation and Distribution in Steel Fibre Reinforced SCC*. Master thesis, Technical University of Denmark, 2011.

Takaji Inamuro. A lattice kinetic scheme for incompressible viscous flows with heat transfer. *Philosophical transactions. Series A, Mathematical, physical, and engineering sciences*, 360(1792):477–84, March 2002. ISSN 1364-503X. doi: 10.1098/rsta.2001.0942. URL `http://www.ncbi.nlm.nih.gov/pubmed/16210191`.

Takaji Inamuro, Masato Yoshino, and Fumimaru Ogino. A non-slip boundary condition for lattice Boltzmann simulations. *arXiv preprint comp-gas/9508002*, 1995. URL `http://arxiv.org/abs/comp-gas/9508002`.

Stefan Jacobsen, Lars Haugan, Tor Arne Hammer, and Evangelos Kalogiannidis. Flow conditions of fresh mortar and concrete in different pipes. *Cement and Concrete Research*, 39(11):997–1006, November 2009. ISSN 00088846. doi: 10.1016/j.cemconres.2009.07.005. URL `http://linkinghub.elsevier.com/retrieve/pii/S0008884609001653`.

Stefan Jacobsen, Hedda Vikan, and Lars Haugan. *Flow of SCC along Surfaces*. Springer Netherlands, Dordrecht, 2010. ISBN 978-90-481-9663-0. doi: 10.1007/978-90-481-9664-7. URL `http://www.springerlink.com/index/10.1007/978-90-481-9664-7`.

Anette Jansson, Ingemar Löfgren, and K Gylltoft. Design methods of fibre reinforced concrete: a state-of-the-art review. *Nordic Concrete Research*, pages 21–36, 2008. URL `http://swepub.kb.se/bib/swepub:oai:services.scigloo.org:68892?tab2=subj`.

GB Jeffery. The motion of ellipsoidal particles immersed in a viscous fluid. *Proceedings of the Royal Society of London. Series A*, 102(715):161–179, 1922. URL `http://www.jstor.org/stable/10.2307/94111`.

Lin Jianzhong, Shi Xing, and You Zhenjiang. Effects of the aspect ratio on the sedimentation of a fiber in Newtonian fluids. *Journal of Aerosol Science*, 34(7):909–921, July 2003. ISSN 00218502. doi: 10.1016/S0021-8502(03)00039-9. URL http://linkinghub.elsevier.com/retrieve/pii/S0021850203000399.

S.-T. Kang and J.-K. Kim. Numerical simulation of the variation of fiber orientation distribution during flow molding of Ultra High Performance Cementitious Composites (UHPCC). *Cem. Concr. Compos.*, 34:208–217, 2012.

Terje Kanstad, Juvik Dan Arve, Arne Vatnar, Alf Egil Mathisen, Sindre Sandbakk, Hedda Vikan, Eirik Nikolaisen, Ase Dossland, Nils Leirud, and Ove Geir Overrein. *Forslag til retningslinjer for dimensjonering, utførelse og kontroll av fiberarmerte betongkonstruksjoner*. Oslo SINTEF Building and Infrastructure, 2011. ISBN 9788253612232. URL http://www.coinweb.no/files/Reports/Forslagtilretningslinjer-fiberarmertebetongkonstruksjoner.pdf.

AG Kooiman. Modelling steel fibre reinforced concrete for structural design. 2000. URL http://www.narcis.nl/publication/RecordID/oai:tudelft.nl:uuid:e7a12191-4484-4fc3-b4c5-e8c0d51271a0.

C. Körner, M. Thies, T. Hofmann, N. Thürey, and U. Rüde. Lattice Boltzmann Model for Free Surface Flow for Modeling Foaming. *Journal of Statistical Physics*, 121(1-2):179–196, October 2005. ISSN 0022-4715. doi: 10.1007/s10955-005-8879-8. URL http://www.springerlink.com/index/10.1007/s10955-005-8879-8.

H. Krenchel. Fibre spacing and specific fibre surface. *A. Neville (Ed.), Fibre Reinforced Cement and Concrete, The Construction, Press, UK*, pages 69–79, 1975.

Irvin M. Krieger. A Mechanism for Non-Newtonian Flow in Suspensions of Rigid Spheres. *Journal of Rheology*, 3(1):137, 1959. ISSN 01486055. doi: 10.1122/1.548848. URL http://link.aip.org/link/?JOR/3/137/1&Agg=doihttp://ci.nii.ac.jp/naid/10018721107/.

Janneke Kromkamp, Dirk van den Ende, Drona Kandhai, Ruud van der Sman, and Remko Boom. Lattice Boltzmann simulation of 2D and 3D non-Brownian suspensions in Couette flow. *Chemical Engineering Science*, 61(2):858–873, January 2006. ISSN 00092509. doi: 10.1016/j.ces.

2005.08.011. URL `http://linkinghub.elsevier.com/retrieve/pii/S0009250905006639`.

S Kulasegaram, Bhushan L. Karihaloo, and Akbar Ghanbari. Modelling the flow of self-compacting concrete. *Numerical and Analytical Methods in Geomechanics*, (April 2010):713–723, 2011. doi: 10.1002/nag. URL `http://onlinelibrary.wiley.com/doi/10.1002/nag.924/full`.

Sivakumar Kulasegaram and BL Karihaloo. Fibre-reinforced, self-compacting concrete flow modelled by smooth particle hydrodynamics. In *Proceedings of the ICE - Engineering and Computational Mechanics*, volume 166, 2013. URL `http://www.icevirtuallibrary.com/content/article/10.1680/eacm.11.00004`.

AJC Ladd and R. Verberg. Lattice-Boltzmann simulations of particle-fluid suspensions. *Journal of Statistical Physics*, 104(5):1191–1251, 2001. doi: 10.1023/A:1010414013942. URL `http://www.springerlink.com/index/W2V150146N3357K7.pdf`.

Anthony J. C. Ladd. Numerical simulations of particulate suspensions via a discretized Boltzmann equation. Part 1. Theoretical foundation. *Journal of Fluid Mechanics*, 271:285, April 2006a. ISSN 0022-1120. doi: 10.1017/S0022112094001771. URL `http://www.journals.cambridge.org/abstract_S0022112094001771`.

Anthony J. C. Ladd. Numerical simulations of particulate suspensions via a discretized Boltzmann equation. Part 2. Numerical results. *Journal of Fluid Mechanics*, 271(1):311, April 2006b. ISSN 0022-1120. doi: 10.1017/S0022112094001783. URL `http://www.journals.cambridge.org/abstract_S0022112094001783`.

Pierre Lallemand and Li-Shi Luo. Lattice Boltzmann method for moving boundaries. *Journal of Computational Physics*, 184(2):406–421, January 2003. ISSN 00219991. doi: 10.1016/S0021-9991(02)00022-0. URL `http://www.sciencedirect.com/science/article/pii/S0021999102000220http://linkinghub.elsevier.com/retrieve/pii/S0021999102000220`.

F. Laranjeira, C. Molins, and a. Aguado. Predicting the pullout response of inclined hooked steel fibers. *Cement and Concrete Research*, 40(10):1471–1487, October 2010. ISSN 00088846. doi: 10.1016/j.cemconres.2010.05.005. URL `http://linkinghub.elsevier.com/retrieve/pii/S0008884610001249`.

F. Laranjeira, a. Aguado, C. Molins, S. Grünewald, J. Walraven, and S. Cavalaro. Framework to predict the orientation of fibers in FRC: A novel philosophy. *Cement and Concrete Research*, 42(6):752–768, June 2012. ISSN 00088846. doi: 10.1016/j.cemconres.2012.02.013. URL `http://linkinghub.elsevier.com/retrieve/pii/S0008884612000415`.

J.F. Lataste, M. Behloul, and D. Breysse. Characterisation of fibres distribution in a steel fibre reinforced concrete with electrical resistivity measurements. *NDT & E International*, 41(8):638–647, December 2008. ISSN 09638695. doi: 10.1016/j.ndteint.2008.03.008. URL `http://linkinghub.elsevier.com/retrieve/pii/S0963869508000315`.

Jonas Latt. *Hydrodynamic limit of lattice Boltzmann equations*. PhD thesis, Universite de Geneve, 2007. URL `http://archive-ouverte.unige.ch/vital/access/services/Download/unige:464/THESIS`.

Jonas Latt and Bastien Chopard. Straight velocity boundaries in the lattice Boltzmann method. *Physical Review E*, 77(5):1–16, May 2008. ISSN 1539-3755. doi: 10.1103/PhysRevE.77.056703. URL `http://link.aps.org/doi/10.1103/PhysRevE.77.056703`.

P Laure and L Silva. Numerical modelling of concrete flow with rigid fibers. *10th Esaform Conference on Material Forming*, pages 1390–1396, 2007. URL `http://journalofrheology.org/resource/1/jorhd2/v31/i8/p751_s1http://pdfserv.aip.org/APCPCS/vol_907/iss_1/1390_1.pdf`.

Paul Lavallée, Jean Pierre Boon, and Alain Noullez. Boundaries in lattice gas flows. *Physica D: Nonlinear Phenomena*, 47(1-2):233–240, January 1991. ISSN 01672789. doi: 10.1016/0167-2789(91)90294-J. URL `http://linkinghub.elsevier.com/retrieve/pii/016727899190294J`.

T.-H. Le, P.J.J. Dumont, L. Orgéas, D. Favier, L. Salvo, and E. Boller. X-ray phase contrast microtomography for the analysis of the fibrous microstructure of SMC composites. *Composites Part A: Applied Science and Manufacturing*, 39(1):91–103, January 2008. ISSN 1359835X. doi: 10.1016/j.compositesa.2007.08.027. URL `http://linkinghub.elsevier.com/retrieve/pii/S1359835X07001741`.

Y Lee, S.-T. Kang, and J.-K. Kim. Pullout behavior of inclined steel fiber in an ultra-high strength cementitious matrix. *Const. Build. Mat.*, 24: 2030–2041, 2010.

Yong Lee, Seok Lee, Jae Youn, Kwansoo Chung, and Tae Kang. Characterization of fiber orientation in short fiber reinforced composites with an image processing technique. *Materials Research Innovations*, 6(2):65–72, September 2002. ISSN 1432-8917. doi: 10.1007/s10019-002-0180-8. URL `http://www.springerlink.com/openurl.asp?genre=article&id=doi:10.1007/s10019-002-0180-8`.

C.R. Leonardi, D.R.J. Owen, and Y.T. Feng. Numerical rheometry of bulk materials using a power law fluid and the lattice Boltzmann method. *Journal of Non-Newtonian Fluid Mechanics*, 166(12-13):628–638, 2011. ISSN 03770257. doi: 10.1016/j.jnnfm.2011.02.011. URL `http://linkinghub.elsevier.com/retrieve/pii/S0377025711000772`.

V C Li, Y Wang, and S Backer. Effect of inclining angle, bundling, and surface treatment on synthetic fiber pull-out from a cement matrix. *Composites*, 21(2):132–140, 1990.

Z Li, M A Perez Lara, and J E Bolander. Restraining effects of fibers during non-uniform drying of cement composites. *Cem. Concr. Res.*, 36(9):1643–1652, 2006.

Jie Liao and Xiao-Ping Wang. Stability of an efficient Navier-Stokes solver with Navier boundary condition. *Discrete and Continuous Dynamical Systems - Series B*, 17(1):153–171, October 2011. ISSN 1531-3492. doi: 10.3934/dcdsb.2012.17.153. URL `http://www.aimsciences.org/journals/displayArticlesnew.jsp?paperID=6596`.

C. Y. Lim, C. Shu, X. D. Niu, and Y. T. Chew. Application of lattice Boltzmann method to simulate microchannel flows. *Physics of Fluids*, 14(7):2299, 2002. ISSN 10706631. doi: 10.1063/1.1483841. URL `http://link.aip.org/link/PHFLE6/v14/i7/p2299/s1&Agg=doi`.

Jianzhong Liu, Changfeng Li, Zhaojin Du, and Gong Cui. Characterization of fiber distribution in steel fiber reinforced cementitious composites with low water-binder ratio. *Indian Journal of Engineering and Materials Sciences*, 18(December):449–457, 2011. URL `http://nopr.niscair.res.in/handle/123456789/13602`.

Jianzhong Liu, Wei Sun, Changwen Miao, Jiaping Liu, and Changfeng Li. Assessment of fiber distribution in steel fiber mortar using image analysis. *Journal of Wuhan University of Technology-Mater. Sci. Ed.*, 27(1):166–171, February 2012. ISSN 1000-2413. doi: 10.1007/

s11595-012-0429-z.   URL `http://www.springerlink.com/index/10.1007/s11595-012-0429-z`.

I Markovic. *High-performance hybrid-fibre concrete: development and utilization.* PhD thesis, Technical University of Delft, The Netherlands, 2006.

L. Martinie and N. Roussel. Simple tools for fiber orientation prediction in industrial practice. *Cement and Concrete Research*, 41(10): 993–1000, October 2011. ISSN 00088846. doi: 10.1016/j.cemconres. 2011.05.008. URL `http://linkinghub.elsevier.com/retrieve/pii/S0008884611001608`.

Nicos Martys and Jack Douglas. Critical properties and phase separation in lattice Boltzmann fluid mixtures. *Physical Review E*, 63(3):1–18, February 2001. ISSN 1063-651X. doi: 10.1103/PhysRevE.63.031205. URL `http://link.aps.org/doi/10.1103/PhysRevE.63.031205`.

Renwei Mei, Li-Shi Luo, and Wei Shyy. An Accurate Curved Boundary Treatment in the Lattice Boltzmann Method. *Journal of Computational Physics*, 155(2):307–330, November 1999. ISSN 00219991. doi: 10.1006/jcph.1999.6334. URL `http://www.sciencedirect.com/science/article/pii/S0021999199963349http://linkinghub.elsevier.com/retrieve/pii/S0021999199963349`.

Renwei Mei, Dazhi Yu, Wei Shyy, and Li-Shi Luo. Force evaluation in the lattice Boltzmann method involving curved geometry. *Physical Review E*, 65 (4):1–14, April 2002. ISSN 1063-651X. doi: 10.1103/PhysRevE.65.041203. URL `http://link.aps.org/doi/10.1103/PhysRevE.65.041203`.

B Mobasher, H Stang, and SP Shah. Microcracking in fiber reinforced concrete. *Cement and Concrete Research*, 20(c):665–676, 1990. URL `http://www.sciencedirect.com/science/article/pii/000888469090001E`.

A.A. Mohamad and A. Kuzmin. A critical evaluation of force term in lattice Boltzmann method, natural convection problem. *International Journal of Heat and Mass Transfer*, 53(5-6):990–996, February 2010. ISSN 00179310. doi: 10.1016/j.ijheatmasstransfer.2009.11.014. URL `http://linkinghub.elsevier.com/retrieve/pii/S0017931009006036`.

S. Montgomery-Smith, David a. Jack, and Douglas E. Smith. A systematic approach to obtaining numerical solutions of Jeffery's type equations using Spherical Harmonics. *Composites Part A: Applied Science and Manufacturing*, 41(7):827–835, July 2010. ISSN 1359835X. doi:

10.1016/j.compositesa.2010.02.010. URL `http://linkinghub.elsevier.com/retrieve/pii/S1359835X10000679`.

C Navier. Memoire sur les lois du mouvement des fluides. *Memoires de l 'Academie Royale des Sciences de l'nstitut de France*, 6:389–440, 1823.

Adam M Neville. *Properties of concrete.* 1995. ISBN 0-582-23070-5.

N.-Q. Nguyen and A. Ladd. Lubrication corrections for lattice-Boltzmann simulations of particle suspensions. *Physical Review E*, 66(4):1–12, October 2002. ISSN 1063-651X. doi: 10.1103/PhysRevE.66.046708. URL `http://link.aps.org/doi/10.1103/PhysRevE.66.046708`.

Mitsuhiro Ohta, Tatsuya Nakamura, Yutaka Yoshida, and Yosuke Matsukuma. Lattice Boltzmann simulations of viscoplastic fluid flows through complex flow channels. *Journal of Non-Newtonian Fluid Mechanics*, 166(7-8):404–412, April 2011. ISSN 03770257. doi: 10.1016/j.jnnfm.2011.01.011. URL `http://linkinghub.elsevier.com/retrieve/pii/S0377025711000280`.

A Okabe, B Boots, K Sugihara, and S N Chiu. *Spatial Tessellations: Concepts and Applications of Voronoi Diagrams (Wiley Series in Probability and Mathematical Statistics).* John Wiley & Sons Ltd., England, second edition, 2000.

Hajime Okamura and Masahiro Ouchi. Self-Compacting Concrete. *Journal of Advanced Concrete Technology*, 1(1):5–15, 2003. ISSN 1346-8014. doi: 10.3151/jact.1.5. URL `http://joi.jlc.jst.go.jp/JST.JSTAGE/jact/1.5?from=CrossRef`.

Filipe Laranjeira De Oliveira. *Design-oriented constitutive model for steel fiber reinforced concrete.* PhD thesis, 2010. URL `http://www.tdx.cat/handle/10803/6174`.

C Ouyang, A Pacios, and S P Shah. Pullout of inclined fibers from cementitious matrix. *J. Eng. Mech.*, 120(12):2641–2659, 1994.

Nilufer Ozyurt, Thomas O. Mason, and Surendra P. Shah. Non-destructive monitoring of fiber orientation using AC-IS: An industrial-scale application. *Cement and Concrete Research*, 36(9):1653–1660, September 2006. ISSN 00088846. doi: 10.1016/j.cemconres.2006.05.026. URL `http://linkinghub.elsevier.com/retrieve/pii/S0008884606001530`.

N Phan-Thien and B L Karihaloo. Materials with negative Poisson's ratio: a qualitative microstructural model. *Journal of applied mechanics*, 61(4): 1001–1004, 1994.

Jay H. Phelps and Charles L. Tucker. An anisotropic rotary diffusion model for fiber orientation in short- and long-fiber thermoplastics. *Journal of Non-Newtonian Fluid Mechanics*, 156(3):165–176, February 2009. ISSN 03770257. doi: 10.1016/j.jnnfm.2008.08.002. URL `http://linkinghub.elsevier.com/retrieve/pii/S0377025708001602`.

Dewei Qi. Direct simulations of flexible cylindrical fiber suspensions in finite Reynolds number flows. *The Journal of chemical physics*, 125(11):114901, September 2006. ISSN 0021-9606. doi: 10.1063/1.2336777. URL `http://www.ncbi.nlm.nih.gov/pubmed/16999505`.

P. Rossi, P. Acker, and Y. Malier. Effect of steel fibres at two different stages: The material and the structure. *Materials and Structures*, 20(6): 436–439, November 1987. ISSN 0025-5432. doi: 10.1007/BF02472494. URL `http://www.springerlink.com/index/10.1007/BF02472494`.

N. Roussel and P. Coussot. "Fifty-cent rheometer" for yield stress measurements: From slump to spreading flow. *Journal of Rheology*, 49 (3):705, 2005. ISSN 01486055. doi: 10.1122/1.1879041. URL `http://link.aip.org/link/JORHD2/v49/i3/p705/s1&Agg=doi`.

Nicolas Roussel, Mette R Geiker, Frédéric Dufour, Lars N Thrane, and Peter Szabo. Computational modeling of concrete flow: General overview. *Cement and Concrete Research*, 37(9):1298–1307, September 2007. ISSN 00088846. doi: 10.1016/j.cemconres.2007.06.007. URL `http://linkinghub.elsevier.com/retrieve/pii/S0008884607001366`.

Asif Salahuddin, Jingshu Wu, and C. K. Aidun. Numerical study of rotational diffusion in sheared semidilute fibre suspension. *Journal of Fluid Mechanics*, 692:153–182, December 2011. ISSN 0022-1120. doi: 10.1017/jfm.2011.501. URL `http://www.journals.cambridge.org/abstract_S0022112011005015`.

S Sandbakk. *Fibre Reinforced Concrete: Evaluation of test methods and material development.* PhD thesis, 2011. URL `http://ntnu.diva-portal.org/smash/record.jsf?pid=diva2:477607`.

Elena Vidal Sarmiento. *Influence of concrete flow on the mechanical properties of ordinary and fibre reinforced concrete.* Master thesis, Technical University of Catalonia, 2011.

C. Shu, N. Liu, and Y.T. Chew. A novel immersed boundary velocity correction–lattice Boltzmann method and its application to simulate flow past a circular cylinder. *Journal of Computational Physics*, 226(2):1607–1622, October 2007. ISSN 00219991. doi: 10.1016/j.jcp.2007.06.002. URL `http://linkinghub.elsevier.com/retrieve/pii/S0021999107002513`.

T. Soetens, a. Van Gysel, S. Matthys, and L. Taerwe. A semi-analytical model to predict the pull-out behaviour of inclined hooked-end steel fibres. *Construction and Building Materials*, 43:253–265, June 2013. ISSN 09500618. doi: 10.1016/j.conbuildmat.2013.01.034. URL `http://linkinghub.elsevier.com/retrieve/pii/S0950061813001050`.

Parviz Soroushian and Cha-Don Lee. Distribution and Orientation of Fibers in Steel Fiber Reinforced Concrete. *Materials Journal*, 87(5):433–439, 1990.

J Spangenberg, MR Geiker, JH Hattel, and H Stang. *Numerisk modellering af formfyldning ved støbning i selvkompakterende beton*. PhD thesis, 2012a. URL `http://forskningsbasen.deff.dk/Share.external?sp=S0eeede98-fb07-4800-86e2-0a6baeb1e7a3&sp=Sdtu`.

J. Spangenberg, N. Roussel, J.H. Hattel, H. Stang, J. Skocek, and M.R. Geiker. Flow induced particle migration in fresh concrete: Theoretical frame, numerical simulations and experimental results on model fluids. *Cement and Concrete Research*, 42(4):633–641, April 2012b. ISSN 00088846. doi: 10.1016/j.cemconres.2012.01.007. URL `http://linkinghub.elsevier.com/retrieve/pii/S0008884612000166`.

Patrick Stähli, Rocco Custer, and Jan G. M. Mier. On flow properties, fibre distribution, fibre orientation and flexural behaviour of FRC. *Materials and Structures*, 41(1):189–196, February 2007. ISSN 1359-5997. doi: 10.1617/s11527-007-9229-x. URL `http://www.springerlink.com/index/10.1617/s11527-007-9229-x`.

P Stroeven. Morphometry of fibre reinforced cementitious materials. *Matériaux et Construction*, 1979. URL `http://link.springer.com/article/10.1007/BF02473994`.

P Stroeven. Steel fibre reinforcement at boundaries in concrete elements. In *Third International RILEM Workshop on High Performance Fiber Reinforced Cement*, pages 412–422, 1999.

Sauro Succi. Mesoscopic Modeling of Slip Motion at Fluid-Solid Interfaces with Heterogeneous Catalysis. *Physical Review Letters*, 89(6):064502, July

2002. ISSN 0031-9007. doi: 10.1103/PhysRevLett.89.064502. URL `http://link.aps.org/doi/10.1103/PhysRevLett.89.064502`.

Michael C. Sukop and Daniel T. Thorne. *Lattice Boltzmann Modeling: An Introduction for Geoscientists and Engineers*. Springer, 2005. ISBN 3540279814. URL `http://www.amazon.com/Lattice-Boltzmann-Modeling-Introduction-Geoscientists/dp/3540279814`.

Jussi-Petteri Suuronen, Aki Kallonen, Marika Eik, Jari Puttonen, Ritva Serimaa, and Heiko Herrmann. Analysis of short fibres orientation in steel fibre-reinforced concrete (SFRC) by X-ray tomography. *Journal of Materials Science*, 48(3):1358–1367, October 2012. ISSN 0022-2461. doi: 10.1007/s10853-012-6882-4. URL `http://www.springerlink.com/index/10.1007/s10853-012-6882-4`.

E Thorenfeldt. Theoretical tensile strength after cracking. Fibre orientation and average stress in fibres. In *Proceedings of the Nordic Concrete Federeation Workshop on Design Rules for Steel Fibre Reinforced Concrete Structures*, pages 43–60, 2003. URL `http://scholar.google.com/scholar?hl=en&btnG=Search&q=intitle:Theoretical+tensile+strength+after+cracking.+Fibre+orientation+and+average+stress+in+fibres#5`.

Lars Nyholm Thrane. *Form Filling with Self-Compacting Concrete*. PhD thesis, Technical University of Denmark, 2007. URL `http://www.byg.dtu.dk/upload/institutter/byg/publications/rapporter/byg-r172.pdf`.

Lars Nyholm Thrane, Claus Pade, Claus V. Nielsen, Ara A. Jeknavorian, John J. Schemmel, and S. W. Dean. Determination of Rheology of Self-Consolidating Concrete Using the 4C-Rheometer and How to Make Use of the Results. *Journal of ASTM International*, 7(1):102003, 2010. ISSN 1546962X. doi: 10.1520/JAI102003. URL `http://www.astm.org/doiLink.cgi?JAI102003`.

Markus Uhlmann. An immersed boundary method with direct forcing for the simulation of particulate flows. *Journal of Computational Physics*, 209(2):448–476, November 2005. ISSN 00219991. doi: 10.1016/j.jcp.2005.03.017. URL `http://linkinghub.elsevier.com/retrieve/pii/S0021999105001385`.

L Vandewalle. RILEM TC 162-TDF: Test and design methods for steel fibre reinforced concrete. *Materials and Structures*, 33(February):3–5, 2000. URL `https://lirias.kuleuven.be/handle/123456789/36241`.

K. Vasilic, B. Meng, H.C. Kühne, and N. Roussel. Flow of fresh concrete through steel bars: A porous medium analogy. *Cement and Concrete Research*, 41(5):496–503, May 2011. ISSN 00088846. doi: 10.1016/j.cemconres.2011.01.013. URL `http://linkinghub.elsevier.com/retrieve/pii/S0008884611000147`.

A. Vikhansky. Lattice-Boltzmann method for yield-stress liquids. *Journal of Non-Newtonian Fluid Mechanics*, 155(3):95–100, December 2008. ISSN 03770257. doi: 10.1016/j.jnnfm.2007.09.001. URL `http://linkinghub.elsevier.com/retrieve/pii/S0377025707001978`.

Oldřich Švec and Jan Skoček. Numerical simulation of the free surface flow of rigid fibres immersed in the non-Newtonian fluid. *Journal of Non-Newtonian Fluid Mechanics*, (To be published), 2013a.

Oldřich Švec and Jan Skoček. Simple Navier's slip boundary condition for the non-Newtonian Lattice Boltzmann fluid dynamics solver. *Journal of Non-Newtonian Fluid Mechanics*, 199:61–69, 2013b.

Oldřich Švec, Jan Skoček, Henrik Stang, John Forbes Olesen, and Peter Noe Poulsen. Flow simulation of fiber reinforced self compacting concrete using Lattice Boltzmann method. In A. Palomo, A. Zaragoza, and J.C. Lopez Agui, editors, *Abstracts and Proceedings in International Congress on the Chemistry of Cement, Madrid*, pages 1–7, 2011.

Oldřich Švec, Jan Skoček, John Forbes Olesen, and Henrik Stang. Fibre reinforced self-compacting concrete flow simulations in comparison with L-Box experiments using Carbopol. In Joaquim Barros, José Sena-Cruz, Rui Ferreira, Isabel Valente, Miguel Azenha, and Salvador Dias, editors, *Proceedings of 8th Rilem International Symposium on Fibre reinforced concrete : Challenges and Opportunities*, pages 1–8, Guimaraes, 2012a. RILEM Publications.

Oldřich Švec, Jan Skoček, Henrik Stang, Mette R. Geiker, and Nicolas Roussel. Free surface flow of a suspension of rigid particles in a non-Newtonian fluid: a Lattice Boltzmann approach. *Journal of Non-Newtonian Fluid Mechanics*, 179-180:32–42, June 2012b. ISSN 03770257. doi: 10.1016/j.jnnfm.2012.05.005. URL `http://linkinghub.elsevier.com/retrieve/pii/S0377025712001061`.

Oldřich Švec, Henrik Stang, John Forbes Olesen, and Lars Nyholm Thrane. Application of the fluid dynamics model to the field of fibre reinforced self-compacting concrete. In *Proceedings of the International Conference on Numerical Modeling Strategies for Sustainable Concrete Structures (SSCS), P. Rossi and J.-L. Tailhan, eds., Aix-en-Provence, France (on CD-ROM)*, pages 1–9, 2012c.

Giedrius Žirgulis, Mette Rica Geiker, Oldřich Švec, and Terje Kanstad. Potential methods for quality control of fibre distribution in FRC SCC. In *Proceedings of 7th international conference on self compacting concrete*, pages 1–8, 2013a.

Giedrius Žirgulis, Oldřich Švec, Terje Kanstad, Mette Rica Geiker, and Andrzej Cwirzen. Experimental and numerical methods for characterization of steel fibre distribution in SCC slabs. *To be published*, 2013b.

S. Wansom and S. Janjaturaphan. Evaluation of fiber orientation in plant fiber-cement composites using AC-impedance spectroscopy. *Cement and Concrete Research*, 45:37–44, March 2013. ISSN 00088846. doi: 10.1016/j.cemconres.2012.11.003. URL http://linkinghub.elsevier.com/retrieve/pii/S000888461200258X.

Dieter A. Wolf-Gladrow. *Lattice-Gas Cellular Automata and Lattice Boltzmann Models: An Introduction (Lecture Notes in Mathematics)*. Springer, 2000. ISBN 3540669736. URL http://www.springerlink.com.globalproxy.cvt.dk/content/978-3-540-66973-9/.

LY Woo, S Wansom, and AD Hixson. A universal equivalent circuit model for the impedance response of composites. *Journal of Materials Science*, 8:2265–2270, 2003. URL http://www.springerlink.com/index/J4T110631J55401N.pdf.

J. Wu and C. Shu. Implicit velocity correction-based immersed boundary-lattice Boltzmann method and its applications. *Journal of Computational Physics*, 228(6):1963–1979, April 2009. ISSN 00219991. doi: 10.1016/j.jcp.2008.11.019. URL http://linkinghub.elsevier.com/retrieve/pii/S0021999108006116.

J. Wu and C. Shu. An improved immersed boundary-lattice Boltzmann method for simulating three-dimensional incompressible flows. *Journal of Computational Physics*, 229(13):5022–5042, 2010. ISSN 00219991. doi: 10.1016/j.jcp.2010.03.024. URL http://linkinghub.elsevier.com/retrieve/pii/S0021999110001348.

Jingshu Wu and CK Aidun. Simulating 3D deformable particle suspensions using lattice Boltzmann method with discrete external boundary force. *International journal for numerical methods in fluids*, (March 2009):765–783, 2009. doi: 10.1002/fld. URL `http://onlinelibrary.wiley.com/doi/10.1002/fld.2043/abstract`.

Jingshu Wu and Cyrus K. Aidun. A method for direct simulation of flexible fiber suspensions using lattice Boltzmann equation with external boundary force. *International Journal of Multiphase Flow*, 36(3): 202–209, March 2010. ISSN 03019322. doi: 10.1016/j.ijmultiphaseflow. 2009.11.003. URL `http://linkinghub.elsevier.com/retrieve/pii/S0301932209001724`.

J Wuest and E Denarié. Tomography Analysis Of Fiber Distribution And Orientation In Ultra High-Performance Fiber-Reinforced Composites With High-Fiber Dosages. *Experimental Techniques*, (October):50–55, 2009. doi: 10.1111/j.1747-1567.2009.00420.x. URL `http://onlinelibrary.wiley.com/doi/10.1111/j.1747-1567.2008.00420.x/full`.

Yuichi Yamane, Yukio Kaneda, and Masao Dio. Numerical simulation of semi-dilute suspensions of rodlike particles in shear flow. *Journal of Non-Newtonian Fluid Mechanics*, 54:405–421, August 1994. ISSN 03770257. doi: 10.1016/0377-0257(94)80033-2. URL `http://linkinghub.elsevier.com/retrieve/pii/0377025794800332`.

Xiaolei Yang, Xing Zhang, Zhilin Li, and Guo-Wei He. A smoothing technique for discrete delta functions with application to immersed boundary method in moving boundary simulations. *Journal of Computational Physics*, 228(20):7821–7836, November 2009. ISSN 00219991. doi: 10.1016/j.jcp.2009.07.023. URL `http://linkinghub.elsevier.com/retrieve/pii/S0021999109004136`.

R. Zerbino, J.M. Tobes, M.E. Bossio, and G. Giaccio. On the orientation of fibres in structural members fabricated with self compacting fibre reinforced concrete. *Cement and Concrete Composites*, 34(2):191–200, February 2012. ISSN 09589465. doi: 10.1016/j.cemconcomp.2011.09.005. URL `http://linkinghub.elsevier.com/retrieve/pii/S0958946511001624`.

List of Figures

Numerical framework capable of predicting fibre orientation and distribution in structural elements made of fibre reinforced self-compacting concrete was developed. The developed framework is capable of simulating free-surface flow of a suspension of explicitly represented rigid particles immersed in the non-Newtonian fluid. The ability to simulate the casting process of the concrete, including the movement of individual immersed fibres in response to such factors as casting method, formwork geometry and surface roughness, has profound implications toward the effective use of these materials.